Dissertation

submitted to the
Combined Faculties for the Natural Sciences and for Mathematics
of the Ruperto-Carola University of Heidelberg, Germany
for the degree of
Doctor of Natural Sciences

presented by
Diplom-Physiker Andreas Krauß
born in Tübingen, Germany

Oral examination: February 1, 2012

Compensation of intra-fractional organ motion through multileaf collimator tracking

Referees: Prof. Dr. Uwe Oelfke
Prof. Dr. Wolfgang Schlegel

Zusammenfassung

In der vorliegenden Arbeit zeigen wir umfangreiche Verbesserungen und Erweiterungen eines im Hause entwickelten Lamellenkollimator (MLC) Kontrollsystems. Das MLC Kontrollsystem gleich Organbewegungen während der Bestrahlung aus, indem es die Apertur eines dynamischen MLC in Echtzeit an kontinuierlich detektierte Organbewegungen anpasst. Unsere wichtigsten Verbesserungen sind: Erstens, die Integration klinisch anwendbarer Technologien zur Detektion von Organbewegungen basierend auf implantierten elektromagnetischen Transpondern, einem neuartigen Röntgen-Bildgebungssystem oder einer Kombination aus einem System zur Detektion von Oberflächen-Bewegungen und dem Röntgen-Bildgebungssystem. Zweitens, die Verwendung modernster Methoden zur Vorhersage von Atembewegungen um die Latenzzeiten des Systems zwischen 0.5 s und 0.6 s auszugleichen. Drittens, die komplette Neuentwicklung der MLC Kontrollsoftware mit dem Ziel einer in hohem Maße zuverlässigen und stabilen Anwendung sowie einer wartungsfreundlichen und erweiterbaren Software. Wir charakterisieren die Leistungsfähigkeit des MLC Kontrollsystems durch Phantomexperimente unter Verwendung sinusförmiger Bewegungsmuster sowie unregelmäßiger Atmungs- und Prostatabewegungsmuster. Wir können die verbleibenden geometrischen Unsicherheiten des Bewegungsausgleichs auf den Fehler der Bewegungsvorhersage reduzieren. Mittels Filmdosimetrie weisen wir nach, dass das MLC Kontrollsystem die negativen Auswirkungen von Organbewegungen auf die Dosisverteilung weitgehend eliminieren kann.

Abstract

In this thesis, we present substantial improvements and extensions of a previously inhouse developed multileaf collimator (MLC) tracking system. The MLC tracking system compensates for intra-fractional organ motion by adapting the aperture of a dynamic MLC in real-time to continuously monitored target motion. Our main improvements are: Firstly, the integration of clinically applicable intra-fractional motion monitoring devices based on implanted electromagnetic transponders, a novel x-ray imaging system or a combined external surrogate monitoring and x-ray imaging system. Secondly, the implementation of state-of-the-art respiratory motion forward prediction models to compensate for total system latencies of 0.5 s to 0.6 s. Thirdly, a complete redesigned of the MLC control software towards a high level of application reliability and stability as well as software maintainability and further extendability. We assess the tracking performance in various phantom experiments with sinusoidal, irregular breathing and prostate trajectories. We can reduce the remaining geometric MLC tracking uncertainties to the respiratory motion forward prediction error. Our film dosimetry evaluations demonstrate that the integrated MLC tracking system can largely eliminate the negative effects of intra-fractional organ motion on the dose distribution.

Contents

1 Introduction

The goal of radiotherapy is to deliver a lethal amount of radiation dose to cancerous target volumes while sparing the surrounding tissues from dose. The invention of intensity-modulated radiotherapy (IMRT) has increased the ability to deliver conformal dose distributions to complex-shaped static target volumes using high energy x-rays. This dose conformity can however be compromised by organ motion (Bortfeld et al., 2004). In particular, the dose-blurring effects observed when target motion is present undermine the delivery of optimized dose distributions exhibiting steep dose gradients to protect, for instance, organs at risk. Organ motion is classified into two categories:

1. *Inter-fractional organ motion:* Inter-fractional organ motion refers to changes in the patient anatomy as well as changes of the positions of the target volume and nearby organs on timescales, which a larger than the duration of a fraction of fractionated radiotherapy deliveries (*i.e.,* several minutes to half an hour). It includes, for example, changes due to patient positioning, bladder or rectal filling, body fat loss and tumor shrinkage.

2. *Intra-fractional organ motion:* Intra-fractional organ motion refers to anatomy changes, which occur during the actual delivery of radiotherapy fractions. Predominant sources of intra-fractional motion are respiration for lesions in the lung or the upper abdomen, and digestion for lesions in the lower abdomen.

The uncertainties introduced by organ motion are most commonly handled through the introduction of population-based safety margins (Van Herk, 2004). Hereby, the spatial extent of a dose distribution with possibly perfect conformity to the target volume is intentionally increased to guarantee a high dose-coverage of the target volume in spite of the presence of organ motion. The disadvantage of this strategy is an increased dose to nearby healthy tissues and the correspondingly increased risk of radiation induced side effects. The aim of motion adaptive radiotherapy deliveries is to compensate for organ motion so that the safety margins can be reduced.

The concepts of image-guided radiotherapy (IGRT) are nowadays routinely applied to compensate for inter-fractional organ motion (Xing et al., 2006; Dawson and Jaffray, 2007; Verellen et al., 2007; Jaffray et al., 2007). The more challenging compensation of intra-fractional organ motion (in the following referred to as 'tumor tracking') is currently

a lively field of research (Keall et al., 2006b). The general procedure of tumor tracking can be divided into the following tasks:

1. Monitoring of organ motion
2. Compensation of system latency
3. Physical adaptation of the dose delivery process

Due to generally irregular organ motion patterns, accurate long term predictions of organ motion are impossible. Organ motion therefore needs to be monitored continuously during the treatment. Motion monitoring technologies are based on the detection of external surrogates (Kubo et al., 2000; Bert et al., 2005; Li et al., 2006), x-ray based detection of implanted internal fiducial markers (Shirato et al., 2000b; Berbeco et al., 2007; Poulsen et al., 2008; Fast et al., 2011a), electromagnetic tracking of implanted markers (Balter et al., 2005; Kupelian et al., 2007), or the detection of internal anatomic structures based on ultrasound imaging (Xu and Hamilton, 2006; Harris et al., 2007), magnetic resonance imaging (Cerviño et al., 2011) or marker-less x-ray imaging (Richter et al., 2010; Rottmann et al., 2010).

Processing times as well as mechanical motion constraints within any tumor tracking system prohibit an instantaneous reaction of the tracking system on an initial target movement. Especially for the rapid respiration induced organ motion, the resulting lag time leads to considerable tracking inaccuracies. System latency can be compensated by means of a forward prediction of the target motion. Prediction of respiratory motion has therefore been studied extensively using linear regression (Murphy et al., 2002; Sharp et al., 2004; Ren et al., 2007), neural networks (Isaksson et al., 2005; Murphy and Pokhrel, 2009), sinusoidal models (Vedam et al., 2004), Kalman filters (Sharp et al., 2004; Putra et al., 2008), support vector regression (Ernst and Schweikard, 2009), and kernel density estimation (Ruan, 2010).

For the third part of tumor tracking (*i.e.,* the dose adaptation), various techniques have been proposed, such as gating the treatment beam (Shirato et al., 2000b; Kubo et al., 2000), repositioning of a robotic linear accelerator (Schweikard et al., 2004; Hoogeman et al., 2009), repositioning of the treatment couch (D'Souza and McAvoy, 2006; Wilbert et al., 2008) or a gimbals tracking system (Takayama et al., 2009; Depuydt et al., 2011).

The approach followed in this thesis is tumor tracking through real-time adaption of the aperture of a dynamic multileaf collimator (MLC) (Keall et al., 2006a; Sawant et al., 2008; McQuaid et al., 2009). Our work was based on a MLC tumor tracking system, which was previously developed at our institution (Tacke, 2009; Tacke et al., 2010). The system supported MLC tracking of rigid 3D target translation, which was detected with a linear potentiometer. Target motion prediction based on a linear extrapolation of the two latest position observation was the limiting factor for tracking accuracy.

In this thesis, we have substantially extended and improved the functionality of the previous MLC tracking system. Our guideline for the tracking system enhancements was to tailor all three parts of the tumor tracking process to the requirements of our final goal, the clinical application. Our major innovations were:

1. *Motion monitoring:* We have integrated the MLC tracking system with clinically applicable motion monitoring technologies: the electromagnetic Calypso System (Calypso Medical Technologies, Seattle, WA) and a novel x-ray imaging system, which was recently developed at our institution (Fast et al., 2011a,b). Additionally, we have developed an integrated motion monitoring system, which combines the complementary strengths of an external surrogate monitoring system and the novel x-ray imaging system. The combined system is based on a correlation model between the external and internal motion observations, which is automatically established and continuously updated by our MLC tracking control system.

2. *Target motion forward prediction:* We have systematically tested, optimized and compared four state-of-the-art respiratory motion forward prediction models for a wide range of applications beyond our tracking system. We have integrated two highly promising prediction models into the MLC tracking system to achieve accurate target tracking in spite of a relatively large latency of our tracking system. The implementation includes automatic adaptation of the prediction models to changes in the target motion breathing pattern during a tracking delivery.

3. *MLC tracking control system:* We have completely redesigned the MLC tracking control software to realize the following improvements: Firstly, the integration of MLC tracking of irregular 3D target motion applied to the delivery modes conformal radiotherapy, step-and-shoot IMRT, dynamic IMRT and rotational IMRT into one software package. Secondly, continuous automated verification of the MLC tracking performance with automated beam holds in case of tracking inaccuracies. Thirdly, graphical visualization of the MLC tracking performance to allow manual intervention in case of abnormal behavior. Fourthly, a high level of software reliability, extendability and maintainability.

The thesis is organized as follows: Chapter 2 introduces four prediction models. The models are optimized for the respiratory motion prediction problem and their respective prediction performances are compared. Chapter 3 gives an overview of currently available motion monitoring devices. It introduces methods to combine different motion monitoring devices through correlation methods and compares the accuracy of three correlation models. Chapter 4 introduces the hardware and software components of the MLC tracking system. The workflow of MLC tracking and its implementation at our system is outlined in detail. Chapter 5 presents experimental results for MLC tracking integrated with the Calypso System for motion monitoring. The presented experiments include:

tracking of regular sinusoidal motion patterns and irregular respiratory and prostate motion patterns, tracking applied to conformal radiotherapy, step-and-shoot IMRT and dynamic IMRT, as well as a comparison of tracking performances of MLC tracking and patient couch tracking. Chapter 6 presents experimental results for MLC tracking integrated with the novel x-ray imaging system for motion monitoring. The x-ray system is used both alone and in combination with external surrogate motion monitoring. Chapter 7 concludes the thesis with a summary, a general discussion of our achievements in the context of other research in the field of tumor tracking as well as suggestions for possible further enhancements of our MLC tracking system.

In accordance with the regulations of the combined faculties for the natural sciences and for mathematics of the Ruperto-Carola University of Heidelberg, parts of this work have already been published: Chapter 2 and section 5.2 have been published in two peer-reviewed journal papers (Krauss et al., 2011b) and (Krauss et al., 2011e). Parts of the work were also presented at international conferences either orally (Krauss et al., 2009, 2011d,a), or as a poster (Krauss et al., 2010, 2011c). The results of sections 5.3 and 5.4 were obtained in student projects (Menten, 2011) and (Hofmann, 2011) under joint supervision of Prof. Dr. Uwe Oelfke and the author.

2 Prediction of respiratory motion

The latencies of the intergrated MLC tracking systems presented in this thesis amount 0.50 s, 0.59 s and 0.62 s depending on the motion monitoring device (sections 5.1, 6.1.2 and 6.2.2). Especially for the rapid organ motion due to breathing, the system latency introduces considerable tracking inaccuracies. To guarantee accurate target tracking, the system latency needs to be compensated by means of a forward prediction of the target motion.

In order to select a suitable prediction model for our MLC tracking system, we have extensively tested four state-of-the-art prediction models. The performance of the prediction models depends strongly on the thorough optimization of model parameters. In the following, we present the comparative performance of the four prediction models. In contrast to previous studies, we perform extensive model parameter tuning for all prediction models to guarantee a fair comparison. The presented results are not limited to the specific settings of our tracking system, but cover a wide range of latencies and motion monitoring sampling rates.

2.1 Introduction

Every intra-fractional motion compensation system has a specific latency, which is defined as the lag time between an initial target motion and the response of the tracking system. Previously reported tracking system latencies range from several tens to several hundreds of milliseconds: (Depuydt et al., 2011) reported a latency of 0.05 s for the VERO gimbals tracking system. For respiratory gating based on radiographic detection of implanted fiducial markers, 0.09 s latency were reported (Shirato et al., 2000b). The latency of the CyberKnife robotic treatment device (Accuray, Sunnyvale, CA) could be reduced from 0.19 s to 0.12 s (Hoogeman et al., 2009). For MLC tracking, latencies ranging from 0.16 s (Keall et al., 2006a) to 0.57 s (Poulsen et al., 2010a) were reported.

Especially for systems with longer latencies, forward prediction of the breathing motion is needed to guarantee accurate target tracking. Various methods for respiratory motion prediction have been presented previously. Sharp et al. (2004) performed a comparison study of linear regression (LR) predictors, neural network (NN) predictors and a

Kalman filter. Putra et al. (2008) combined two Kalman filters to a multiple model filter. Kalet et al. (2010) used a hidden Markov model for state-based probabilistic prediction. Ruan (2010) introduced a kernel density estimation-based (KDE) predictor, which is particularly powerful for longer prediction times up to a second. Ernst and Schweikard (2009) demonstrated a superior prediction accuracy of an adaptive support vector regression (SVR) predictor compared to wavelet-based linear prediction.

All these methods learn the patient specific breathing characteristics from a training data set. Continuous predictor retraining is expected to be advantageous, at least if the patient breathing characteristics change within the course of a radiotherapy treatment.

Each of the mentioned predictors features several model parameters besides the free parameters, which are optimized during the training period. For an adaptive neural network, Murphy and Pokhrel (2009) demonstrated the importance of the model parameters on the prediction accuracy. They showed, that although the best prediction accuracy can be achieved if the model parameters are optimized on a patient-specific basis, the transition to a patient-independent set of model parameters deteriorates the prediction accuracy only slightly.

Because the three components of the breathing data sample are likely to be highly correlated, it can be advantageous to incorporate the full three-dimensional (3D) motion information into the predictor. Ruan and Keall (2010) proposed a procedure to transform the resulting high dimensional prediction problem into a lower dimensional feature space using principal component analysis (PCA) in order to avoid the 'curse of dimensionality' (Bellman, 1957).

In the following, we compare the performance of the LR, NN, KDE and SVR predictors for a variety of prediction horizons and sampling rates. We apply the predictors to twelve 3D lung tumor motion data samples. For all predictors, we investigate the effect of stationary training versus continuous retraining. We also test two modes of 3D motion processing for all predictors: three independent 1D prediction models for each coordinate, and full 3D motion processing using PCA.

We perform for each predictor at all considered latencies, sampling rates, training schemes and the two 3D motion processing modes extensive model parameter optimization through a grid search in the multi-dimensional model parameter space. Because of extensive computation times, such model parameter optimization procedures are not feasible in clinical settings. We therefore identify patient-independent model parameter sets, which yield good prediction performances for all considered breathing traces. We compare the accuracy of the predictors in the clinically applicable setting of patient-independent model parameters.

Table 2.1: Summary of the 3D breathing data characteristics.

Breathing trace	Mean amplitude [mm]			Standard deviation [mm]			Mean cycle duration [s]
	LR	SI	AP	LR	SI	AP	
1	2	6	5	0.5	2.1	1.8	3.2
2	2	8	6	0.4	2.9	2.2	3.0
3	3	8	5	0.9	2.8	1.5	3.5
4	3	8	6	0.7	2.7	1.8	3.7
5	1	9	1	0.3	3.4	0.2	2.4
6	10	2	1	3.6	0.8	0.2	3.4
7	2	12	2	0.7	4.1	0.6	4.4
8	1	10	3	0.2	3.3	0.7	5.6
9	2	13	5	0.7	5.0	1.9	3.0
10	2	14	5	1.1	6.8	2.4	2.9
11	3	9	8	1.0	3.2	3.1	3.1
12	3	8	7	1.0	2.9	2.6	2.9

2.2 Materials and Methods

2.2.1 Patient breathing data

A total of twelve breathing data samples was studied. The samples were acquired during respiratory gated radiotherapy treatments of six lung cancer patients on two radiotherapy fractions in each case. Internal 3D lung tumor motion was assessed through stereoscopic x-ray fluoroscopy tracking of gold markers, which were implanted into the lung tumors of the patients, at a imaging rate of 30 Hz (Berbeco et al., 2005). Breathing data characteristics are listed in 2.2.1.

The first 83 s of each sample were split up into a 40 s training data set and a 40 s test data set, on which the predictive performance was assessed. To simulate a realistic treatment workflow, a 3 s period between the training and the test data set was reserved for computation time.

2.2.2 Data preparation

The breathing data sets were expressed as uniformly sampled timeseries

$$\left\{ \boldsymbol{s_i} := \boldsymbol{s}(t_i) = \left(s^1(t_i), s^2(t_i), s^3(t_i)\right)^T \mid i \in [1, N] \right\}. \tag{2.1}$$

The superscript index labels the euclidean coordinates of the 3D tumor position $\boldsymbol{s}_j$ at discrete point in time t_j. N is the total number of recorded positions.

For the considered predictors, pairs of input vectors and target scalars

$$\left\{ \left(\boldsymbol{x}_i^k, y_i^k \right) \mid i \in [1, N] \,,\ k \in [1, 3] \right\} \tag{2.2}$$

were constructed from the breathing data samples. The subscript index labels points in time t_j, the superscript index labels the euclidean coordinates. The p-dimensional input vectors $\boldsymbol{x}_j^k$ were constructed from the history of past tumor positions $\{ \boldsymbol{s}_i \mid i \leq j \}$. For the lookahead length τ, the target vectors $\boldsymbol{y}_j = \left(y_j^1, y_j^2, y_j^3 \right)^T$ were given as the breathing data signal τ time steps ahead: $\boldsymbol{y}_j = \boldsymbol{s}_{j+\tau}$. If τ was not a multiple of the sampling interval $t_j - t_{j-1}$, the target vectors were determined through linear interpolation.

Preprocessing.

Data preprocessing was performed to be robust against baseline drifts and large amplitude fluctuations. For each point in time t_j, an offset value a_j^k and a scaling factor b_j^k was calculated for each coordinate k, such that the past 7 s of the breathing data $\left\{ s^k(t_i) \mid t_i \in [t_{j-N_{\mathrm{sw}}}, t_j] \right\}$ had zero mean and unity variance:

$$\begin{aligned} a_j^k &= \frac{1}{N_{\mathrm{sw}}} \sum_{i\,=\,j-N_{\mathrm{sw}}}^{j} s^k(t_i) \,, \\ b_j^k &= \left(\frac{1}{N_{\mathrm{sw}}(N_{\mathrm{sw}}-1)} \sum_{i\,=\,j-N_{\mathrm{sw}}}^{j} \left(s^k(t_i) - a_j^k \right)^2 \right)^{1/2} . \end{aligned} \tag{2.3}$$

N_{sw} is the number of positions within the 7 s sliding window.

These normalization values were applied to each pair of input vectors and target scalars as described in the following section. The prediction itself as well as predictor training was performed using the normalized input vectors and target scalars. For prediction accuracy assessment, the predicted positions were back-transformed using the stored normalization values.

3D motion data processing.

The preparation of the pairs of input vectors $\boldsymbol{x}_j^k$ and normalized target scalars $y_{j,norm}^k$ was different for the two ways of 3D breathing motion processing:

1. *Coordinate-wise prediction:* Three independent input vectors were established for each coordinate respectively. To allow for input vectors, which span a relatively large time window without being composed of too many elements, the lag length $\delta \in \mathbb{N}$ of successive input vector entries was introduced. Using the normalization values a_j^k and b_j^k from 2.3, the input vectors and target scalars were given as

$$\begin{aligned} \boldsymbol{x}_j^k &= \left(\, s_{j-\delta(p-1)}^k - a_j^k \, , \, s_{j-\delta(p-2)}^k - a_j^k \, , \, \ldots \, , \, s_j^k - a_j^k \, \right)^T \, / \, b_j^k \, , \\ y_{j,norm}^k &= (\, s_{j+\tau}^k - a_j^k \,) \, / \, b_j^k \, . \end{aligned} \tag{2.4}$$

2. *Multidimensional prediction:* A common input vector for the three coordinates was established, which contained the 3D information of the past breathing data samples. The superscript index of the input vectors $\boldsymbol{x}_j^k$ could therefore be omitted. For normalization, scaling factors $b_j = \max(\left\{ b_j^k \mid k \in [1,3] \right\})$ and offset values $\boldsymbol{a}_j = (a_j^1, a_j^2, a_j^3)^T$ from 2.3 were used to produce the $3p$-dimensional vectors

$$\tilde{\boldsymbol{x}}_j = \left(\, \boldsymbol{s}_{j-\delta(p-1)} - \boldsymbol{a}_j \, , \, \boldsymbol{s}_{j-\delta(p-2)} - \boldsymbol{a}_j \, , \, \ldots \, , \, \boldsymbol{s}_j - \boldsymbol{a}_j \, \right)^T \, / \, b_j \, . \tag{2.5}$$

   In order to avoid the 'curse of dimensionality', the vector $\tilde{\boldsymbol{x}}_j$ was transferred into a lower dimensional feature space using PCA (Ruan and Keall, 2010): The covariance matrix $\Sigma_{\tilde{x}}$ of the vectors $\tilde{\boldsymbol{x}}_j$ of the training data set was estimated. An eigenanalysis of $\Sigma_{\tilde{x}}$ was performed and the vectors $\tilde{\boldsymbol{x}}_j$ were transformed into the space spanned by the first p eigenvectors $\boldsymbol{v}_j$ of $\Sigma_{\tilde{x}}$. Input vectors and target scalars were then given as:

$$\begin{aligned} \boldsymbol{x}_j &= (\, \boldsymbol{v}_1 \tilde{\boldsymbol{x}}_j \, , \, \ldots \, , \, \boldsymbol{v}_p \tilde{\boldsymbol{x}}_j \,)^T \, , \\ y_{j,norm}^k &= (\, s_{j+\tau}^k - a_j^k \,) \, / \, b_j \, . \end{aligned} \tag{2.6}$$

2.2.3 The predictors

The following paragraphs give a short description of the considered predictors. The formulas apply to one-dimensional prediction problems defined by pairs of p-dimensional input vectors and target scalars $(\boldsymbol{x}_j, y_j)$. A prediction function $f\colon \mathbb{R}^p \rightarrow \mathbb{R}$ is inferred from the training data set $\{ \, (\boldsymbol{x}_i, y_i) \mid i \in [1, N_{\text{tr}}] \, \}$. N_{tr} is the number of training data examples. $f(\boldsymbol{x})$ is the predicted position of a test input vector $\boldsymbol{x}$.

To predict 3D breathing motion data, three prediction functions $\{ \, f_i \mid i \in [1,3] \, \}$ were established. For coordinate-wise data processing, predicted positions were given as $\hat{\boldsymbol{y}}_{norm} = (f_1(\boldsymbol{x}^1), f_2(\boldsymbol{x}^2), f_3(\boldsymbol{x}^3))^T$. For multidimensional data processing, predicted positions were given as $\hat{\boldsymbol{y}}_{norm} = (f_1(\boldsymbol{x}), f_2(\boldsymbol{x}), f_3(\boldsymbol{x}))^T$.

Both the prediction itself and the predictor training was based on the input vectors and target scalars 2.4 and 2.6, which were preprocessed using the normalization values 2.3. For prediction accuracy assessment, the predicted values $\hat{\boldsymbol{y}}_{j,norm} = (\hat{y}^1_{j,norm}, \hat{y}^2_{j,norm}, \hat{y}^3_{j,norm})^T$ were back-transformed to $\hat{\boldsymbol{y}}_j = (\hat{y}^1_j, \hat{y}^2_j, \hat{y}^3_j)^T$ using the stored normalization values

$$\hat{y}^k_j \;=\; \begin{cases} b^k_j \cdot \hat{y}^k_{j,norm} + a^k_j & \text{for coordinate-wise prediction} \\ b_j \cdot \hat{y}^k_{j,norm} + a^k_j & \text{for multidimensional prediction.} \end{cases} \tag{2.7}$$

Linear (ridge) regression.

The regression function is a multi-dimensional linear map of the input vector:

$$f(\boldsymbol{x}) \;=\; \boldsymbol{\beta}^T \boldsymbol{x} + \beta_0, \tag{2.8}$$

using the coefficient vector $\boldsymbol{\beta} = (\beta_1, \ldots, \beta_p)^T$. Because of data preprocessing to zero mean values, we fixed the offset term β_0 to zero in all calculations.

For ridge regression, the loss function to be minimized is the penalized residual sum of squares:

$$R(\beta) \;=\; \sum_{i=1}^{N_{\text{tr}}} (y_i - f(\boldsymbol{x}_i))^2 + \lambda \|\boldsymbol{\beta}\|^2, \tag{2.9}$$

with the regularization parameter $\lambda \geq 0$. The regularization term shrinks the magnitude of the coefficient vector $\boldsymbol{\beta}$, which leads to a reduction of the noise level of the prediction signal (Hastie et al., 2001). If the matrix $\mathbf{X}$ is defined such that its rows equal the input vectors $\boldsymbol{x}_j$ of the training data, and the vector $\mathbf{Y}$ is defined such that its entries equal the targets y_j of the training data, $R(\boldsymbol{\beta})$ is minimized by:

$$\hat{\boldsymbol{\beta}} \;=\; (\mathbf{X}^T\mathbf{X} + \lambda \mathbf{I})^{-1} \mathbf{X}^T \mathbf{Y}. \tag{2.10}$$

There is no need of an iterative optimization to train the regression function.

Neural networks.

We considered only multilayer perceptrons (MLP) with a single layer of hidden neurons and a linear output neuron. The MLP prediction function can be expressed as:

$$f(\boldsymbol{x}) \;=\; \boldsymbol{\beta}^T \boldsymbol{\Phi}(\boldsymbol{x}) + \beta_0. \tag{2.11}$$

using the coefficient vector $\boldsymbol{\beta} = (\beta_1, \ldots, \beta_{N_{\text{h}}})^T$ and the number of hidden neurons N_{h}. The transformation function $\boldsymbol{\Phi}(\boldsymbol{x}) = (\Phi_1(\boldsymbol{x}), \ldots, \Phi_{N_{\text{h}}}(\boldsymbol{x}))^T$ consists of non-linear activation functions σ applied to a linear combination of the input vector entries:

$$\Phi_m(\boldsymbol{x}) \;=\; \sigma\left(\boldsymbol{\omega}^T_m \boldsymbol{x} + \omega_{m0}\right), \tag{2.12}$$

with the weights $\boldsymbol{\omega}_m = (\omega_{m1}, \ldots, \omega_{mp})^T$ and ω_{m0} and the sigmoid activation function $\sigma : \mathbb{R} \rightarrow (0, 1)$ given as $\sigma(v) = 1/(1 + e^{-v})$.

We chose *weight decay* regularization to overcome the problem of over-fitting, which is often observed for neural networks. The network weights are shrunk through a penalized residual sum of squares:

$$R(\beta, \omega) = \sum_{i=1}^{N_{\text{tr}}} (y_i - f(\boldsymbol{x}_i))^2 + \lambda \left(\|\boldsymbol{\beta}\|^2 + \sum_{m,i} \omega_{mi}^2 \right). \tag{2.13}$$

The minimization of 2.13 is a non-convex optimization problem. The solution obtained by any gradient-based optimizer is consequently highly dependent on the choice of the starting weights. We therefore trained five independent networks with randomly initialized starting weights in parallel and averaged the obtained predictions. Optimization was performed using the R-package nnet (Venables and Ripley, 2002).

Kernel density estimation.

In KDE as proposed by Ruan and Keall (2010), prediction is performed through a weighted sum of the targets of the training data sample:

$$f(\boldsymbol{x}) = \mathcal{N} \sum_{i=1}^{N_{\text{tr}}} \omega_i \, y_i, \tag{2.14}$$

with the normalization parameter $\mathcal{N} = \left(\sum \omega_i\right)^{-1}$. The weights quantify 'closeness' to the input vectors of the training data by means of a kernel function $K(\boldsymbol{x}, \boldsymbol{x'})$. We chose the popular Gaussian kernel

$$K_\gamma(\boldsymbol{x}, \boldsymbol{x'}) = \exp\left(-\gamma \|\boldsymbol{x} - \boldsymbol{x'}\|^2\right), \tag{2.15}$$

with the kernel parameter $\gamma > 0$. Predictions are performed by computing the weights $w_j = K_\gamma(\boldsymbol{x}, \boldsymbol{x}_j)$ and inserting them into 2.14.

Support vector regression.

SVR can be expressed as a basis expansion method:

$$f(\boldsymbol{x}) = \boldsymbol{\beta}^T \boldsymbol{\Phi}(\boldsymbol{x}) + \beta_0. \tag{2.16}$$

The coefficient vector of the prediction function is computed by solving the optimization problem:

$$\min_{\boldsymbol{\beta}} \quad \frac{1}{2}\|\boldsymbol{\beta}\|^2 + C \sum_{i=1}^{N_{\text{tr}}} (\xi_i + \xi_i^*) \tag{2.17a}$$

subject to

$$\begin{aligned} y_j - \left(\boldsymbol{\beta}^T \boldsymbol{\Phi}(\boldsymbol{x}_j) + \beta_0\right) &\leq \epsilon + \xi_j \,, \\ \left(\boldsymbol{\beta}^T \boldsymbol{\Phi}(\boldsymbol{x}_j) + \beta_0\right) - y_j &\leq \epsilon + \xi_j^* \,, \\ \xi_j, \xi_j^* &\geq 0 \,. \end{aligned} \tag{2.17b}$$

The residual sum of squares is replaced by an 'ϵ-insensitive' error measure. The slack-variables ξ_j, ξ_j^* correspond to the distance of a predicted value $f(\boldsymbol{x}_j)$ to a ϵ-tube around the targets y_j of the training data (2.17b). Deviations smaller than ϵ do not contribute to the loss function (2.17a). The regularization term in (2.17a) is weighted through the cost parameter C.

Using the kernel function $K(\boldsymbol{x}, \boldsymbol{x'}) = \boldsymbol{\Phi}(\boldsymbol{x})^T \boldsymbol{\Phi}(\boldsymbol{x'})$, the SVR problem can be reformulated such that the transformation functions $\boldsymbol{\Phi}(\boldsymbol{x})$ enter only implicitly in form of inner products (Vapnik, 1998):

$$f(\boldsymbol{x}) = \sum_{i=1}^{N_{\text{tr}}} (\alpha_i - \alpha_i^*) K(\boldsymbol{x}, \boldsymbol{x}_i) + \beta_0 \,. \tag{2.18}$$

The coefficients α_j, α_j^* are computed by solving the optimization problem

$$\begin{aligned} \min_{\alpha_i, \alpha_i^*} \quad & \epsilon \sum_i (\alpha_i + \alpha_i^*) - \sum_i y_i (\alpha_i - \alpha_i^*) \\ & + \frac{1}{2} \sum_{i,j} (\alpha_i - \alpha_i^*)(\alpha_j - \alpha_j^*) K(\boldsymbol{x}_i, \boldsymbol{x}_j) \end{aligned} \tag{2.19a}$$

subject to

$$\begin{aligned} 0 \leq \alpha_j, \alpha_j^* &\leq C \,, \\ \sum_i (\alpha_i - \alpha_i^*) &= 0 \,, \\ \alpha_j \alpha_j^* &= 0 \,. \end{aligned} \tag{2.19b}$$

This so-called 'kernel trick' allows for implicitly solving a basis expansion problem for transformation functions $\boldsymbol{\Phi}$ mapping into infinite-dimensional feature spaces. After an appropriate kernel function is selected, the infinite sum (2.16) is replaced by a sum over the training instances (2.18).

We solved the optimization problem (2.19a) using the R-package `e1071`, which provides an R-interface to the LIBSVM package by Chang and Lin (2001). As kernel function, we chose the previously defined Gaussian kernel (2.15).

2.2.4 Prediction scenarios

Besides the distinction between coordinate-wise and full 3D prediction (2.2.2), the following scenarios were considered.

Latency and sampling rate.

Two design parameters of a predictor for real-time tumor tracking are determined by the characteristics of the specific tracking system:

1. *Latency:* The total system latency determines the lookahead length τ of the predictor. We have considered values of 0.2 s, 0.4 s and 0.6 s to cover the range of typical latency values for real-time tumor tracking systems.

2. *Sampling rate:* The breathing data sampling rate is determined by the real-time motion monitoring system. We have considered values of 30 Hz, 15 Hz and 7.5 Hz. 30 Hz was the sampling rate of the considered breathing data samples. Downsampling was performed to cover the range of typical sampling rates from 30 Hz for the real-time position management system (RPM system, Varian Medical, Palo Alto, CA) and 25 Hz for the research real-time data stream of the Calypso System (Calypso Medical Technologies, Seattle, WA) (Krauss et al., 2011e) down to 7 Hz or 5 Hz for linac-mounted flat panel imagers (Cho et al., 2009; Poulsen et al., 2010a).

Training schemes.

Retraining of the predictors is expected to improve predictions, especially if breathing patterns change their characteristics during the course of a radiotherapy treatment. We investigated three different training schemes:

1. *Stationary:* The predictor is trained once on a 40 s training data window.

2. *Adaptive:* The predictor is retrained every 3 s on a 40 s training data window, which is sequentially shifted towards newer target position observations.

3. *Adaptive-expansive:* The predictor is retrained every 3 s. The training data window is sequentially expanded from 40 s to 67 s. The 67 s training window is then shifted towards newer target position observations.

For the adaptive training schemes, the updated predictors were applied to the data samples that were acquired 3 s after the last sample in the training data set. This emulated the process of a real-time adaptive filter, which needs 3 s of computation time for retraining. These 3 s of computation time were for all the considered predictors a very conservative estimate on a standard 3 GHz processor.

Table 2.2: Parameters of the predictors. Free parameters are obtained through predictor training. Model parameters must be selected prior to training. General parameters apply to every predictor.

Predictor	Free parameters	Model parameters
LR	β_j	regularization parameter λ
NN	β_j, ω_{mj}	number of hidden neurons $N_{\mathbf{h}}$ weight decay parameter λ
KDE	none	kernel parameter γ
SVR	α_j, α_j^*, β_0	tube width ϵ cost parameter C kernel parameter γ
general		input vector dimension p lag length δ

2.2.5 Model parameter selection

Every respiratory motion predictor can be adjusted to a specific prediction scenario through the choice of several model parameters. These model parameters cannot, as opposed to the free parameters, be optimized through predictor training. They can be divided into general model parameters, which apply to every predictor, and predictor specific model parameters. An overview of the relevant parameters is listed in table 2.2.

The number of model parameters ranges from 3 to 5 for the selected predictors. Since these parameters influence each other, they cannot be optimized individually. We therefore implemented an extensive grid search in the 3- to 5-dimensional model parameter space to optimize the model parameters.

Optimum model parameters depend on the prediction scenario (section 2.2.4) as well as on the specific patient breathing characteristics. Because of the extensive computation times for a grid search in the model parameter space, we aimed to find a set of model parameters, which is optimal for the population of considered breathing patterns. For each breathing pattern, each latency, each sampling rate and each training scheme, we optimized all the model parameters given in table 2.2 for all considered predictors in both the coordinate-wise and full 3D data preparation mode.

The optimum, patient-independent model parameter set was identified by minimizing the average of the prediction errors of the twelve individual breathing patterns. For the comparison of the different prediction methods, the best patient-independent model parameter configuration as well as the best training scheme and 3D data processing mode was selected for each latency and sampling rate.

2.2.6 Prediction accuracy measures

Prediction errors were quantified as root mean squared deviations between predicted positions $\hat{\boldsymbol{y}}_j$, which were back-transformed using (2.7), and actual target positions $\boldsymbol{y}_j = \boldsymbol{s}_{j+\tau}$ of the test data set:

$$\text{RMSE} = \sqrt{\frac{\sum_i \|\hat{\boldsymbol{y}}_i - \boldsymbol{y}_i\|^2}{N_{\text{te}}(N_{\text{te}} - 1)}} \ . \tag{2.20}$$

N_{te} is the number of test data examples. The gain in prediction accuracy compared to using no prediction was expressed as normalized prediction error:

$$\text{normalized RMSE} = \frac{\text{RMSE(prediction)}}{\text{RMSE(no prediction)}} \ . \tag{2.21}$$

Changes in prediction accuracy for different model parameter sets were compared through relative root mean squared prediction error changes:

$$\text{relative RMSE change} = \frac{\text{RMSE(parameter set 1)}}{\text{RMSE(parameter set 2)}} - 1 \ . \tag{2.22}$$

2.2.7 Box plots

Distributions of prediction accuracies were displayed as box and whisker plots (Chambers, 1983). The bottom, middle and top of the box represents the lower quartile, the median and the upper quartile, respectively. The whiskers extend to the lowest data point which is still within 1.5 times the interquartile range of the lower quartile, and the highest data point which is still within 1.5 times the interquartile range of the upper quartile. Outside observations are displayed individually.

2.3 Results

Figure 2.1 shows the impact of the transition from patient-specific optimal to patient-average optimal model parameters for all prediction scenarios (section 2.2.4). Displayed are distributions of the relative prediction accuracy loss, that is the increase of the prediction error using the common parameter set relative to the prediction error using individually optimal model parameters (section 2.2.6). On a patient level (2.1a), some cases of extremely high accuracy losses of up to 60 % are observed for both the KDE and SVR predictors. For the majority of cases, a moderate accuracy loss is observed, with the third quartile being well below 20 %. If we average over the twelve patient traces (2.1b), no losses higher than 12 % are observed.

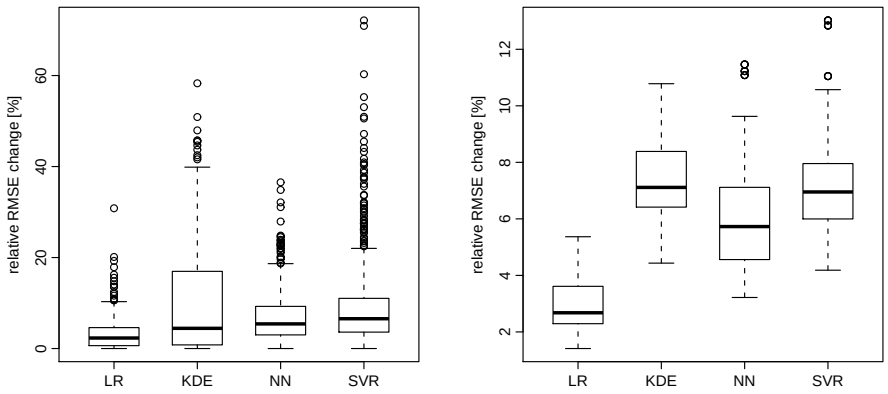

(a) all motion traces (b) average over patient traces

Figure 2.1: Prediction accuracy loss for patient-independent model parameters relative to patient-specific model parameter optimization.

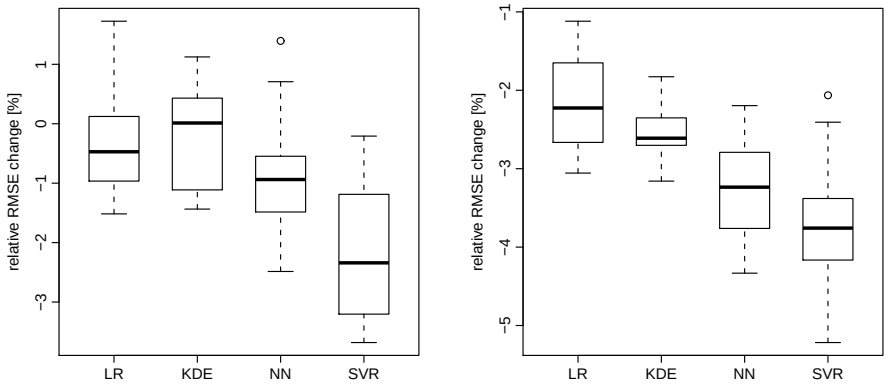

(a) adaptive retraining (b) adaptive-expansive retraining

Figure 2.2: Prediction accuracy gain of adaptive retraining schemes relative to stationary training.

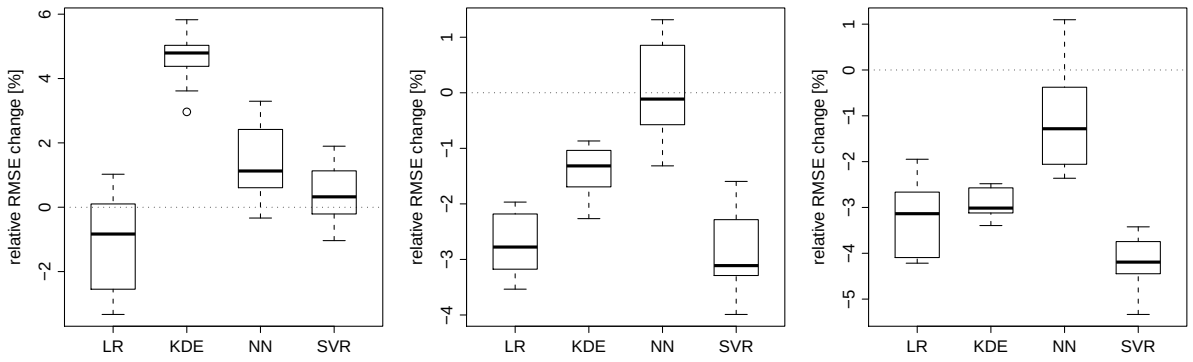

(a) latency 0.2 s (b) latency 0.4 s (c) latency 0.6 s

Figure 2.3: Prediction accuracy changes of 3D prediction using PCA relative to independent coordinate-wise prediction.

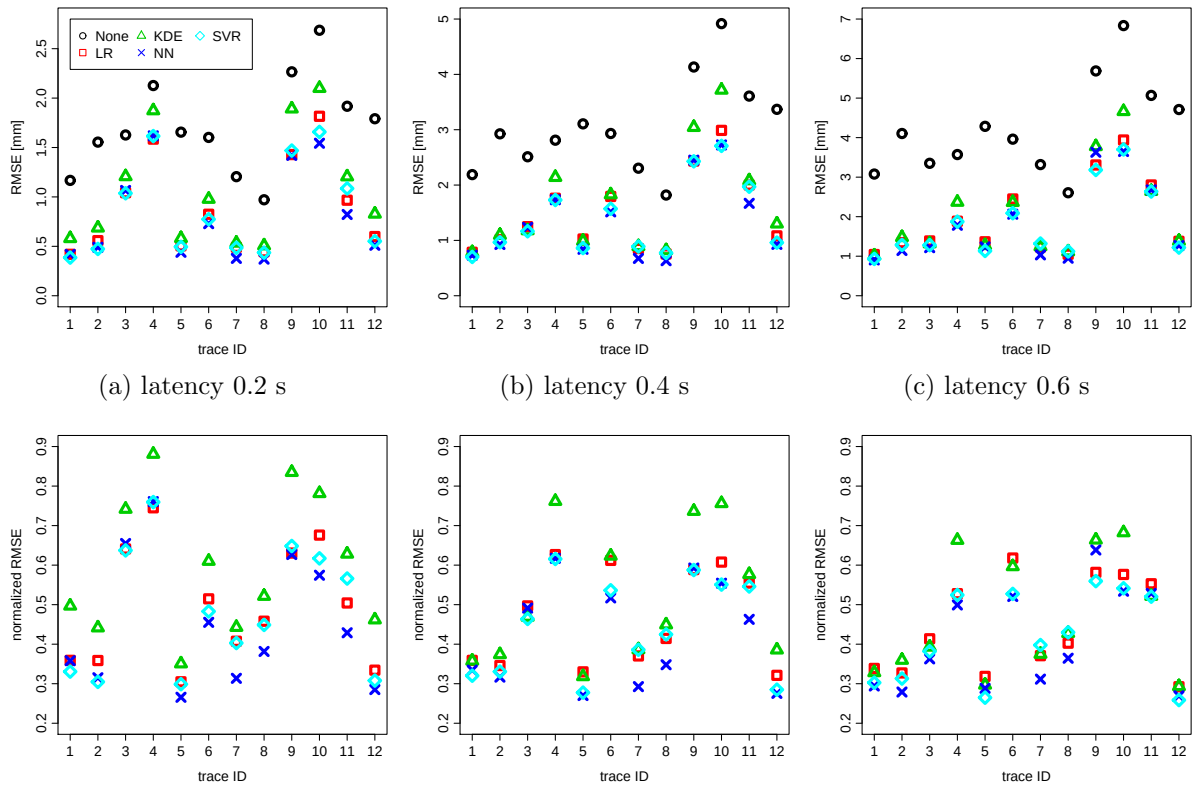

(a) latency 0.2 s (b) latency 0.4 s (c) latency 0.6 s

(d) latency 0.2 s (e) latency 0.4 s (f) latency 0.6 s

Figure 2.4: Comparison of prediction errors for individual breathing traces and latencies of 0.2 s, 0.4 s and 0.6 s (left to right) and a sampling rate of 15 Hz. Absolute errors (upper row) and errors normalized to using no prediction (lower row).

Figure 2.2 shows the gain in prediction accuracy of the adaptive retraining schemes relative to stationary predictor training (section 2.2.4), averaged over the breathing traces. The impact on the prediction accuracy is surprisingly small, with third quartile improvements of up to 3 % for adaptive retraining (2.2a) and up to 4 % for adaptive-expansive retraining (2.2b). There are even some scenarios, where the prediction accuracy on the patient average level is decreased through adaptive retraining. Adaptive-expansive retraining in contrast is favorable in all scenarios.

Figure 2.3 shows the impact on prediction accuracy of full 3D processing using PCA relative to three independent coordinate-wise predictors (section 2.2.2). We observe small improvements for the longer latencies of 0.4 s and 0.6 s except for the NN predictor, for which no trend can be observed at 0.4 s latency. Except for the LR predictor, deteriorations at 0.2 s latency are observed when changing to full 3D processing.

Figure 2.4 shows the comparative prediction performance of the four predictors for the twelve patient breathing traces at the considered latencies for a 15 Hz sampling rate. Prediction method ‘none’ refers to using the last position observation as prediction value.

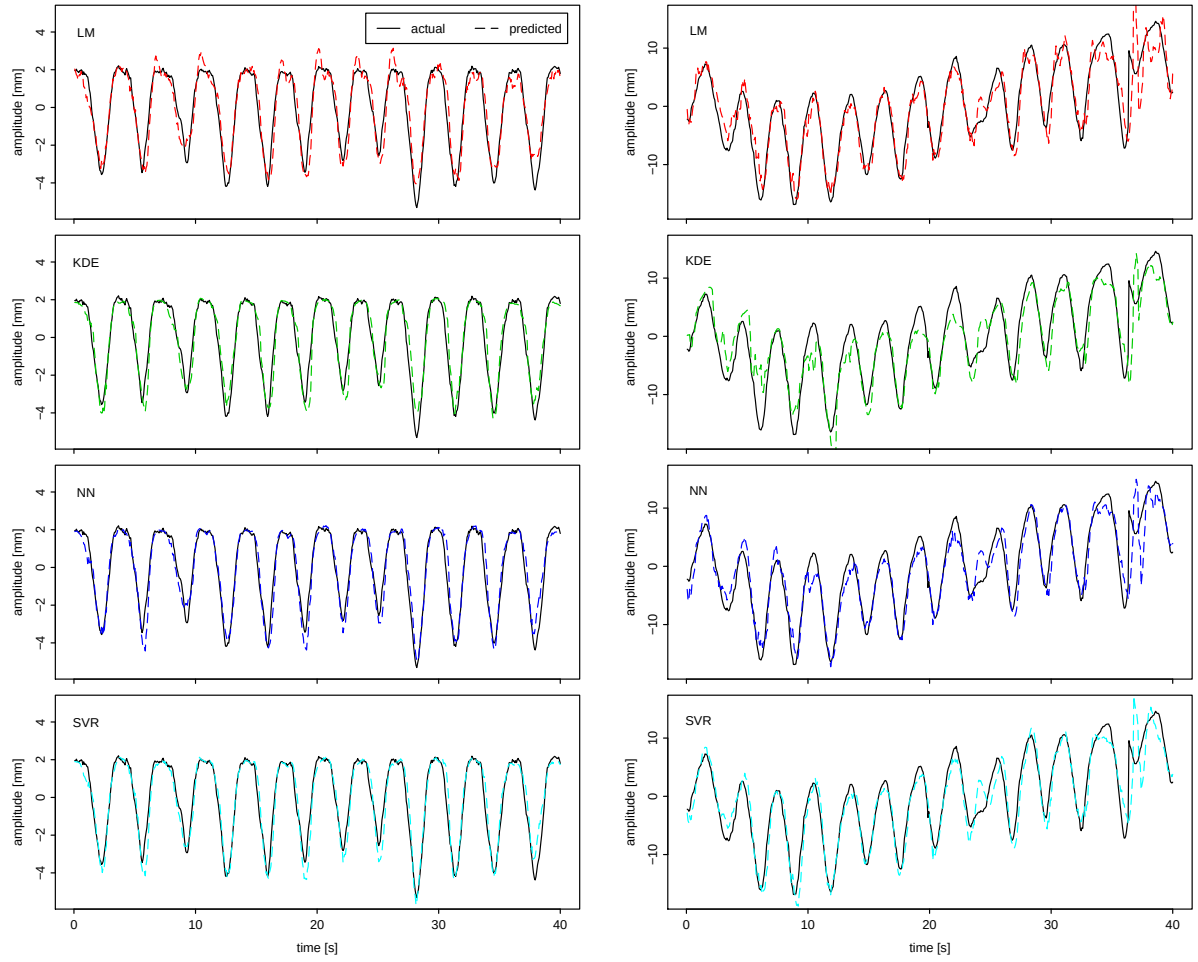

Figure 2.5: Actual breathing signal in superior-inferior direction and corresponding predictions for 0.4 s latency and 15 Hz sampling rate. The y-axis scaling for breathing trace 10 (right) is three times higher than for trace 1 (left).

Displayed are prediction results using patient-independent model parameters for all predictors and the adaptive-expansive retraining scheme, which proved advantageous for all predictors in all scenarios (2.2b). Full 3D versus coordinate-wise predictor setup is selected according to the patient averaged prediction accuracy of the current scenario. The lower row displays the prediction accuracy using the individual predictors divided by using no prediction. KDE yields the worst predictions and NN the best predictions for almost all breathing patterns.

Figure 2.5 shows actual breathing signals in superior-inferior direction and the corresponding predictions for 0.4 s latency and 15 Hz sampling rate. The displayed breathing traces 1 and 10 show the range from sub-millimeter to around three-millimeter prediction accuracy. Prediction was performed using patient-independent model parameters.

Figure 2.6 shows the comparison of the prediction errors averaged over the breathing

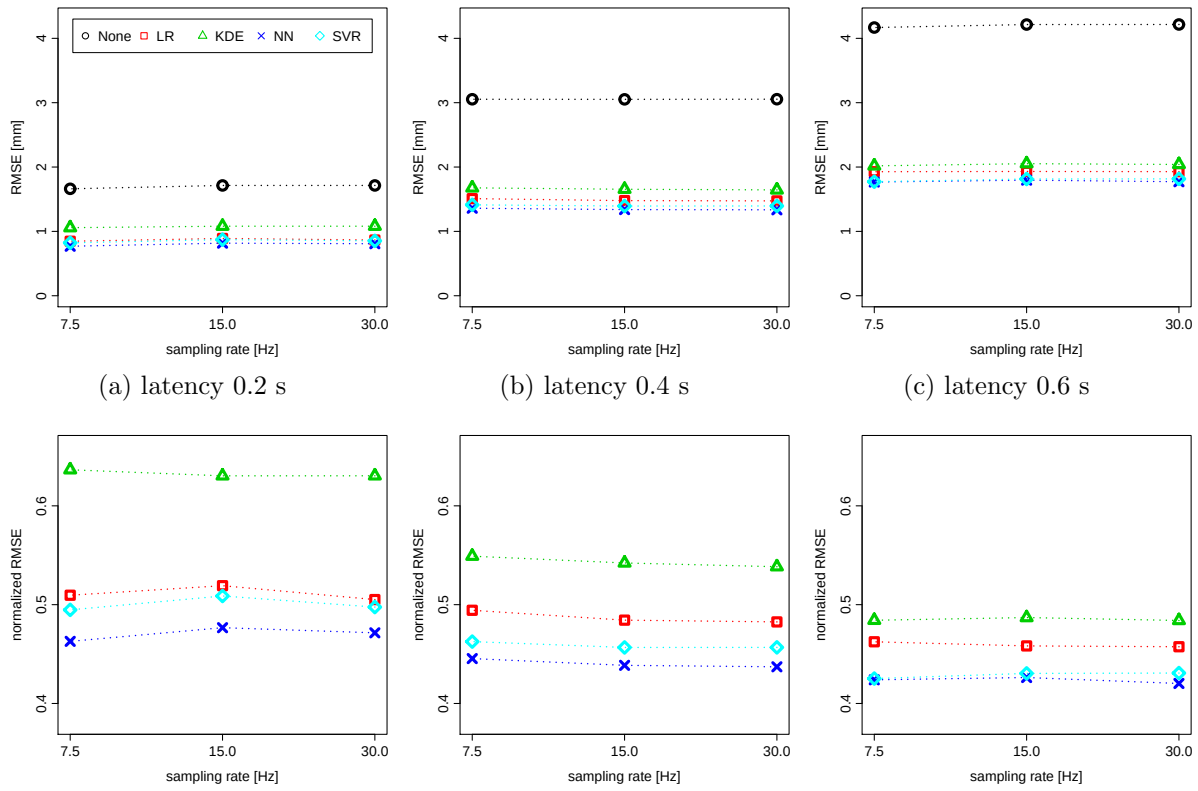

(a) latency 0.2 s (b) latency 0.4 s (c) latency 0.6 s

(d) latency 0.2 s (e) latency 0.4 s (f) latency 0.6 s

Figure 2.6: Comparison of prediction errors averaged over patient traces for latencies of 0.2 s, 0.4 s and 0.6 s (left to right). Absolute errors (upper row) and errors normalized to using no prediction (lower row).

traces. Absolute prediction errors (upper row) depend strongly on the latency. Prediction errors increase roughly linear from 1 mm for 0.2 s latency to 2 mm for 0.6 s latency. The prediction errors normalized to using no prediction (lower row) show no strong dependency on the latency. All predictors roughly halve the errors of using no prediction in all scenarios. An effect of the sampling rate is almost not observable. From the lower row, we can deduce a ranking of the predictors. Although the differences are small, the NN outperforms the others, followed by SVR and LR. Especially for 0.2 s latency, KDE performs clearly worst.

Table 2.3 summarizes the results of figure 2.6. Displayed are absolute and relative RMS prediction errors averaged over both the breathing traces and the three sampling rates.

Table 2.3: Prediction errors averaged over both breathing traces and sampling rates for the different latencies. Absolute root mean squared prediction errors (RMSE) and RMSE normalized to using no prediction.

	absolute RMSE [mm]			normalized RMSE		
	latency			latency		
Predictor	0.6 s	0.4 s	0.2 s	0.6 s	0.4 s	0.2 s
LR	1.93	1.49	0.87	0.46	0.49	0.51
KDE	2.04	1.66	1.07	0.49	0.54	0.63
NN	1.78	1.34	0.80	0.42	0.44	0.47
SVR	1.80	1.40	0.85	0.43	0.46	0.50

2.4 Discussion

All the considered predictors allowed selecting a patient-independent model parameter set. Although a few cases of strong deteriorations in prediction accuracy were observed on the patient-specific level, prediction accuracy losses on a patient-average level were small. The third quartile of the accuracy loss distributions was 4% for LR prediction and 8% for KDE, NN and SVR prediction.

The impact of adaptive retraining schemes was found to be relatively small. On a patient-average level, no improvements larger than 5% were observed. The sliding window adaptive training even yielded deteriorations compared to stationary training in several scenarios. These findings contrast the previously reported strong improvements of adaptive retraining for KDE (Ruan, 2010). In the present study, baseline and amplitude drifts were eliminated through data preprocessing (section 2.2.2), which reduced the need of adaptive retraining.

The effects of full 3D data processing using PCA were below 5%. Moderate improvements were observed for LR, KDE and SVR prediction for the larger latencies of 0.4 s and 0.6 s. KDE prediction was degraded at 0.2 s latency. The NN predictor showed almost no effects.

The predictor comparison was based on adaptive-expansive retraining and on patient-independent model parameters, which were optimized for each latency and sampling rate individually. 3D data processing mode was also selected for each predictor in each scenario individually. Because almost no effect of the breathing data sampling rate in the considered range from 30 Hz to 7.5 Hz was observed, prediction errors were averaged over all sampling rates to produce the results of table 2.3. Although the differences between the predictors were small, figure 2.6 allowed deducing a clear ranking between the predictors: The NN outperformed the others at all latencies and sampling rates.

RMS prediction errors normalized to using no prediction, averaged over all latencies and sampling rates were 0.44, 0.46, 0.49 and 0.55 for the NN, SVR, LR and KDE predictors, respectively. Prediction errors relative to the NN deteriorated accordingly only by 4%, 9% and 24% for SVR, LR and KDE.

Ruan (2010) demonstrated clear advantages of KDE over LR prediction; the opposite was found in our comparison study. Advantages of NN and SVR prediction over LR prediction reported by Murphy and Dieterich (2006) and Riaz et al. (2009), were by far more pronounced than our results. The contrary findings of our comparison study supposedly result from the extensive model parameter tuning, which improved the LR prediction considerably. In addition, Murphy and Dieterich (2006) used an iterative optimization scheme for the parameter vector $\boldsymbol{\beta}$, which did not converge for some breathing traces; a problem, which can not occur with the non-iterative training scheme depicted in section 2.2.3.

2.5 Conclusions

After thorough model parameter optimization on a patient-average basis, all the considered predictors succeeded in adapting to the patient-specific breathing motion in spite of a common set of model parameters for all considered breathing traces. All studied predictors roughly halved prediction errors compared to using no prediction. A ranking between the predictors could be deduced: When averaging over all latencies and sampling rates, the NN outperformed the SVR, LR and KDE predictors by 4%, 9% and 24%, respectively.

The relatively small differences between the predictors indicate that an appropriate choice of patient-independent model parameters is supposedly more important than the choice of the actual prediction method. Especially the good performance of the LR predictor contrasts the findings of previously published comparison studies. We therefore recommend that future assessments of the benefits of new prediction methods should thoroughly consider model parameter tuning of the benchmark methods to achieve fair comparisons.

3 Motion monitoring and correlation models

Tumor tracking requires precise knowledge of tumor positions throughout the treatment. An ideal motion monitoring system would provide 3D tumor and surrounding organ position information including organ displacement, deformation and rotation - optimally at a high frame-rate, with a short latency. Additionally, the ideal motion monitoring would be non-invasive and would not deliver x-ray imaging dose to the patient.

In the following we will introduce several motion monitoring technologies. None of these technologies can fulfill the aforementioned requirements to an ideal motion monitoring device. Internal motion monitoring is often invasive and restricted to the detection of single point translations. External surrogate monitoring relies on a strong correlation between surrogate and organ motion. Combining different modalities is often beneficial; the mathematics of combining external surrogate monitoring and x-ray imaging will be discussed in section 3.2.

3.1 Internal motion monitoring

3.1.1 The Calypso System

The Calypso System (Calypso Medical Technologies, Seattle, WA) can detect internal organ motion at a high frame-rate without delivering ionizing radiation to the patient (Balter et al., 2005). It is based on three electromagnetic transponders, which are implanted either close to or inside the treatment target (figure 3.1b). The transponders are essentially electromagnetic resonant circuits inside a glass capsule (diameter 1.8 mm, length 8 mm).

An electromagnetic detector array (figure 3.1a) is placed above the patient in the treatment room. For position detection, the transponders are sequentially excited with their respective resonance frequencies using source coils within the detector array. The response of the transponders following excitation is detected simultaneously in an assembly

(a) Calypso console (Image source: Calypso Medical)

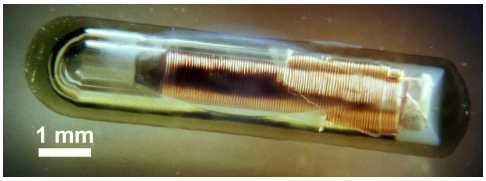

(b) Electromagnetic transponder

Figure 3.1: The Calypso System. (a) Control console with the electromagnetic detector array mounted on the arm. (b) Electromagnetic transponder with clearly visible coil of the resonance circuit.

of 32 receiver coils (Rau et al., 2008), which allows calculating transponder 3D displacement with respect to the detector array. The detector array position is determined through a room-fixed infrared camera system.

The research version of the Calypso System, which is available at our institution, provides the geometric centroid of the three actual transponder positions via Ethernet connection at a frame-rate of 25 Hz. Additionally, the rotation matrix of the actual transponder positions with respect to the reference transponder geometry is reported. A position update is based on the centroid recalculation after detection of one out of the three transponders.

The Calypso System can currently be used clinically for prostate treatments only. Using a newly developed anchored transponder design, 100% long term fixation rates of transponders implanted into canine lungs were demonstrated (Mayse et al., 2008). Recently, the United States Food and Drug Administration (FDA) granted Investigational Device Exemption (IDE) approval for clinical studies evaluating lung tumor motion monitoring during radiotherapy. Implantation of anchored transponders in human lung tumors was found to be feasible and safe (Bolliger et al., 2011).

The Calypso System motion monitoring is limited to displacements and rotations of the transponder positions. The system can however be combined with x-ray imaging (Rau et al., 2008), which could additionally allow monitoring target volume deformations or the motion of nearby organs at risk.

A disadvantage of the Calypso System is the limited compatibility with magnetic resonance imaging (MRI). Null signals surrounding the transponders with radii of ∼1.5 cm and lengths of ∼4 cm were observed within MRI imagery (Zhu et al., 2009), which may prohibit MRI-based radiotherapy treatment follow-up.

3.1.2 X-ray imaging

Kilovoltage (kV) and megavoltage (MV) x-ray image guidance is nowadays widely used for inter-fractional motion compensation (Jaffray, 2007; Verellen et al., 2008; Korreman et al., 2010). Volumetric imaging techniques include linac-integrated kV and MV cone-beam computed tomography (CBCT), MV fan-beam CT and kV in-room CT. Both CTs and CBCTs can either be acquired in conventional 3D mode, or in time-resolved respiration-correlated 4D mode (Pan et al., 2004; Sonke et al., 2005).

4D CT and 4D CBCT scans are typically obtained in 1 to 5 minutes. They represent a snapshot of intra-fractional organ motion prior to the radiotherapy treatment and are therefore not suitable for tumor tracking. Continuous x-ray based motion monitoring is accordingly limited to monoscopic 2D or stereoscopic semi-3D solutions.

Stereoscopic x-ray image guidance systems

The first system offering intra-fractional kV image guidance for respiratory gated radiotherapy treatments was the real-time radiation therapy (RTRT) system jointly developed by Mitsubishy Electronics Co. Ltd. (Tokyo, Japan) and the Hokkaido University (Shirato et al., 2000a,b). The RTRT system uses four orthogonal kV imaging systems. Dependent on the gantry angle, two of the imaging systems are selected for image acquisition and marker detection at a frame-rate of 30 Hz. The treatment beam is turned on whenever marker positions are within a predefined window around the planned coordinates.

Similar technologies are the ExacTrac (BrainLAB AG, Feldkirchen, Germany) and CyberKnife (Accuray, Sunnyvale, CA) systems. Both systems offer orthogonal stereoscopic kV x-ray imaging. Additionally, they feature external surrogate motion monitoring devices, which can be used to correlate external surrogate motion to internal target motion (section 3.2).

Linac-mounted x-ray imaging devices

Almost all modern linacs are equipped with electronic portal imaging devices (EPID). Exploiting these technologies for intra-fractional motion monitoring is therefore interesting from an economical point of view. Besides MV portal imaging, Varian Medical

Systems (Palo Alto, CA) and Elekta Oncology Systems Ltd. (Crawley, UK) offer kV imaging systems, which consist of an x-ray tube and a flat panel detector (FPD) mounted orthogonally to the treatment beam axis.

The Siemens in-line kV imaging system (Oelfke et al., 2006) will be available in the near future and is already installed at the research Siemens Artiste system at our institution. The 180° arrangement of MV treatment and kV imaging beams allows detecting tumor motion components perpendicular to the treatment beam. The target motion in this plane is particularly important for tumor tracking, as it usually features steep dose gradients. Orthogonal imaging can only partly resolve target motion perpendicular to the treatment beam. The in-line geometry is therefore beneficial for tumor tracking (Nill et al., 2005).

The use of linac-mounted x-ray imaging systems for MLC tumor tracking has been extensively investigated. MLC tracking based on a single orthogonal kV x-ray imager (Poulsen et al., 2010c,a) was performed using a correlation model, which estimated 3D target positions from 2D orthogonal x-ray projections and a 3D probability density function for the target (Poulsen et al., 2008).

MLC tracking based on MV imaging alone (Poulsen et al., 2011) as well as combined kV and MV imaging (Cho et al., 2009) was also demonstrated. MV motion monitoring is limited to high contrast objects, such as radio-opaque markers (Shirato et al., 2000b) or clearly visible lung tumors (Richter et al., 2010; Rottmann et al., 2010). Additionally, limited field of view for MV imaging can be problematic especially for IMRT treatments (Mao et al., 2008). Ma et al. (2009) demonstrated that treatment planning can be modified to guarantee marker visibility in IMRT segments without severely compromising final dose distributions.

Intra-fractional imaging in the in-line geometry

We have recently developed an intra-fraction x-ray motion monitoring system based on the in-line kV imaging concept (Fast et al., 2011a,b). The kV imaging axis was therefore intentionally tilted by 5.4° with respect to the treatment beam axis to achieve geometric separation of MV treatment and kV imaging signals on the FPD (figure 3.2).

Due to the high treatment beam intensity and the proximity of the FPD to the treatment beam source, the MV signal by far outnumbered the kV signal. We therefore synchronized every second FPD read-out with the kV imaging pulses to get subsequent frames containing mixed kV/MV and MV-only signals. Within a region of interest, these frames were subtracted to give kV-only frames.

Figure 3.3 shows an example kV-only frame. The image quality is limited by a high noise level and synchronization stripe artifacts. Nevertheless, radio-opaque marker positions

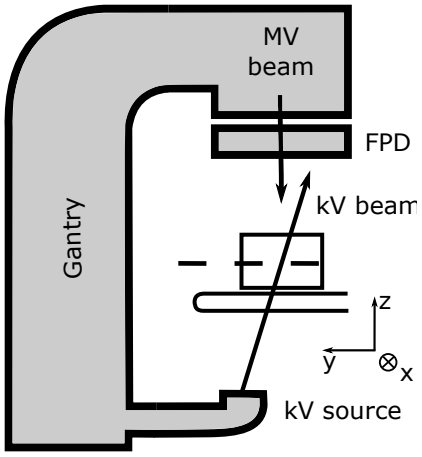

Figure 3.2: Geometry of in-line imaging system with tilted imaging axis for geometric separation of kV and MV signals. (Reprinted from Fast et al. (2011b). With permission.)

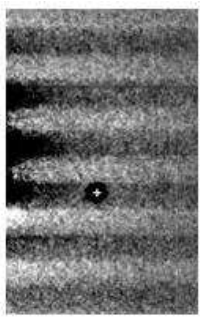

Figure 3.3: Example kV-only image. Radioopaque marker detected successfully in spite of distortions and stripe artifacts. (Reprinted from Fast et al. (2011b). With permission.)

could be detected with a latency of 87 ms and a root mean squared (RMS) detection accuracy of 0.2 mm (Fast et al., 2011b).

3.1.3 Volumetric non-ionizing soft tissue imaging

Ultrasound imaging

Ultrasound imaging has the potential to provide non-ionizing, volumetric imagery of the treatment target and nearby organs at risk for radiotherapy guidance. Propagation of ultrasound waves is, however, heavily disturbed by air and bone. Ultrasound imaging is therefore limited to organs such as the heart or organs in the pelvis and neck region (Hendee and Ritenour, 2002). The most widespread use of ultrasound imaging in radiotherapy is pre-treatment patient setup for prostate cancers. Of major concern for ultrasound based positioning is the user-to-user variability of image interpretation (Langen et al., 2003).

The following studies are encouraging for possible future application of ultrasound imaging for intra-fractional motion compensation: Hsu et al. (2005) have demonstrated the feasibility of synchronous ultrasound imaging and linac based radiation delivery. Xu and Hamilton (2006) and Harris et al. (2007) have demonstrated accurate automatic ultrasound organ motion tracking based on 2D and 3D imagery, respectively. 3D tracking was however not performed online due to large computation times. Schlosser et al. (2010)

have developed a robotic ultrasound probe manipulator to remotely acquire ultrasound imagery during radiotherapy treatments.

Magnetic resonance imaging

Magnetic resonance imaging (MRI) provides volumetric imagery with excellent soft-tissue contrast and without delivering dose of ionizing radiation. The integration of MRI with medical linacs for intra-fractional motion management has become a strong field of research. Prototype integrated systems have been proposed: A group from the University of Utrecht, The Netherlands, has integrated a 1.5 T MRI scanner with a medical linac, (Raaymakers et al., 2004; Lagendijk et al., 2008). A group from the University of Alberta, Edmonton, Canada, have built a prototype system with a 0.2 T MRI scanner (Fallone et al., 2007, 2009). A third group – ViewRay Inc., Cleveland, OH and the University of Florida, Gainsville, FL – has integrated a low-field MRI scanner with three ^{60}Co sources (Dempsey et al., 2005).

Major challenges for the development of such integrated systems are distortions of the beam generation through the strong static magnetic field and MR image quality distortions through radiofrequency inferences. Nevertheless, simultaneous MV radiation delivery and MR imaging has been demonstrated successfully (Fallone et al., 2009). Additionally, influences of the magnetic field on the radiation dose deposition have to be taken into account for treatment planning (Raaijmakers et al., 2005; Kirkby et al., 2008; Pfaffenberger and Oelfke, 2011).

Recently, real-time tracking of lung tumors within MR imagery has been demonstrated (Cerviño et al., 2011). However, such tracking systems are restricted to 2D imagery because of long acquisition times for volumetric MR images as well as long computation times for tracking algorithms within 3D imagery.

3.2 External surrogate monitoring and correlation models

Using the aforementioned internal motion monitoring devices alone is not ideal for real-time tumor tracking. Continuous internal tumor motion monitoring based on kV x-ray imaging leads to considerable imaging doses. Detection of implanted markers requires a patient dose of approximately 0.18 mGy per image (Shirato et al., 2000b). Combining continuous external motion monitoring with occasional x-ray imaging has the potential to substantially reduce imaging dose while maintaining a high level of internal motion detection accuracy. Volumetric image acquisition times for both ultrasound and MR as

well as tumor position detection within the volumetric images can lead to large motion monitoring latencies and low sampling rates. The combination of external motion monitoring with ultrasound or MR imaging could counteract this effect. In the following, we introduce several external surrogate motion technologies and discuss the mathematics for combined external-internal motion monitoring strategies.

3.2.1 External surrogate monitoring technologies

Various technologies for external surrogate monitoring have been proposed. The most extensively used device is the real-time position management (RPM) system (Varian Medical Systems Inc., Palo Alto, CA) developed by Kubo et al. (2000). The system uses an infrared marker block, which is placed on the patient's chest or abdomen. The markers are detected with an infrared camera system. The vertical coordinate of detected marker displacements is reported as surrogate motion signal.

Spirometry measures the volume of inhaled and exhaled air through a mouthpiece. An additional noseclip prevents breathing through the nose. Hoisak et al. (2004) showed that tidal lung volume changes correlate better to tumor motion than abdominal displacement. Baseline drifts, which are often observed with spirometry (Zhang et al., 2003), are however concerning for real-time tumor tracking.

Anzai Medical Co. Ltd. (Tokyo, Japan) offers two external motion monitoring systems. A pressure belt system detects the respiration-induced expansion of an elastic belt around the patient's chest or abdomen. Alternatively, vertical abdominal surface motion can be measured with a laser system. The Anzai system provides an interface for respiratory gated radiotherapy treatments using Siemens linacs (Li et al., 2006).

Patient surface motion monitoring is provided by VisionRT Ltd. (London, UK). The system projects a speckle pattern on the patient surface. Individual points in the speckle pattern are detected with a stereoscopic camera system, which allows 3D surface mapping through triangulation (Bert et al., 2005). AlignRT is used for accurate pre-treatment patient positioning (Schöffel et al., 2007). Actually measured patient surfaces are registered with a reference surface using full translational and rotational degrees of freedom. GateCT and GateRT produce 1D signals for respiratory gated CT or respiratory gated radiotherapy by registering surfaces with only one translational degree of freedom.

3.2.2 Correlation of external surrogate and internal tumor motion

Various studies have retrospectively analyzed the correlation between external surrogate and internal organ motion (Vedam et al., 2003; Ahn et al., 2004; Hoisak et al., 2004;

Tsunashima et al., 2004; Gierga et al., 2005). They used different external motion surrogates and x-ray fluoroscopy for either marker-based internal tumor motion monitoring or internal surrogate (such as diaphragm) motion monitoring. The quality of correlation was thereby quantified using Pearson's sample correlation coefficient

$$R = \frac{\sum(X_i - \bar{X})(Y_i - \bar{Y})}{\sqrt{\sum (X_i - \bar{X})^2}\sqrt{\sum (Y_i - \bar{Y})^2}} \,, \tag{3.1}$$

where the pairs (X_j, Y_j) represent synchronous external and 1D internal position observations and $(\bar{X}, \bar{Y})$ the corresponding sample means. The correlation coefficient can be interpreted as quality indicator of a straight line fit to $\{\, (X_i, Y_i) \mid i \in [1, N] \,\}$, N being the total number of observations. Additionally, phase-shifts between external and internal motion were quantified by shifting the time axes of internal and external observations such that the correlation coefficient was maximized (Hoisak et al., 2004; Tsunashima et al., 2004; Korreman et al., 2006; Ionascu et al., 2007). Phase-shifts of more than 0.5 s were frequently observed. The external/internal correlation was found to be more pronounced in superior-inferior (SI) direction than in anterior-posterior (AP) direction (Ionascu et al., 2007).

Figure 3.4 shows an example correlation analysis. The external/internal data displayed in (a) and (b) was normalized to zero mean and unity variance. The internal AP motion is lagging behind the external surrogate. Deviations of the straight line fit from the breathing data are therefore larger in AP than in SI direction, which is reflected by a smaller correlation coefficient.

The generally strong correlation between external surrogate and internal organ motion justifies the use of external surrogate monitoring for intra-fractional motion compensation. Commercially available respiratory gating systems often rely implicitly on a fixed external/internal correlation (Korreman et al., 2008). For amplitude-based gating, the treatment beam is turned on whenever the external signal enters a predefined gating window. For phase-based gating, the actual breathing phase is estimated from the surrogate signal and the beam is turned on whenever the actual breathing phase falls into a predefined window – most commonly centered around peak exhale. Berbeco et al. (2005) have shown that neither modality is significantly superior in terms of residual internal tumor motion.

Of major concern are inter-fractional shifts in the baseline of internal tumor breathing traces. Sonke et al. (2008) have reported systematic and random baseline variations of 3.9 mm and 2.4 mm in SI-direction, respectively. Based on this data, Korreman et al. (2008) showed that margins can be safely reduced only if daily image guidance is used to account for baseline shifts. Intra-fractional changes in external/internal correlation were also observed (Ionascu et al., 2007). Intra-fractional correlation model updates can substantially reduce internal motion prediction errors (Hoogeman et al., 2009).

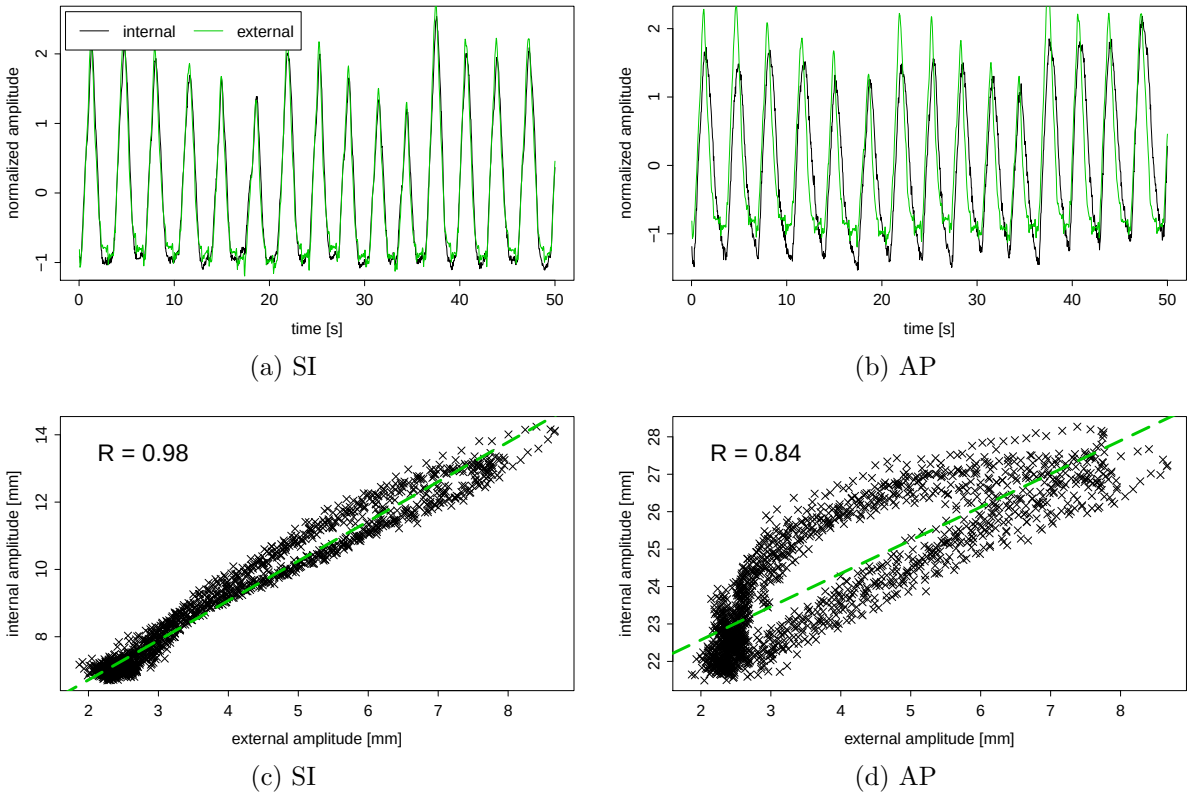

(a) SI (b) AP

(c) SI (d) AP

Figure 3.4: Example synchronous external surrogate and internal tumor motion data in SI and AP directions (upper row). Scatterplot of external/internal data points together with a straight line fit and Pearson's correlation coefficient R (lower row).

The simplest and most common external/internal correlation model is a straight line or linear fit. Correlation models based on linear fitting can however not accurately predict hysteretic breathing traces (figure 3.4d), which are typical for lung tumor movements (Keall et al., 2006b). Two ways to account for hysteresis have been proposed: Firstly, separating the breathing trajectory into inhale and exhale phases and then constructing a phase-dependent non-linear map through polynomial fitting (Seppenwoolde et al., 2007). Secondly, the method of state-augmentation (Ruan et al., 2008), which uses not a single external surrogate position as input for the correlation model, but provides the correlation model with an input vector of at least two past surrogate position observations.

Ruan et al. (2008) compared prediction accuracies of correlation models based on linear fitting (LF), polynomial fitting (PF) and state-augmented linear regression (LR). The LR correlation model clearly outperformed PF and LF. Ernst et al. (2011) showed superior prediction accuracy of a state-augmented support vector regression (SVR) correlation model compared to PF.

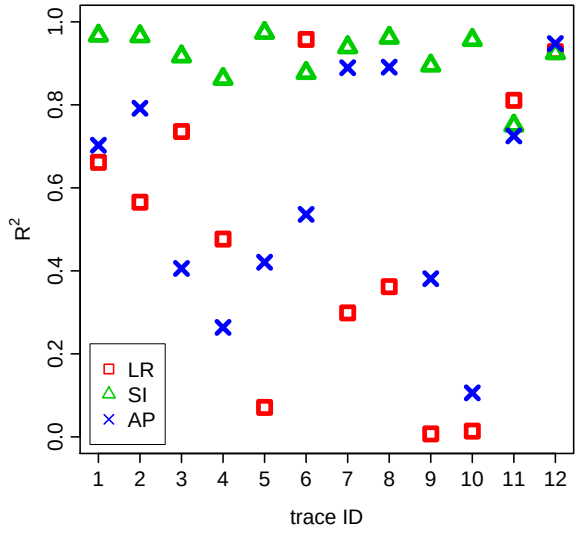

Figure 3.5: Squared Pearson's correlation coefficients R^2 for the 12 synchronous external surrogate and internal tumor motion data sets for left-right (LR), superior-inferior (SI) and anterior-posterior (AP) directions.

3.3 Comparison of correlation models

To guide our choice of a suitable correlation model for MLC tracking based on x-ray imagery combined with external motion monitoring (section 6.2), we have compared LF, augmented LR and augmented SVR correlation models. Similar to the performance comparison of respiratory motion forward prediction as outlined in chapter 2, we have evaluated two different intra-fractional correlation model update schemes and have applied model parameter tuning routines.

3.3.1 Materials and methods

Patient breathing data The comparison of correlation models was based on the same twelve breathing data samples that were used for the comparison of the previously described prediction models (section 2.2.1). The data sets were recorded with the Mitsubishi RTRT system and consist of synchronous internal 3D tumor position and 1D abdominal motion measurements acquired at a frame-rate of 30 Hz. Figure 3.5 displays Pearson's correlation coefficients of the 12 synchronous external/internal breathing data samples. The linear correlation is strongly pronounced between external and internal SI motion and relatively poor for LR an AP directions.

Data preparation The breathing data sets were expressed as uniformly sampled time-series

$$\left\{ \boldsymbol{s_i} := \boldsymbol{s}(t_i) = \left(s_{ext}(t_i),\, s^1_{int}(t_i),\, s^2_{int}(t_i),\, s^3_{int}(t_i) \right)^T \mid i \in [1, N] \right\} , \tag{3.2}$$

where $s_{ext}(t_j)$ and $s^k_{int}(t_j)$ represent the 1D external surrogate position observation and coordinate k of the internal positon observation at point in time t_j. N is the total number of observations. The breathing samples were split up into a 20 s training data set and a 50 s testing data set. Correlation model training can be performed quickly. We therefore reserved only 0.5 s of computation time between the training and testing data sets.

For each euclidean coordinate k of the internal motion data, we constructed pairs of input vectors and target scalars $\left(\boldsymbol{x}_j, y^k_j\right)$ from the breathing data samples. Target scalars were given by internal tumor positions $y^k_j = s^k_{int}(t_j)$. To simulate sparse internal motion monitoring, only a small subset of internal positions observations was included into the training data set:

$$\left\{ \left(\boldsymbol{x}_i, y^k_i\right) \mid i \in \{\, 1, \delta_{int}, 2\delta_{int}, ..., N_{tr} \,\} ,\ k \in [1, 3] \right\} . \tag{3.3}$$

The spacing between training data instances was set to $\delta_{int} = 15$ corresponding to 0.5 s.

The p-dimensional input vectors for point in time t_j were constructed from the history of past external surrogate positions:

$$\boldsymbol{x}_j \;=\; \left(s_{ext}(t_{(j-\delta(p-1))}) ,\, s_{ext}(t_{(j-\delta(p-2))}) ,\, \ldots ,\, s_{ext}(t_j) \right)^T , \tag{3.4}$$

using the lag length $\delta \in \mathbb{N}$ of successive input vector entries. For the linear fit correlation model, only 1D input vectors (*i.e.*, $p = 1$) were used.

Preprocessing Preprocessing as depicted in section 2.2.2 could not be applied for the correlation models. It is based on scaling factors for the input vectors and target scalars, which are calculated from a sliding window of past internal motion observations. Consequently, the preprocessing procedure relies on continuous internal motion measurements, which interferes with the actual goal of combined external/internal motion monitoring strategies – namely accurate tumor tracking in spite of sparse internal motion measurements.

Correlation models The actual prediction of internal tumor positions from external surrogate data was performed using the previously outlined mathematical procedures (section 2.2.3). The LF and augmented LR correlation models used equation (2.8) for internal motion prediction. The offset term β_0 was however not set to zero, but was optimized together with the coefficient vector $\boldsymbol{\beta}$. The prediction procedure for the augmented SVR correlation model followed the formalism outlined in section 2.2.3.

Training schemes Besides the stationary correlation model training, we investigated two modes of intra-fractional correlation model updates. The update schemes are tailored to the MLC tracking mode based on combined external/internal motion monitoring depicted in section 6.2: During the delivery of step-and-shoot IMRT, five kV x-ray images are acquired between the delivery of the beam segments with an update-rate of 2 Hz. Accordingly, the correlation model training schemes are:

1. *Stationary:* The correlation model is trained once using the 40 internal tumor position observations within the training data set.

2. *Adaptive:* The correlation model is retrained every 10 s using 5 newly acquired internal positions plus the latest 35 positions of the previous training cycle.

3. *Adaptive-expansive:* The correlation model is retrained every 10 s using 5 newly acquired internal positions plus all of the previously acquired positions.

Model parameter tuning The augmented LR and SVR correlation models feature the model parameters listed in table 2.2. Model parameter tuning was performed as outlined in section 2.2.5. Computation times were however much shorter because our investigations did not include different latencies, sampling rates or 3D data processing modes. We also optimized patient-independent model parameter sets and used them for the actual correlation model comparisons.

Prediction accuracy measures Correlation model prediction accuracy was quantified using 3D RMS deviations between predicted and actually measured internal positions observations within the testing data set. The gain in prediction accuracy compared to using no prediction was expressed as normalized prediction error according to equation (2.21). Using no correlation model prediction refers to setting the prediction value as the mean internal tumor position within the testing data set.

3.3.2 Results

Figure 3.6 shows the comparative performance of the three correlation models for the 12 breathing traces using adaptive-expansive training and patient-independent model parameters. Prediction method 'none' refers to using the mean value of the internal tumor positions of the training data set as correlation model prediction. All correlation models reduce prediction errors substantially, but the correlation model accuracy depends strongly on the specific breathing trace. In almost all cases, the augmented correlation models clearly outperform the LF.

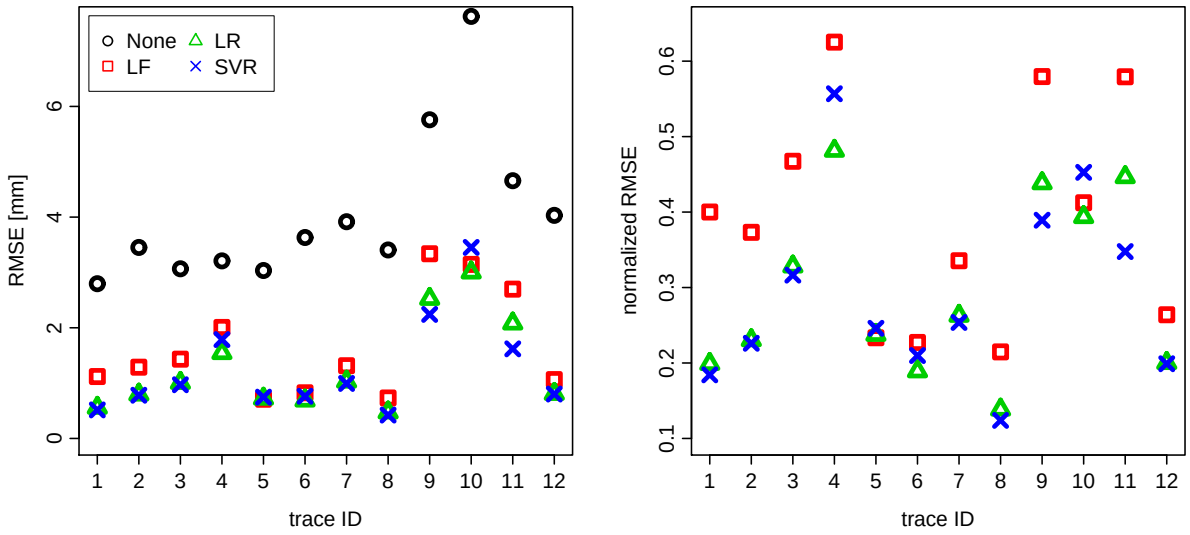

Figure 3.6: Comparison of correlation model prediction errors for individual breathing traces using adaptive-expansive training. Absolute errors (left) and errors normalized to using no prediction (right).

Figure 3.7 shows example correlation model predictions for breathing traces 1 and 10 using adaptive-expansive training. The SI-coordinate of trace 1 is almost perfectly predicted by all three correlation models. The LF prediction of the AP-coordinate is much worse than the LR and SVR predictions. The actual AP-motion is lagging behind the LF prediction. This phase shift can be effectively compensated by the LR and SVR correlation models based on state augmentation.

Breathing trace 10 is the only example which shows superior prediction performance of the LR correlation model. Obviously, all considered correlation models fail to predict the AP motion accurately. This is not surprising, as the correlation coefficient between external motion and internal AP motion of trace 10 is smaller than 0.2 (figure 3.5). The LF correlation model predicts the SI-coordinate better than LR and SVR. The models based on state augmentation can not predict the strong baseline drifts and amplitude fluctuations accurately.

Table 3.1 lists 3D correlation model prediction accuracies averaged over the 12 breathing traces for patient-independent model parameters. The augmented SVR outperforms the augmented LR slightly. LF correlation model predictions are substantially less accurate. The adaptive retraining schemes can slightly improve prediction accuracies. The only exception is adaptive training for the LF correlation model, which yields worse results than stationary training. When averaged over the three training modes, the improvements in absolute correlation model prediction accuracy of SVR and LR compared to LF are 23% and 21%, respectively.

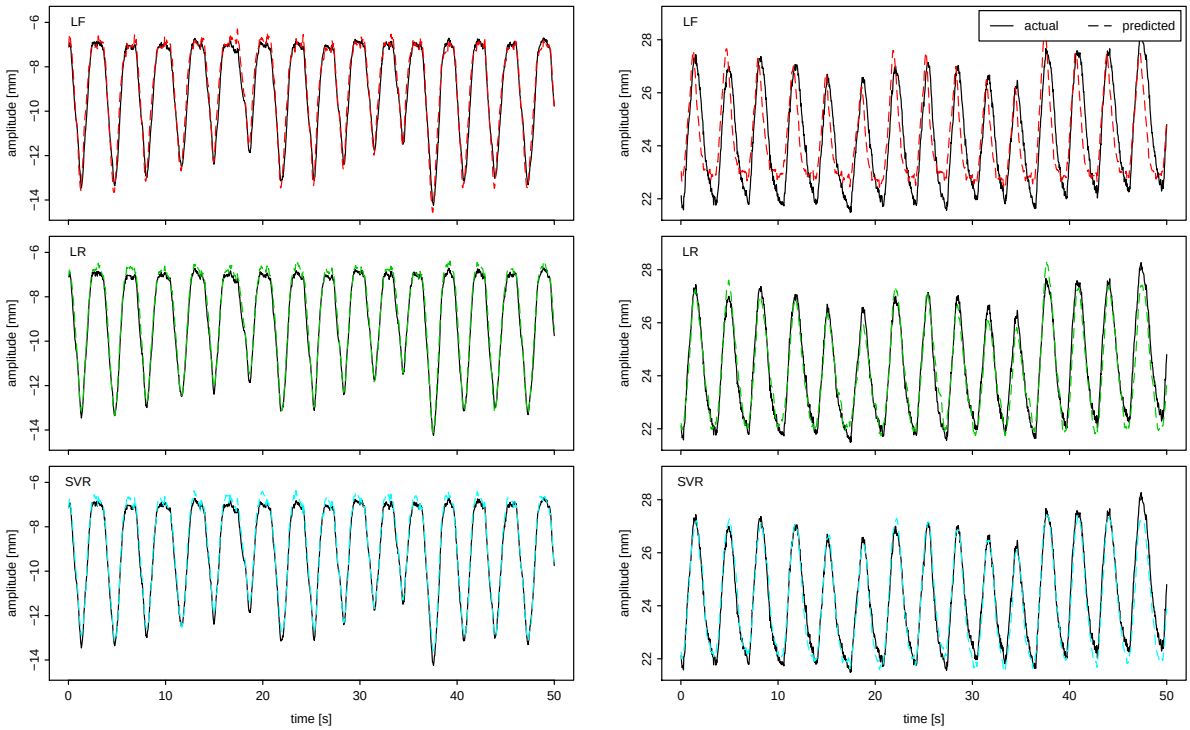

(a) Breathing trace 1, SI

(b) Breathing trace 1, AP

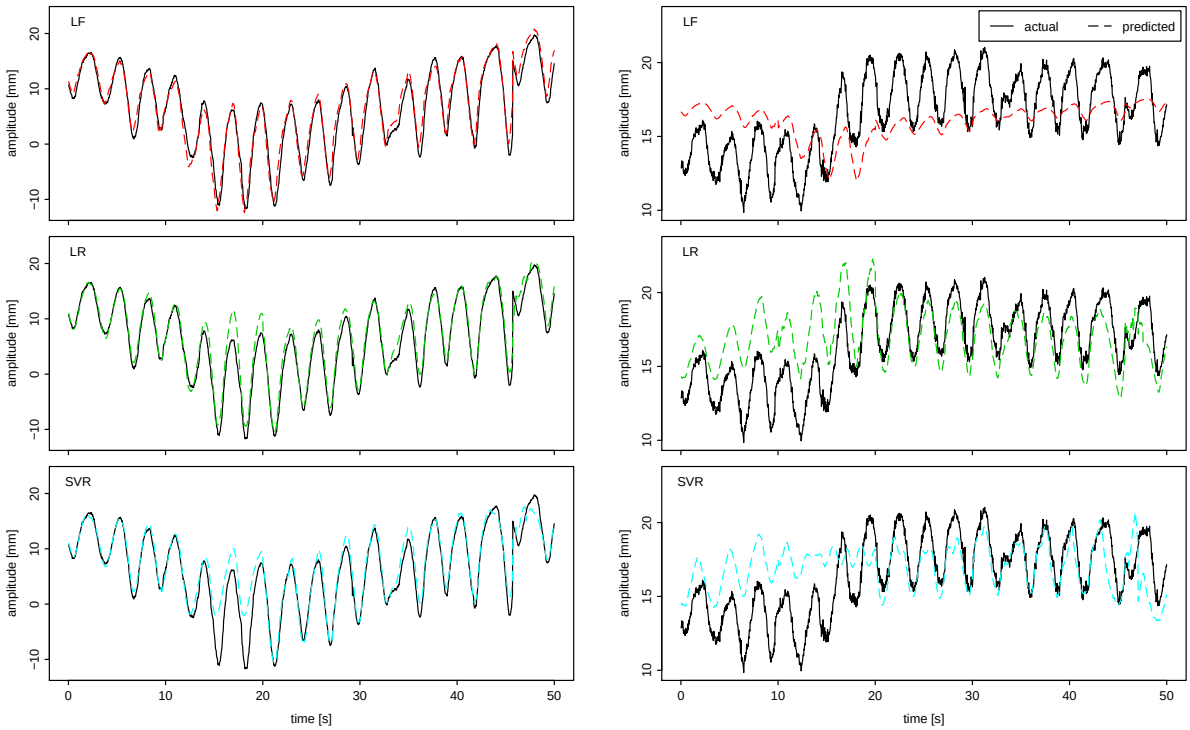

(c) Breathing trace 10, SI

(d) Breathing trace 10, AP

Figure 3.7: Actual breathing signal in superior-inferior (SI) and anterior-posterior (AP) direction and corresponding correlation model predictions for breathing traces 1 and 10.

Table 3.1: 3D root mean squared prediction errors of the correlation models for stationary (1), adaptive (2) and adaptive-expansive (3) training.

	RMSE [mm]			normalized RMSE		
	training scheme			training scheme		
Correlation model	(1)	(2)	(3)	(1)	(2)	(3)
LF	1.69	1.71	1.64	0.42	0.42	0.40
LR	1.41	1.31	1.27	0.35	0.32	0.31
SVR	1.32	1.29	1.26	0.33	0.32	0.31

Table 3.2: Root mean squared prediction errors of the correlation models. 3D prediction errors and errors of left-right (LR), superior-inferior (SI), anterior-posterior (AP) directions for adaptive-expansive training.

	RMSE [mm]				normalized RMSE			
Correlation model	LR	SI	AP	3D	LR	SI	AP	3D
LF	0.52	1.02	1.06	1.64	0.58	0.31	0.66	0.40
LR	0.45	0.80	0.79	1.27	0.50	0.25	0.49	0.31
SVR	0.46	0.79	0.78	1.26	0.51	0.24	0.49	0.31

Table 3.2 displays correlation model prediction accuracies for LR, SI and AP directions using adaptive-expansive training. The absolute prediction errors are almost equal for SI and AP directions. For LR direction, the absolute prediction errors of SI and AP directions are roughly halved. Because of the different average amplitudes of the three coordinates, the normalized prediction errors in SI direction are roughly twice as small as for AP and LR directions. The correlation models accordingly predict SI motion much more accurate than LR and AP motion. Beholding the poor linear correlation between between external motion and internal AP and LR direction as displayed in figure 3.5, this result is not surprising.

3.3.3 Discussion

We have compared the predictive performance of three correlation models. Two models – LR and SVR – were based on the method of state-augmentation, which provides the correlation models with a input vector of previously observed external motion observations. The LF correlation model, in contrast, predicts internal motion from a single external motion observation.

Similar to the analysis of respiratory motion forward prediction (section 2.3), we observed

only small improvements of the adaptive correlation model retraining schemes. The adaptive retraining schemes were tailored to a step-and-shoot IMRT delivery, which updates the correlation model with 5 internal tumor position observations in between the delivery of the individual beam segments. The additional information content is relatively small compared to the initially acquired 40 position observations and induces therefore only minor correlation model adaptions.

As expected, the models based on state-augmentation clearly outperformed the LF correlation model. The SVR performed slightly better than the LR correlation model. The largest LR and SVR correlation model prediction errors were observed for breathing trace 10, which exhibits large baseline drifts and amplitude fluctuations. In this case, LR and SVR even performed worse than the LF correlation model. For forward prediction of respiratory motion, we have applied preprocessing routines to minimize baseline drifts and amplitude fluctuations. The sparse internal motion data available to the correlation models, however, prohibits such preprocessing.

4 Tracking system integration

In this chapter, we present the hardware and software intergration of our MLC tracking system. Section 4.1 introduces the hardware components of the tracking system (*i.e.,* the medical linear accelerator and the multileaf collimator) as well as interfaces to the hardware components through which we adapt the radiotherapy delivery process to the real-time monitored target motion. In section 4.2, we describe general strategies for motion adaptive MLC leaf positioning. In section 4.3, we introduce the workflow of our integrated MLC tracking control system. Section 4.4 gives a conceptual overview of our MLC tracking software implementation.

4.1 Radiotherapy delivery system

The most widespread technique to produce treatment beams in radiotherapy is the medical x-ray producing electron linear accelerator (linac). An electron beam impinges onto a high density target to produce photons at energies in the MeV range. The photon beam is spatially limited with a primary collimator. A uniform fluence is produced through a subsequent flattening filter. The shape of the actual treatment beam is adjusted by a secondary collimator; most commonly a computer-controlled multileaf collimator (MLC). A MLC consists of an arrangement of metal plates (leaves) mounted on opposing leaf carriages. The positions of the leaves can be controlled individually. The leaves block the beam partially such that the remaining aperture defines the treatment field. The entire accelerator is mounted on a gantry that can rotate around the patient.

A medical linac equipped with a MLC supports the following radiotherapy delivery modes:

1. *Conformal RT:* Radiation dose is delivered from multiple gantry angles. The beam shape is adjusted to enclose the beam's eye view of the 3D contour of the target volume.

2. *Step-and-shoot IMRT:* The fluence profile from every beam angle is modulated to achieve better dose homogeneity in the target and better dose sparing of healthy tissues. For step-and-shoot IMRT, the fluence modulation is performed by delivering the dose of each gantry angle in several segments with different MLC shapes.

3. *Dynamic IMRT:* The leaves move continuously on individual trajectories while the radiation beam is turned on. Fluence modulation along the path of a leaf pair is achieved through different leaf opening times and correspondingly different radiation exposure times at each tissue position.

4. *Rotational IMRT:* Both the gantry and the leaves move continuously during radiation delivery. Additionally, the dose-rate of the linac is often modulated as a function of the actual gantry rotation angle. Rotational IMRT can be performed with a single or with multiple arcs.

For conformal RT and step-and-shoot IMRT, radiation delivery is interrupted while the MLC leaves are moving. Continuous leaf motion during radiation delivery for dynamic and rotational IMRT requires dynamic MLC control. Such dynamic MLCs have to control not only precise leaf positioning but also precise leaf dynamics, *i.e.* leaf velocities and accelerations.

4.1.1 The Siemens ARTISTE linear accelerator

The Siemens ARTISTE is the most recent radiotherapy suite offered by Siemens Healthcare (Erlangen, Germany). Figure 4.1 shows the research ARTISTE linac, which is installed at our institution for experimental purposes. The ARTISTE features several on-board imaging capabilities:

1. *MVision:* MVision provides megavoltage (MV) cone-beam computed tomography (CT). The system uses the treatment beam for imaging. Image acquisition is based on the amorphous silicon flat panel detector (1024 $\times$ 1024 pixels, 0.4 mm $\times$ 0.4 mm pixel size) displayed in figure 4.1a.

2. *KView:* KView uses a modified treatment beam for imaging. The electron target in the linac head is replaced and the flattening filter is removed to produce a softer photon energy spectrum. The system yields considerable image quality improvements compared to MVision (Faddegon et al., 2008; Steinke, 2010).

3. *KVision:* KVision denotes the on-board kV x-ray imaging solution of the ARTISTE linac using the in-line geometry (Oelfke et al., 2006). The x-ray source is mounted at an angle of 180° with respect to the treatment beam (figure 4.1b) so that the imaging axis is parallel to the treatment beam axis. Superior imaging quality compared to MVision (Stützel et al., 2008) and KView (Steinke, 2010) was demonstrated.

KVision is not a commercially available product yet. Siemens however offers the in-room kV imaging system CTVision. A complete CT scanner is mounted on rails so that it

(a) (b)

Figure 4.1: The research Siemens ARTISTE linear accelerator at the DKFZ. (a) The MV flat panel detector for MVision and KView imaging. (b) The x-ray tube and kV flat panel detector for in-line KVision imaging.

can slide over the patient lying on the radiotherapy treatment couch. The system provides excellent image quality. Couch shifts into treatment position after CT acquisition however increase patient setup times.

4.1.2 The Siemens 160 MLC

The ARTISTE linac is equipped with a Siemens 160 MLC. The photograph in figure 4.2 shows the 160 leaves, whose extensions from the two carriages can be controlled individually. Carriage positions are also computer-controlled. The leaf width amounts to 5 mm in the isocenter plane. The leaves can be extended from the carriages by 20 cm. The maximum field size is $40 \times 40\,\mathrm{cm}^2$. The maximum leaf travel speed is 43 mm/s. The longitudinal penumbra is 5 mm and the leakage through leaf tips is 13.5% on the central axis. A more comprehensive characterization of the 160 MLC is given in Tacke et al. (2008).

The Siemens 160 MLC is not designed for dynamic radiotherapy delivery modes. The ARTISTE radiotherapy suite therefore supports conformal RT and step-and-shoot IMRT deliveries only. A solution similar to rotational IMRT called 'mARC' will be available soon. Hereby, radiation is delivered in multiple beamlets with a continuously moving

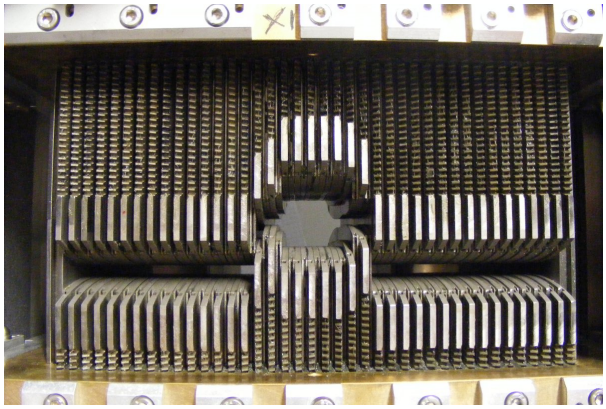

Figure 4.2: Photograph of the Siemens 160 MLC. The 80 leaves on each carriage can be positioned individually to form the desired field shape.

gantry but static leaves. MLC shapes are adjusted during beam interruptions between the beamlets (Salter et al., 2011).

4.1.3 Hardware interfaces

MLC tracking represents a major modification of the radiotherapy delivery process. Our research ARTISTE radiotherapy suite was therefore endowed with several hardware interfaces, which allow us to both monitor and modify parts of the radiation delivery process.

Linac interfaces

The MLC tracking deliveries require control of the treatment beam status. For example, the treatment beam has to be turned off while the MLC prepares new segments of a step-and-shoot IMRT delivery, during predictor training or if tracking errors occur. The ARTISTE linac provides an interface for respiratory gated radiotherapy deliveries. We utilize the gating interface to control the treatment beam during the MLC tracking deliveries.

Two further interfaces to the ARTISTE linac were established for rotational IMRT deliveries: A gantry interface continuously monitors and reports actual gantry angles. A dose-rate control board performs gantry angle dependent dose-rate modulation (Ulrich, 2009).

MLC interface

The 160 MLC can be operated with a modified Siemens Collimator Control (SCC) unit, which allows us to move leaves while the treatment beam is turned on (Tacke, 2009). The modified SCC can receive requests for next leaf positions through Ethernet connection and report actual leaf positions at the same time. Such position commands include positions and velocities for both the carriages and the 160 leaves.

The SCC performs the actual hardware control for leaf positioning. It collects several position packages and then sends the leaves on a trajectory that closely resembles the requested trajectory. If the SCC receives several identical position packages, it slowly decelerates the leaf motion to reach the desired position without overshoot. For a series of different, possibly noisy position requests, the SCC actuates leaf trajectories that smoothly follow the desired trajectories with a relatively large latency of $\tau_{mlc} \approx 0.5\,\mathrm{s}$ (see section 5.1 for a detailed discussion of latency measurements).

4.2 Motion-adaptive leaf positioning

The rationale of MLC tracking is to adapt the treatment beam instantaneously to intra-fractional organ motion by repositioning of the leaves of a dynamic MLC. In section 4.2.1, our leaf positioning strategy for the relatively simple case of rigid target volume translations will be introduced. Realistic intra-fraction organ motion is more complex and may involve rotations, deformations or relative organ displacements. A meaningful compensation of such complex forms of organ motion is challenging. We will discuss the main problems and previously proposed approaches associated with MLC tracking of complex organ motion in section 4.2.2.

4.2.1 Rigid 3D translations

Rigid 3D translation refers to a simplistic model of organ motion: the entire target volume as well as all nearby organs move synchronously into the same direction. Under this assumption, perfect motion compensation can be achieved in three steps: Firstly, transformation of the organ motion into coordinates parallel and perpendicular to the beam axis. Secondly, translation of the treatment field in synchrony with the beam's eye view of the organ motion (*i.e.,* the organ motion in the plane perpendicular to the beam axis). Thirdly, magnification of the treatment field according to the motion parallel to the beam axis because of the cone-shaped treatment beam. For realistic respiratory

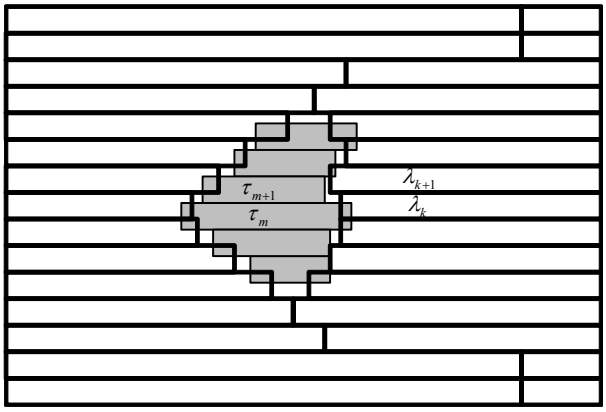

Figure 4.3: Leaf position definition for 3D target translation. The initially planned MLC field shape (gray) is shifted perpendicular to the leaf travel direction. The leaves are positioned such that underdosage equals overdosage area.

motion patterns, the magnification step represents a small correction. Given a source-to-isocenter distance of 100 cm and a motion range of ±10 mm, the magnification amounts to 1%. We therefore neglect magnification in our leaf positioning algorithms.

Due to the finite leaf width, MLC tracking can only approximate this compensation strategy. Figure 4.3 illustrates the problem of motion compensation perpendicular to the leaf travel direction. The leaves are positioned to approximate the desired field shape. Parts of the desired field shape will be blocked (underdosage). Parts outside the desired field are irradiated (overdosage). Our leaf positioning algorithm weights underdosage and overdosage areas equally and therefore optimizes the conformity with the desired field shape while maintaining the integral fluence.

Optimal leaf positions according to the above definition can be calculated as follows: Let $y(\lambda_k)$ and $x(\lambda_k)$ denote the lower edge and the tip of leaf λ_k. Accordingly let $y(\tau_m)$ and $x(\tau_m)$ denote the lower and right edges of target segment τ_m. If leaf λ_k overlaps the target segments τ_m and τ_{m+1}, the optimized leaf position $x(\lambda_k)$ is given as weighted sum over target segment edges $x(\tau_m)$ and $x(\tau_{m+1})$:

$$x(\lambda_k) \;=\; \frac{y(\tau_{m+1}) - y(\lambda_k)}{y(\lambda_{k+1}) - y(\lambda_k)}\, x(\tau_m) \;+\; \frac{y(\lambda_{k+1}) - y(\tau_{m+1})}{y(\lambda_{k+1}) - y(\lambda_k)}\, x(\tau_{m+1})\;. \tag{4.1}$$

Figure 4.3 shows the positions of closed leaf pairs adjacent to the aperture. The first closed leaf pair beside the open field is placed in the middle of the positions of the adjacent open leaf pair to be able to open quickly in case of rapid organ motion perpendicular to the leaf travel direction. The other closed leaf pairs are retracted by 1 cm and 5 cm to minimize the leakage through leaf tips, which is largest on the central axis.

4.2.2 Complex forms of organ motion

Besides rigid translation of the entire patient anatomy, a realistic description of intra-fractional motion has to include:

- non-uniform translation of adjacent organs with different magnitudes or even different directions for individual organs,
- rotation of individual organs or of the initial arrangement of adjacent organs,
- non-uniform deformation of individual organs.

With today's internal motion monitoring technologies (as reviewed in section 3.1), complex organ motion can not be fully detected. In the majority of cases, motion monitoring is limited to translations of markers, which are implanted into or close to the target volume. Relative motion of markers can however give rise to organ rotation as well as uniform organ deformation. Volumetric imaging technologies could in principle detect more complex organ motion. Image acquisition times as well as processing times for automatic segmentation of multiple organs however restrict such monitoring strategies.

Nevertheless, the adaptation of dynamic IMRT deliveries to target volumes translating and deforming uniformly in 1D has been discussed theoretically (Papiez and Rangaraj, 2005; Papiez et al., 2005; Tacke et al., 2007). These considerations did not include tissue density changes due to deformation, which may influence the dose deposition.

Compensation of target translation and rotation through MLC tracking has been demonstrated experimentally (Wu et al., 2011). Motion monitoring was based on the Calypso System (see section 3.1.1). The study was restricted to rigid target rotations in beam's eye view. Rotations out of the beam's eye view plane can not be compensated by leaf repositioning alone, but would additionally require gantry and patient table rotations.

Suh et al. (2009) have proposed a 4D planning and 4D delivery approach, which implicitly takes complex organ motion into account. Different treatment plans are generated for each phase of a 4D planning CT. During 4D delivery, the actual breathing phase is detected and the MLC field for this particular phase of the 4D treatment plan is selected and adapted in real-time. If the simultaneously monitored tumor position deviates from the tumor position within the corresponding phase in the planning CT, the MLC aperture is adapted as described in section 4.2.1. 4D planning hereby has to assure, that the 4D delivery is feasible given the MLC hardware constraints such as maximum leaf velocities.

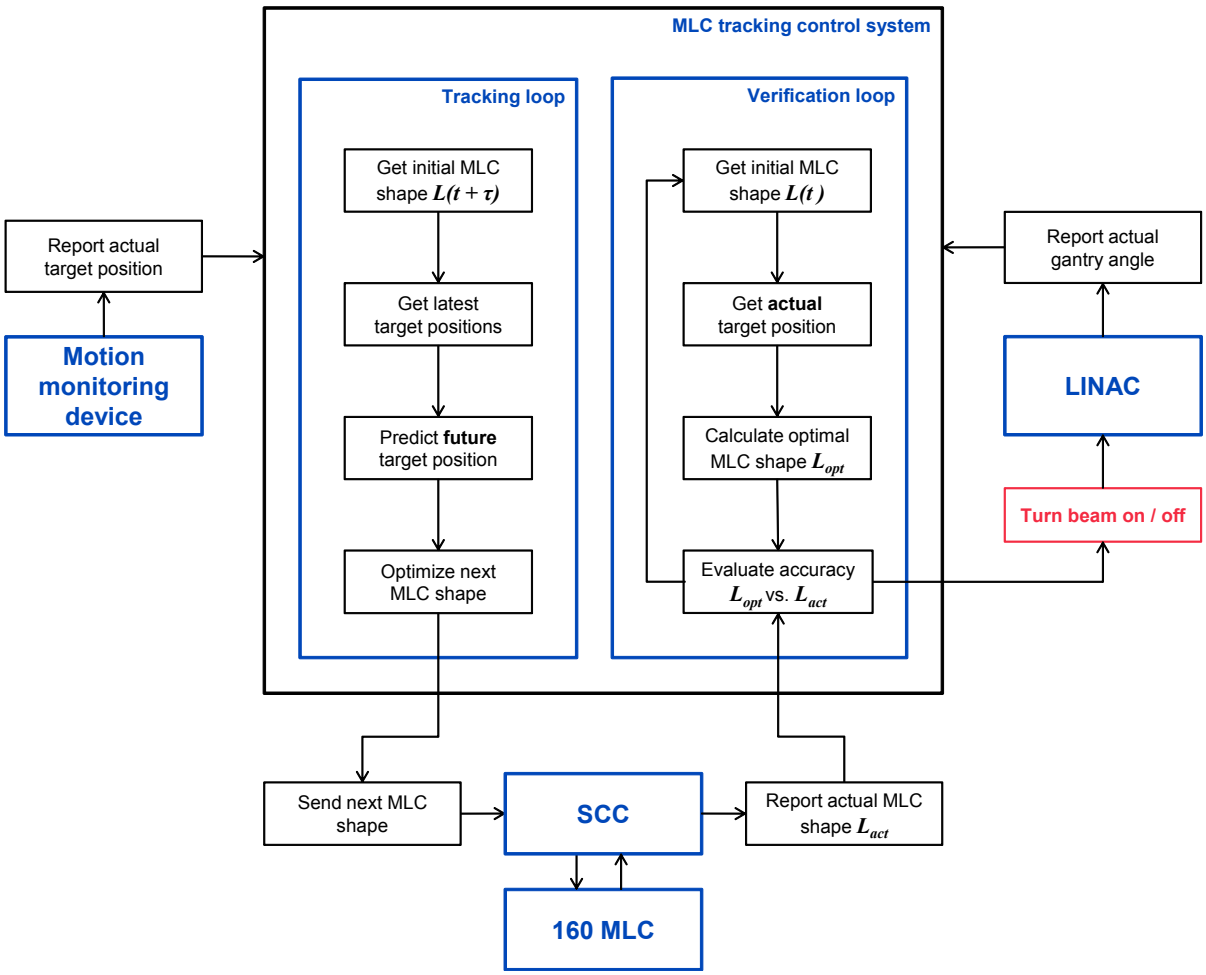

Figure 4.4: Overview of the MLC tracking platform installed at DKFZ.

4.3 MLC tracking workflow

We have implemented a MLC tracking platform based on the research Siemens ARTISTE radiotherapy suite installed at our institution (section 4.1). For this purpose, we have developed a MLC tracking control system (MTCS), which uses the hardware interfaces described in section 4.1.3 to adapt the aperture of the Siemens 160 MLC to continuously monitored target motion. The system supports the application of MLC tracking to conformal RT, step-and-shoot IMRT, dynamic IMRT and rotational IMRT deliveries. MLC tracking is restricted to the compensation of rigid 3D target translations (section 4.2.1).

Figure 4.4 gives an overview of the MLC tracking platform. The MTCS imports the leaf sequence $\boldsymbol{L}(MU)$, which is defined in the treatment plan of the radiotherapy delivery (section 4.3.1). During the MLC tracking delivery, the MTCS continuously receives current target positions from the motion monitoring device and actual MLC shapes from the SCC. For rotational IMRT deliveries, the linac reports actual gantry angles. Based on

the real-time input data, the MTCS adapts the radiotherapy delivery to the current target motion and controls the treatment beam status. The implementation of the MTCS relies on two control loops: the tracking loop (section 4.3.2) adapts the leaf sequence $\boldsymbol{L}(MU)$ to the target motion, the verification loop (section 4.3.3) controls the treatment beam status based on continuous tracking performance assessments.

Motion monitoring is either based on a single device for direct internal motion monitoring or on two devices for combined external surrogate and internal motion monitoring. The motion monitoring devices report current position observations together with a time-stamp of the position detection to the tracking software. Motion monitoring is either performed continuously or on demand.

The SCC (section 4.1.3) provides MLC position updates every 50 ms, which include leaf and carriage positions and velocities. The SCC accepts position requests for desired leaf motion in every second SCC control cycle. We therefore utilize every second MLC position update to trigger the tracking loop, which sends optimizes MLC position packages to the SCC.

4.3.1 Radiotherapy delivery management

Treatment plan file import

The MTCS can import treatment plan files for all considered delivery modes prior to the actual delivery. The treatment plan defines leaf sequences $\boldsymbol{L}(MU)$, which determine leaf and carriage positions of a radiotherapy delivery as a function of delivered monitor units (MU). For conformal RT and step-and-shoot IMRT treatments, $\boldsymbol{L}(MU)$ is constant during the delivery of a beam or segment, respectively. For dynamic and rotational IMRT deliveries, the leaves are continuously moving during the delivery.

The linac does not report delivered monitor units continuously to the tracking system. For dynamic IMRT deliveries, leaf sequence access is managed through the elapsed delivery time t, which corresponds linearly to delivered the monitor units. The dose-rate of rotational IMRT deliveries is in general not constant. The plan file leaf sequence is therefore expressed as a function of the gantry angle γ, which is continuously reported to the tracking system. To simplify the notation, we express treatment plan leaf sequences as a function of the delivery time t:

$$\boldsymbol{L}(t) := \begin{cases} \boldsymbol{L}(MU(t)) & \text{for dynamic IMRT} \\ \boldsymbol{L}(\gamma(t)) & \text{for rotational IMRT.} \end{cases} \tag{4.2}$$

Record and verify system based delivery

The tracking system alternatively supports tracking deliveries without the need to manually import treatment plan files. For conformal RT and step-and-shoot IMRT (*i.e.,* the delivery modes, which are clinically approved with the ARTISTE radiotherapy suite), the tracking system can access the communication between the record and verify system of the ARTISTE radiotherapy suite and the linac control console. This communication is based on the 'digital machine interface protocol' (DMIP) and includes:

1. Leaf positions transfer for the next segment to be delivered from the record and verify system to the linac control console.
2. Transfer of delivered parameters after completion of a segment from the linac control console to the record and verify system.

DMIP-based deliveries with the MTCS can be performed without manual intervention. The MTCS scans the DMIP communication 1 to import the constant leaf shape $\boldsymbol{L}(MU)$ prior to the delivery of the next segment or beam. The MLC tracking delivery is then performed using the gating interface to interrupt the beam if tracking errors are detected. If the planned monitor units are delivered, the linac control console automatically stops the beam. After detection of the corresponding DMIP message 2, the MTCS waits for the next DMIP message 1 to deliver the next segment.

4.3.2 Tracking loop

The tracking loop calculates leaf positions to adapt the radiotherapy delivery to the current target motion. The actual leaf motion is controlled by the SCC. As outlined in section 4.1.3, there is a considerable latency τ_{mlc} between leaf position requests, which are sent to the SCC, and the corresponding physical leaf motion. Consequently, the tracking loop has to optimize leaf positions for a future point in time $t_0 + \tau_{mlc}$.

The tracking loop performs the following steps:

1. Request MLC shape of the plan file $\boldsymbol{L}(t_0 + \tau_{mlc})$ for future point in time $t_0 + \tau_{mlc}$.
2. Predict the target position $\hat{\boldsymbol{y}}(t_0 + \tau_{mlc})$ for future point in time $t_0 + \tau_{mlc}$.
3. Shift the MLC shape $\boldsymbol{L}(t_0 + \tau_{mlc})$ according to the beam's eye view of the predicted target position $\hat{\boldsymbol{y}}(t_0 + \tau_{mlc})$.
4. Calculate a MLC shape $\boldsymbol{L}_{opt}(t_0 + \tau_{mlc})$, which is optimally adapted to the shifted MLC shape of step 3.
5. Send the optimized MLC shape $\boldsymbol{L}_{opt}(t_0 + \tau_{mlc})$ to the SCC.

The calculation of $\boldsymbol{L}_{opt}(t_0 + \tau_{mlc})$ in step 4 is performed according to the formalism outlined in section 4.2.1. The tracking loop is triggered by every second MLC position update of the SCC.

The MTCS uses either linear regression or support vector regression (see chapter 2) for the prediction of future target positions $\hat{\boldsymbol{y}}(t_0+\tau_{mlc})$. For combined external surrogate and sparse internal motion monitoring, prediction of internal target positions is calculated in two steps: Firstly, the future external surrogate position $\hat{s}_{ext}(t_0 + \tau_{mlc})$ is predicted. Secondly, an external/internal correlation model is used to estimate the future internal target position $\hat{\boldsymbol{y}}(t_0+\tau_{mlc})$ from the predicted external position $\hat{s}_{ext}(t_0+\tau_{mlc})$ and previous external position observations (sections 3.2 and 6.2.1).

The tracking loop obviously controls leaf positions indirectly, as the hardware actuation is performed by the SCC. The tracking loop sends desired leaf trajectory requests to the SCC and does consequently not contain any feed-back of the physically realized leaf motion. The inspection of leaf positioning accuracy is conferred on the verification loop. The leaf position calculations of the tracking loop are however based on real-time observations of the carriage positions as reported by the SCC, which is necessary to compensate for a gravitation induced sag of carriage positions during rotational IMRT deliveries.

4.3.3 Verification loop

The verification loop continuously evaluates the tracking accuracy. It uses the gating interface (section 4.1.3) to turn the treatment beam temporarily off, if tracking errors exceed a predefined tolerance level. The MLC tracking then continues without radiation delivery. If the tracking accuracy stays within the error tolerance for a certain time interval, the radiation delivery is resumed.

The verification loop repeats the following steps every 100 ms:

1. Request MLC shape of the plan file $\boldsymbol{L}(t_0)$ for current point in time t_0.
2. Get the actual target position $\boldsymbol{y}(t_0)$.
3. Shift the MLC shape $\boldsymbol{L}(t_0)$ according to the beam's eye view of the actual target position $\boldsymbol{y}(t_0)$.
4. Calculate a MLC shape $\boldsymbol{L}_{opt}(t_0)$, which is optimally adapted to the shifted MLC shape of step 3.
5. Get the actual MLC shape $\boldsymbol{L}_{act}(t_0)$, that was reported by the SCC.

6. Compare optimal and actual MLC shapes $\boldsymbol{L}_{opt}(t_0)$ and $\boldsymbol{L}_{act}(t_0)$ and quantify the tracking error.

7. Turn the beam on or off.

Steps 1 to 4 of the verification loop basically repeat the corresponding steps of the tracking loop; they are, however, performed for the current point in time t_0 as opposed to the future point in time $t_0 + \tau_{mlc}$, at which the tracking loop is operating.

The verification loop is sensitive to two sources of tracking errors: firstly, target position prediction errors and secondly, mismatches between requested leaf trajectories by the tracking loop and the corresponding physically realized trajectories. The mismatches between requested and actually realized leaf trajectories are caused by hardware limitations, such as the limited leaf velocity or the limited maximum and minimum extension of the leaves from the carriages. The inspection of these mismatches by the verification loop compensates for the lack of feed-back within the tracking loop.

The verification of leaf positioning needs to be performed continuously during radiation delivery. It consequently has to be based on data streams, which are frequently updated. This is problematic for MLC tracking deliveries, which are based on sparse internal motion monitoring combined with continuous external surrogate monitoring (sections 3.2 and 6.2). In this case, step 3 of the verification loop uses the estimation of the actual internal target position $\hat{\boldsymbol{y}}(t_0)$ of the external/internal correlation model. The verification is accordingly insensitive to correlation model inaccuracies.

The quantification of tracking errors in step 6 is based on the comparison of the actual MLC shape $\boldsymbol{L}_{act}(t_0)$ and the MLC shape $\boldsymbol{L}_{opt}(t_0)$ that is optimally adapted to the actual internal target position $\boldsymbol{y}(t_0)$ according to the formalism depicted in section 4.2.1. The inevitable tracking errors due to the finite leaf width do not contribute to the tracking error assessment of the verification loop. The actual measure for tracking errors is the sum of wrongly blocked and wrongly open areas of the MLC shape $\boldsymbol{L}_{act}(t_0)$, normalized to the area of the optimal radiation field $\boldsymbol{L}_{opt}(t_0)$. Leaf positioning errors are more strictly penalized for small fields than for large fields.

4.4 MLC tracking control software

To implement the workflow of the MTCS as depicted in section 4.3, we have developed a large scale C++ software package.[1] The software package includes a total of 43 C++ classes implemented in a total of approximately 14 000 lines of physical source code (without external libraries). It features a graphical user interface (GUI) to select the

[1] Code implementation with support of Dr. S. Nill

different radiotherapy delivery modes, the motion monitoring devices, the prediction models, and the correlation models. It uses the concept of multi-threading to perform multiple tasks simultaneously. The implementation includes a total of 16 threads. A maximum of 9 threads run in parallel to the thread for GUI display in the case of MLC tracking applied to a step-and-shoot IMRT delivery with combined external surrogate and internal target motion monitoring.

The MTCS adopts parts of a previous in-house developed MLC tracking software package (Tacke, 2009; Tacke et al., 2010). The previous system supported MLC tracking of rigid 3D target translation for the delivery modes conformal RT, step-and-shoot IMRT and rotational IMRT. Tracking applied to dynamic IMRT was restricted to 1D target translations and 1D uniform target deformations (Tacke et al., 2007). Motion detection was performed with a potentiometer. Target motion prediction based on a linear extrapolation of the two latest position observation was the limiting factor for tracking accuracy.

A complete software redesign was necessary to allow the following substantial extensions in functionality of the MTCS compared to the previous tracking system:

1. *Motion monitoring:* The MTCS implements clinically applicable motion monitoring based on the Calypso System (section 3.1.1), x-ray fluoroscopy (section 3.1.2) or combined external surrogate and internal motion monitoring (section 3.2).

2. *Prediction models:* The MTCS features the advanced prediction models linear regression and support vector regression. The implementation includes continuous retraining of the predictors to adapt to changes in the respiratory pattern (sections 2.2.3 and 2.2.4).

3. *Correlation models:* The MTCS supports combined external surrogate and internal motion monitoring. It manages position data streams of two devices and implements a support vector regression based correlation model, which is continuously updated during the delivery (sections 3.2 and 6.2).

4. *Verification:* The continuous assessment of tracking accuracy based on the verification loop (section 4.3.3) represents an important step towards quality assurance requirements for any clinical or pre-clinical application.

5. *MLC visualization:* The MTCS features real-time display of actual MLC positions. It also shows the MLC shapes that are optimally adapted to the current target position as calculated by the verification loop. The real-time visualization enables the operator to manually intervene in case of undesired MLC behavior.

6. *Integration of delivery modes:* The MTCS integrates the delivery modes conformal RT, step-and-shoot IMRT, dynamic IMRT and rotational IMRT into one software

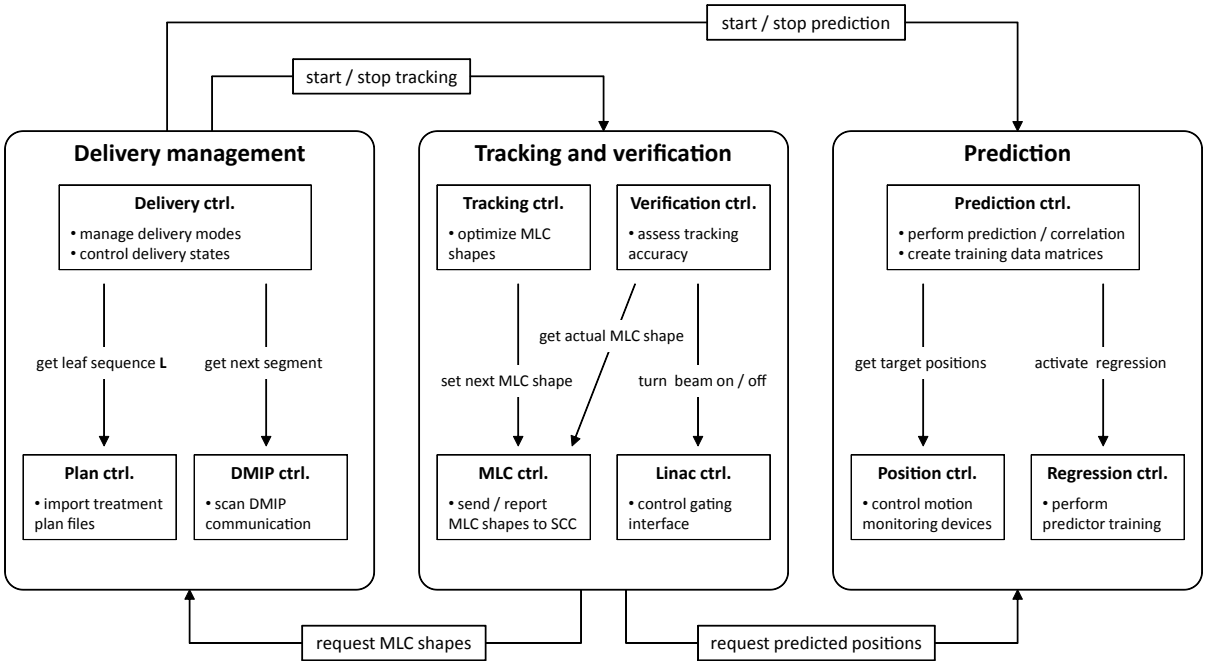

Figure 4.5: Overview of the three modules of the MLC tracking software package as well as the main C++ classes within the modules. The arrangement of the classes within the modules in rows represents the class hierarchy: The classes in the upper row determine the workflow of the MTCS. The classes in the lower row perform clearly defined tasks upon request.

package. The integration avoids duplication of source code, which makes the software more easy to maintain and less prone to programming errors. The GUI allows the selection of the delivery modes as well as the configuration of all important delivery parameters.

4.4.1 Software modules

The guidelines for the MLC tracking software development were maintainability and further extendability. We achieved this through a modular software design, as well as clear interface definition between the modules and classes of the software. Modularity refers to the separation of the program into several distinct components (*i.e.,* the modules) that overlap in functionality as little as possible. Definition of interfaces between C++ classes is achieved naturally by utilizing the concepts of object oriented programming such as encapsulation, information hiding and inheritance. Figure 4.5 shows the three modules of the MLC tracking software package, as well as the most important classes, which are forming these modules. In the following we will discuss the modules in detail.

Delivery management

The delivery management module is responsible for two tasks: firstly, the management of leaf sequences for the different delivery modes and secondly, the control of delivery states. The latter includes activation and deactivation of the tracking and verification module and the prediction module as well as exception handling.

Management of leaf sequences $\boldsymbol{L}(MU)$ for conformal RT, step-and-shoot IMRT, dynamic IMRT and rotational IMRT deliveries relies either on the import of treatment plans through a plan controller class, or on the DMIP-based communication between record and verify system and linac control console (section 4.3.1). DMIP communication is hereby scanned continuously by a DMIP controller class. The delivery specific MLC shape $\boldsymbol{L}(t)$ for time t of the delivery (4.2) is provided to the tracking and verification module through a function `get_next_MLC_shape(t)`.

The control of the delivery states by the delivery management module will be illustrated on the example of a DMIP-based step-and-shoot IMRT delivery:

1. *Treatment preparation:* The delivery controller initializes all C++ classes for the selected delivery. The prediction module is activated and the network connection of the DMIP controller is established.

2. *Beam preparation:* Triggered by the DMIP transfer of the first MLC segment, the carriages of the MLC are positioned. As simultaneous carriage and leaf motion is not possible, carriages have to be positioned prior to the delivery of the segment so that compensation of target motion within the expected range is possible without further carriage adjustment.

3. *Segment preparation:* Upon DMIP transfer, the leaves are positioned to the the MLC shape for the next segment. If the positions are reached, the delivery state is entered automatically.

4. *Delivery:* The tracking and verification loops are started. The tracking delivery is performed with treatment beam control by the verification controller. After the delivery of the planned monitor units, the tracking and verification loops are stopped and the system switches into the segment preparation state.

5. *Delivery halt:* If any hardware or software complication is detected, the delivery management switches into a 'delivery halt' state. Such exceptions can be caused by interlocks from the linac control console, network connection breakups, slow reactions of a software module or the detection of unrealistically large target movements. The delivery management stores delivery parameters such as already delivered monitor units to be able to resume the delivery after the complication is resolved.

Tracking and verification

The module is initialized and stopped by the delivery management module before and after the tracking delivery of each beam or segment. It is responsible for performing the leaf adaptation to the target motion during the delivery of a beam or segment of the radiotherapy delivery.

The classes 'tracking controller' and 'verification controller' perform the tracking and verification loops (sections 4.3.2 and 4.3.3). The MLC controller manages the communication with the SCC and triggers the tracking loop with every second MLC update of the SCC. The Linac controller uses the gating interface to control the treatment beam status. For rotational IMRT deliveries, it additionally monitors the gantry motion and controls the dose-rate modulation.

The tracking and verification controllers request next MLC shapes from the delivery management module. For this purpose, the delivery management module provides a function `get_next_MLC_shape(t)`. The implementation of this function within the delivery management module depends on the actual delivery mode. The different implementations are not visible to the tracking and verification module, which can therefore operate completely independent of the actual delivery mode.

The tracking and verification controllers request predicted and actual positions from the prediction module, respectively. The connection to the prediction module is independent of the motion monitoring strategy. The specific implementation of the functions `get_actual_position()` and `get_predicted_position()` within the prediction module is not visible for the tracking and verification module.

The tracking controller is implemented as abstract C++ class, which defines the interface to the other modules. Individual tracking modes are derived from the abstract class and inherit the interface. The current implementation supports 'no tracking' and 'rigid 3D target translation tracking' modes. The no tracking mode is useful for the delivery of dynamic IMRT or rotational IMRT – the delivery modes, which are not supported by the clinically approved ARTISTE radiotherapy suite. Possible extensions of the MTCS could implement tracking modes for more complex forms of target motion (for example rotation and deformation) or tracking modes, which additionally compensate for the motion of nearby organs at risk.

Prediction

The prediction module provides future target positions $\hat{\boldsymbol{y}}(t_0 + \tau_{mlc})$ for the compensation of the system latency. Additionally, it predicts actual internal target positions $\hat{\boldsymbol{y}}(t_0)$ from the external surrogate signal based on a external/internal correlation model.

The module performs continuous retraining of both the future target position predictor and the external/internal correlation model. It is activated by the delivery management module at the beginning of a treatment. Unlike the tracking and verification module, the prediction module is not deactivated until the treatment is finished. Adaptive predictor retraining is performed throughout the complete treatment.

Upon activation through the delivery management module, the position controller initializes the motion monitoring devices and stores the reported positions. The prediction controller then starts the training of prediction and correlation models. It therefore arranges the stored target positions into training data matrices matrices X and Y containing input vectors and target scalars (section 2.2.3). It then selects one of the regression controllers (*i.e.,* linear regression or support vector regression) to establish the prediction function f based on the training data matrices.

Prediction of 3D motion data is performed for each coordinate independently. Data preprocessing, as depicted in section 2.2.2, is applied to eliminate baseline drifts and breathing amplitude fluctuations. The optimal parameter vector $\boldsymbol{\beta}$ of the linear regression prediction function (2.8) is calculated by solving (2.10) analytically. Quick matrix inversion is performed using LU-decomposition. The optimization problem (2.19) for the support vectors regression prediction function (2.18) is solved using the C++ package LIBSVM (Chang and Lin, 2001). The linear regression and support vector regression controllers are derived from an abstract regression controller class, which defies the interface to the prediction controller.

The current implementation includes prediction controllers for a single internal motion monitoring device or combined external surrogate and internal target motion monitoring. They are derived from an abstract prediction controller class. The individual prediction controllers implement different versions of the functions `get_actual_position()` and `get_predicted_position()`, which constitute the interface to the tracking and verification module.

5 MLC tracking based on the Calypso System

This chapter presents various experiments performed with the MLC tracking system integrated with the Calypso System (section 3.1.1) for motion monitoring. In section 5.1, we present measurements of the total system latency as well as an analysis of the main latency contributors. In section 5.2, we present experiments of MLC tracking with regular sinusoidal motion patterns. The study focuses on dosimetric tracking accuracy assessments for conformal radiotherapy and step-and-shoot IMRT deliveries. In section 5.3, MLC tracking is applied to irregular respiratory motion and prostate motion traces. The geometric and dosimetric tracking performance is not only assessed for MLC tracking, but is also compared to a patient couch tracking system, which was installed at our research ARTISTE linac in a multi-institutional cooperation. In section 5.4, we evaluate the application of MLC tracking to dynamic IMRT deliveries.

5.1 Latency

Processing times within the individual components of the integrated tracking system add up to a total system latency. We formally define system latency as the lag time between an initial target motion and the corresponding beam-target realignment. Precise knowledge of the total system latency is necessary, as it defines the lookahead length of the predictor.

The following sections show measurements of the total system latency as well as an analysis of the contribution of the individual components of the MTCS to the total system latency.[1]

5.1.1 Experimental setup

Figure 5.1 shows a photograph of the experimental setup for the latency measurements. A simple phantom, which consists of a stack of solid water slices, is mounted on a motion

[1] Measurements performed by M. Menten.

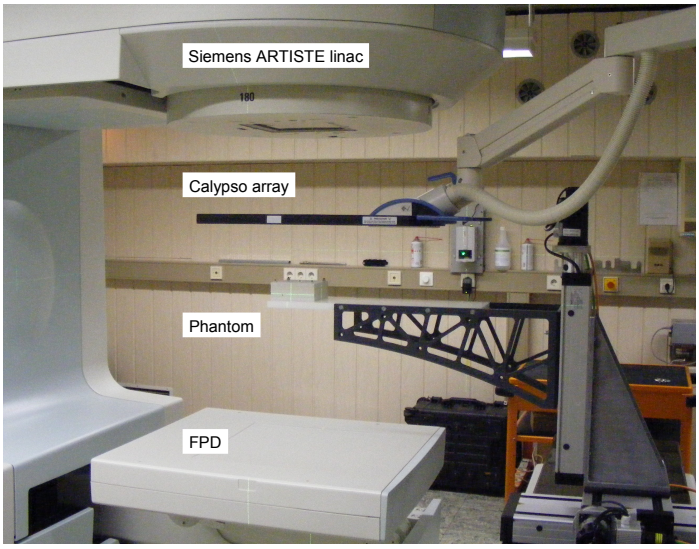

Figure 5.1: Experimental setup for MLC tracking based on the Calypso System. Phantom motion is detected with the Calypso array. The flat panel detector (FPD) captures phantom and MLC motion at the same time.

platform. The phantom has the three Calypso transponders as well as a radioopaque marker embedded. The motion platform can reproduce arbitrary 3D trajectories with sub-millimeter precision. The Calypso System monitors the phantom motion at a frame-rate of 25 Hz and reports it to the MTCS. The MTCS adapts the MLC aperture to the reported target motion. The on-board flat panel detector (FPD) acquires portal images continuously during the tracking experiments. The portal imagery allows capturing the motion of the radioopaque marker in the phantom and the motion of the MLC aperture at the same time within each imaging frame.

5.1.2 Total system latency

Total system latency was determined by switching the prediction algorithm of the MTCS off and measuring the resulting lag time between target motion and the corresponding beam-target realignment using portal imagery. The phantom was moved on a 1D sinusoidal trajectory parallel to the leaf travel direction. During radiation delivery in tracking mode, portal images were acquired with an update rate of 15 Hz. A circular MV radiation field with a diameter of 5 cm was chosen. The centroid trajectories of both the circular field aperture and the radioopaque marker were determined from the portal imagery automatically. Sine-functions were fitted to the resulting sampled trajectories of the MV field and the target. The latency could be read off the phase difference of the two fitted curves.

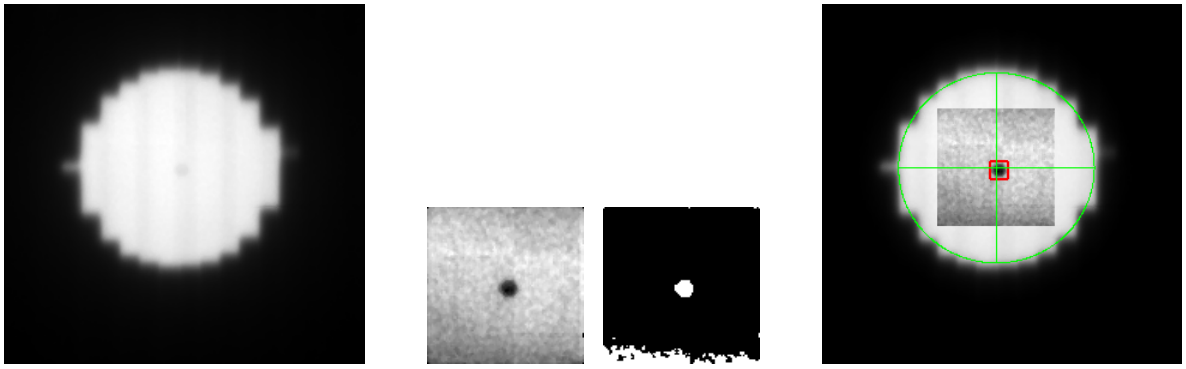

(a) (b) (c) (d)

Figure 5.2: Detection of the centroids of the circular radiation field and the radioopaque marker. (a) raw image, (b) region of interest (ROI) after preprocessing, (c) binary image of the ROI, (d) result of the image analysis – the green cross lines indicate the centroid of the radiation field; the red square highlights the metal ball.

Analysis of portal imagery

Figure 5.2a displays a portal image of the circular radiation field including the shadow of the radioopaque marker. The centroid position of the circular field is determined in two steps: (1) conversion of the portal image into a binary image by applying a threshold of 60% of the mean pixel value within the MV field, (2) calculation of the geometric centroid of the points in the resulting binary image with pixel value 1.

After determination of the centroid of the circular MV field, the radioopaque marker was detected within a rectangular region of interest (ROI) around the centroid of the radiation field. The size of the ROI was chosen such that the ROI was completely inside the radiation field. The algorithm for radioopaque marker detection was essentially adopted from Rau et al. (2008). The following steps were performed to detect the marker within the ROI:

1. Image preprocessing including noise reduction through a median filter as well as contrast maximization. The ROI after preprocessing is displayed in figure 5.2b.

2. Threshold based conversion into a binary image (figure 5.2c).

3. Labeling of the multiple components of the binary image (*i.e.,* the connected areas with pixel value 1 within the binary image).

4. Analysis of geometric properties of the components – such as area, minor and major axis length, eccentricity – to distinguish the real radioopaque marker from spurious components.

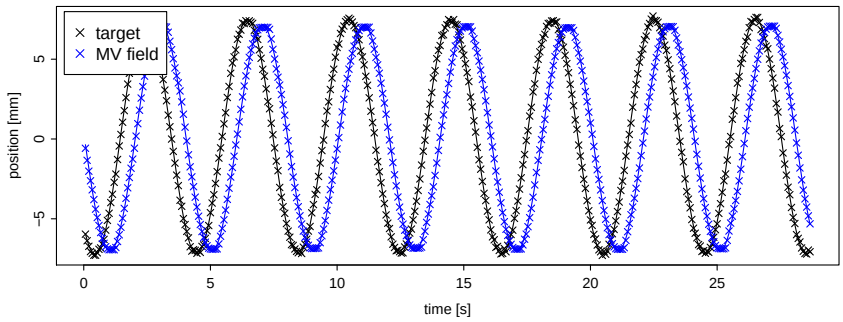

Figure 5.3: Trajectories of centroids of radioopaque marker and circular MV field as extracted from the portal imagery (crosses). The MV field is lagging behind the target. The total system latency can be read off the phase difference of the fitted sine-functions (solid lines).

Steps 2 to 4 were repeated with iteratively increased threshold values until the true marker position was found (*i.e.,* until one of the components fulfilled all constraints on its geometric properties). The marker position is then given as the geometric centroid of this component.

Results

Figure 5.3 displays the result of the portal image analysis for a radiation delivery in tracking mode without target motion prediction. The circular MV field is clearly lagging behind the target motion. The latency is given by the phase shift of the sinusoidal fits to the target and MV field trajectories. Five such measurements yielded a total system latency of $\tau_{\text{total}} = (586 \pm 3)$ ms.

5.1.3 Analysis of latency contributors

The MTCS writes dynamic log-files continuously during radiation deliveries. Amongst others, the following data is stored in the MTCS log-files: (1) the target positions reported by the Calypso System to the MTCS, (2) predicted positions by the MTCS, (3) the MLC shape requests sent to the SCC (section 4.1.3), and (4) the physically realized MLC shapes reported by the SCC. All log-file entries contain time stamps of the logged events. Log-file analysis therefore allows us to quantify the contribution to the total system latency of motion monitoring by the Calypso System, adaptive MLC shape optimization by the MTCS, and physical leaf position adaptation by the SCC.

Calypso latency The Calypso System reports 3D centroids of the three implanted transponders. An individual Calypso position update is based on the detection of the

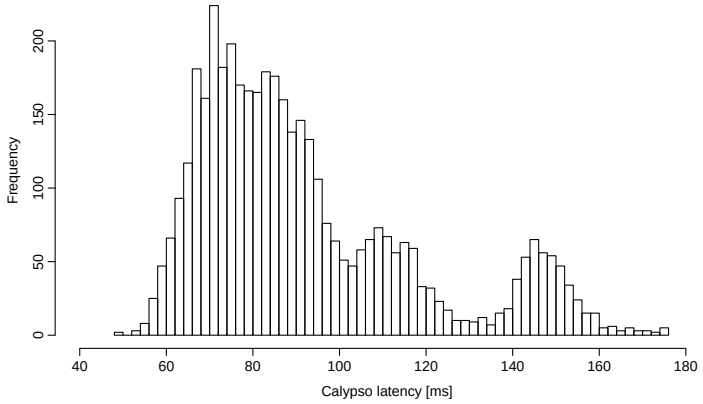

Figure 5.4: Histogram of position detection latencies reported by the Calypso System.

3D position of only one transponder and the corresponding centroid recalculation. The Calypso System additionally reports an effective time-stamp of position detection, which corresponds to a weighted mean value of the three latest individual transponder position detection times. The latency of each Calypso position update is given as the difference between the time of position report to the MTCS and the corresponding effective Calypso time-stamp.

Figure 5.4 displays the distribution of Calypso latencies as extracted from the log-files of the five latency measurements, which were also used for the portal image analysis. The wide distribution of Calypso latencies ranges from 50 ms to 180 ms. The distribution exhibits three clearly distinguishable peaks centered roughly at 80 ms, 110 ms and 145 ms. Analysis of the position packages in the peak at 145 ms suggested that these packages correspond to transponder detection failures; the packages exactly repeated the position information of the previous package. We quantify the Calypso position detection latency as the mean value of the distribution of reported latencies: $\tau_{\text{calypso}} = (93 \pm 27)$ ms.

Effective Calypso latency Calypso positions updates are not synchronized to the iterations of the tracking loop and the corresponding optimized MLC shape requests sent to the SCC. Poulsen et al. (2010b) therefore proposed an effective position detection latency, which depends on the sampling frequency f of the motion monitoring system:

$$\tau_{\text{eff}} = \tau + \frac{1}{2f} \,. \tag{5.1}$$

Given the Calypso update rate of 25 Hz, the expected effective Calypso latency accordingly amounts (113 ± 27) ms.

The effective position detection latency can also be measured with the MTCS log-files. Log-file entries of predicted target positions are written at the beginning of the tracking

loop. For the latency measurements, target motion prediction is turned off. The corresponding predictor 'none' logs the latest 3D target position update provided by the Calypso System with the actual time stamp. The lag time between the target trajectories based on the effective Calypso position detection time-stamp on the one hand and target trajectories based on the predictor 'none' time stamp on the other hand corresponds to the effective position detection latency.

Similar to the latency analysis based on flat panel imagery, this lag time was quantified through the phase difference of sinusoidal fits. The effective Calypso latency calculation for the five measurements yielded: $\tau_{\text{calypso,eff}} = (112 \pm 6)$ ms. This value is in perfect agreement with the expected value based on (5.1).

Tracking loop The MLC shape log-file entries include carriage and leaf positions as well as the time-stamps for MLC shape transfer to or from the SCC. The tracking loop is triggered by every second MLC shape update of the SCC and ends with a MLC shape request sent to the SCC (section 4.3.2). The calculation time for one iteration of the tracking loop can therefore be quantified as the difference of time-stamps between corresponding SCC position updates and requests. The distribution of tracking loop computation times within the five measurements yielded $\tau_{\text{loop}} = (1.4 \pm 0.7)$ ms.

Total system latency The total system latency can be calculated from the log-files of the target position trajectory and the centroid trajectory of physically realized MLC shapes as reported by the SCC. The centroid coordinate of the circular MLC aperture parallel to the leaf travel direction is hereby quantified as the mean value of the middle positions of all open leaf pairs. In five measurements we obtained a total system latency of $\tau_{\text{total,log}} = (615 \pm 8)$ ms. This value is about 30 ms larger than the corresponding value of the portal image analysis.

The SCC does not report a time stamp for leaf position detection with its MLC shape updates. The log-file analysis used the time-stamp of MLC shape reports to the MTCS as the time-stamp for leaf position detection. It consequently over-estimated the total system latency. We assume that the over-estimation of the total system latency is solely caused by the missing time-stamp for leaf position detection within SCC updates. We neglect possible systematic errors in the effective time-stamp calculation of the Calypso System. Consequently, time axes of MLC trajectories reported by the SCC have to be shifted by (29 ± 9) ms towards smaller values.

MLC latency We quantify the MLC latency as the lag time between an MLC position request sent to the SCC and the corresponding physical leaf adaptation. The log-file analysis provides MLC aperture centroid coordinate trajectories parallel to the leaf travel

Table 5.1: Latencies of the components of the tracking system.

Contributor	Latency [ms]
Total (portal imagery)	586 ± 3
Total (log-files)	615 ± 8
Calypso position detection	93 ± 27
Calypso effective	112 ± 6
Tracking loop	1.4 ± 0.7
MLC	503 ± 5
MLC corrected	473 ± 10

direction for MLC shapes sent to or received from the SCC. The phase shift of sinusoidal fits to these trajectories averaged over five measurements amounts $\tau_{\mathrm{mlc}} = (503 \pm 5)$ ms.

The aforementionned over-estimation of the total system due to the missing time-stamp for leaf position detection within SCC updates also leads to an overestimation of the MLC latency. Taking into account the correction of time axes of MLC trajectories reported by the SCC by a shift of (29 ± 9) ms towards smaller values yields a corrected MLC latency of $\tau_{\mathrm{mlc,corrected}} = (473 \pm 10)$ ms.

5.1.4 Summary

We have precisely measured the latency of the integrated tracking system using portal imagery. Based on a log-file analysis, we have additionally quantified the contribution to the total system latency of the motion monitoring by the Calypso System, the calculation of optimized MLC positions by the the MTCS and the physical MLC adaptation by the SCC. We have observed a discrepancy between portal imagery and log-file analysis. We have identified a missing time-stamp within MLC updates of the SCC as the source of the discrepancy and have corrected the MLC latency accordingly. The results are summarized in table 5.1.

The MLC latency of (473 ± 10) ms is by far the main contribution to the total system latency. It is also substantially larger than the MLC latency of a similar MLC tracking developed at Stanford University (Keall et al., 2006a; Sawant et al., 2008), for which Poulsen et al. (2010b) reported a MLC latency of only 52 ms. The total latency of the Stanford MLC tracking system integrated with the Calypso System amounts 220 ms (Sawant et al., 2009); it is almost three times smaller than the latency of our tracking system.

5.2 Regular motion tracking

In the following, we report on the performance of the MLC tracking platform integrated with the Calypso System. Tracking performance is characterized in terms of geometric and dosimetric accuracy. The evaluation is based on conformal RT and IMRT radiation deliveries applied to different phantoms moving on sinusoidal trajectories in two dimensions.

5.2.1 Materials and methods

Experimental setup

The experimental setup is displayed in figure 5.5. Except for the phantom, the same equipment as for the latency measurements was used. The displayed phantom mimics a human thorax. It consists of solid water slices of 10 mm thickness with lung equivalent inserts and a tumor inlay.

The following coordinate system was used throughout the present study. The origin coincides with the isocenter. The x-axis points in the left-right direction for a patient in the head-first, supine position. The y-axis points in superior-inferior direction toward the linear accelerator, and the z-axis points upward in the anterior-posterior direction. The collimator angle was set to 90° such that the leaf travel direction coincided with the y-axis.

Prediction of future target positions was based on linear regression (section 2.2.3). The model parameters were however not systematically optimized. Preprocessing – as depicted in section 2.2.2 – was not necessary, as the sinusoidal motion patterns do not exhibit baseline drifts or amplitude fluctuations.

To assess the geometric accuracy of the tracking system, the phantom was moved on a Lissajous curve consisting of two sine waves parallel and perpendicular to the leaf travel direction with a periodicity of 4.5 s and 6.5 s. Portal images were acquired continuously during radiation delivery in the target tracking mode. Tracking errors were calculated from the distance between the centroids of the radiation field and the metal ball derived from the portal images.

Radiologic accuracy

For the assessment of the radiologic benefits achievable with the tracking system, radiochromic films (Gafchromic EBT, International Specialty Products, Wayne, NJ) placed

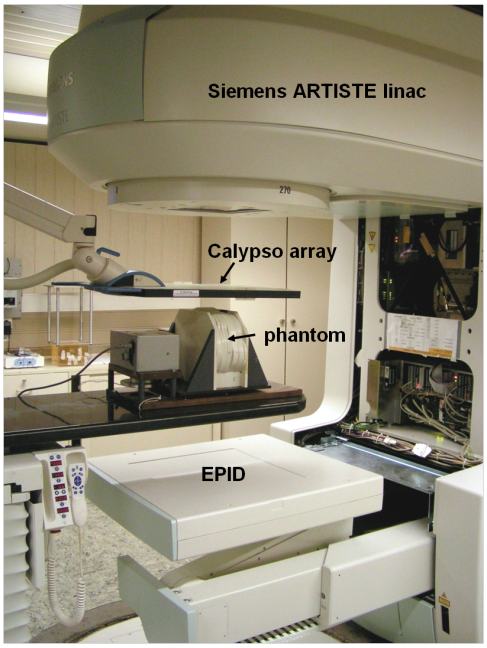

Figure 5.5: Experimental setup for MLC tracking based on the Calypso System. Phantom motion is detected with the Calypso array. The flat panel detector (FPD) captures phantom and MLC motion at the same time.

in between the solid water slices of the phantoms were irradiated. For each set of measurements, three scenarios were investigated: radiation delivery in static MLC mode to the non-moving phantom defining the reference standard for the tracking experiments, delivery in static MLC mode to the moving target, and delivery in the dynamic MLC tracking mode.

The films were scanned and normalized to the maximal dose of the reference standard measurement for each set of experiments. A comparison to this reference measurement was performed in terms of the gamma-test, which brings the dose difference and distance-to-agreement maps together (Low and Dempsey, 2003). For the calculation of the gamma-metric, we used the maximal value of the reference dose distribution as the reference value for the accepted percentage of dose deviation.

We assumed that the static radiation delivery to the non-moving target represented optimal delivery in terms of target coverage and healthy tissue sparing and, therefore, considered the gamma-index evaluation (i.e., the estimation of the similarity of a dose distribution to this reference standard distribution) as an appropriate measure of dosimetric accuracy. Advancing from a technical to a more clinically relevant viewpoint, three kinds of experiments using two phantoms were performed:

1. An open, circular radiation field 5 cm in diameter in the isocenter was applied to a simple phantom, which consisted of a stack of water equivalent slices. The phan-

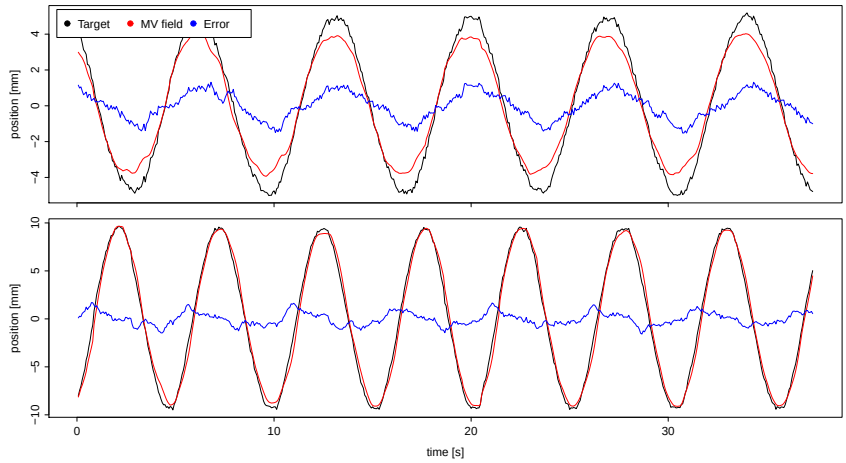

Figure 5.6: Tracking accuracy in direction parallel (upper panel) and perpendicular (lower panel) to leaf travel direction. Trajectories of the centroid of the radiation field, the target position and the difference between these curves are displayed.

tom was moved both in a twodimensional Lissajous curve and in one-dimensional sinusoidal trajectories parallel and perpendicular to the leaf travel direction with a periodicity of 4.5 s and 6.5 s and amplitude of 2 cm and 1 cm, respectively. This allowed the examination of the influence of the finite leaf width to the total delivery accuracy, which only played a role for the compensation of movements perpendicular to the leaf travel direction.

2. A single beam out of a step-and-shoot IMRT plan (see below) was applied to the same simple phantom in two-dimensional tracking mode. Again, the phantom was moved on the aforementioned Lissajous curve.

3. A complete step-and-shoot IMRT plan was applied to the thorax phantom. The transponders were embedded in the tumor inlay. The phantom was moved on a $\cos^4(t)$-shaped trajectory in y-direction with an amplitude of 2.4 cm. The slices of the phantom are aligned perpendicular to the motion axis of the phantom. The delivery was performed in the completely automatic DMIP mode (section 4.3.1). The standard five-beam treatment plan was generated for a computed tomography scan of the lung phantom.

5.2.2 Results

Geometric accuracy

In figure 5.6, the trajectories of the centroid of the field aperture and the target position are plotted, together with the tracking error (i.e., the difference between these

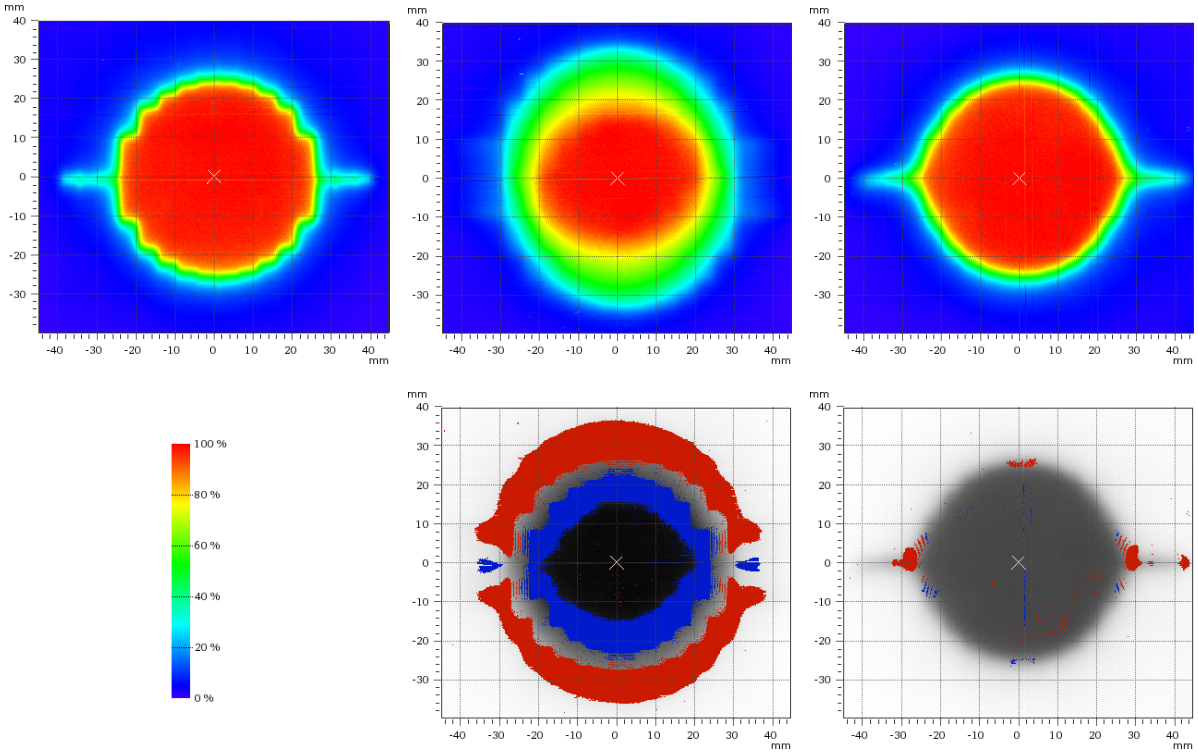

Figure 5.7: Dose distributions of the circular field applied to the target moving in two directions (Upper row). Gamma-test results displayed as grayscale dose distribution with gamma-indexes > 1 marked in red for overdosage and blue for underdosage (Lower row).

two curves). In both cases, the absolute of the tracking errors remained below 1.6 mm. A root mean squared error of 0.69 mm mm and 0.80 mm was observed for the directions parallel and perpendicular to the leaf travel direction, respectively. Parallel to the leaf travel direction, the maximal tracking errors occurred in the regions of the greatest leaf velocities. Perpendicular to the leaf travel direction, the greatest deviations were observed in the peaks of the trajectory.

Radiologic accuracy

The upper row of figure 5.7 shows the dose distributions for the circular field applied to the non-moving target in the static MLC mode, the target moving in two directions in the static MLC mode, and the moving target in the dynamic tracking MLC mode. For the no-tracking case, strong blurring of the static reference dose distribution was observed. The high-dose area inside the 95% isodose line decreased from 13.8 cm^2 to 8.1 cm^2. In contrast, the region between the 20% and 95% isodose lines increased from 11.7 cm^2 to 24.6 cm^2. Both effects were negligible in the tracking case. Except for a

Table 5.2: Failure rates of the gamma-test for a circular field applied to different target motion patterns.

	Without tracking		With tracking	
Target motion	2%/2mm [%]	3%/3mm [%]	2%/2mm [%]	3%/3mm [%]
Two-dimensional	59.7	40.6	3.3	0.5
Parallel	51.1	32.3	0.6	0.1
Perpendicular	14.8	1.5	3.6	0.9

smoothing of the sharp edges, the reference dose distribution could be well restored in the tracking case.

The lower row of figure 5.7 shows maps of the points failing the 2%/2mm gamma-criterion (i.e., having a gamma-value > 1). A large ring of points receiving an underdosage (blue spots) inside the target volume followed by an overdosage region (red spots) outside the target volume could be observed for the no-tracking case. In contrast, only very few points near the closing position of the adjacent leaves failed the gamma-test in the tracking case.

Table 5.2 lists the gamma-test results for tracking in two dimensions and for tracking along the directions parallel and perpendicular to the leaf travel direction. For tracking parallel to the leaf travel direction, an almost complete recovery of the reference dose distribution was observed. Only 0.6% of the evaluated points failed the 2%/2mm gamma-criterion. For tracking perpendicular to the leaf travel direction, an increased failure rate of 3.6% was observed. For target displacements perpendicular to the leaf travel direction, the planned field shape could not be completely restored because of the finite leaf width of 5 mm, which was therefore the main contribution to the radiologic inaccuracy for twodimensional tracking in this experiment.

Figure 5.8 shows the results of the film evaluation of a single IMRT beam applied to a target moving in two dimensions. Again, dose distributions (upper row) and maps of points failing the 2%/2mm gamma-criterion (lower row) are displayed. For the tracking case, an improvement of the strong blurring effect of the no-tracking case was clearly visible. The gamma failure rate decreased from 55% to 15.6% and from 31% to 7.6% for the 2%/2mm and 3%/3mm criterion, respectively. However, an underdosage of the sharp target edges and an overdosage of the surrounding areas above and below the target area remained when tracking was applied.

In a third set of measurements, the radiologic effect of our tracking approach to a complete IMRT plan for a lung tumor site was assessed. Four films were sandwiched between the slices of the lung phantom. Two films (Films 2 and 3) were placed near the center of the phantom's tumor inlay; Film 1 was placed 5 mm inside the target volume and

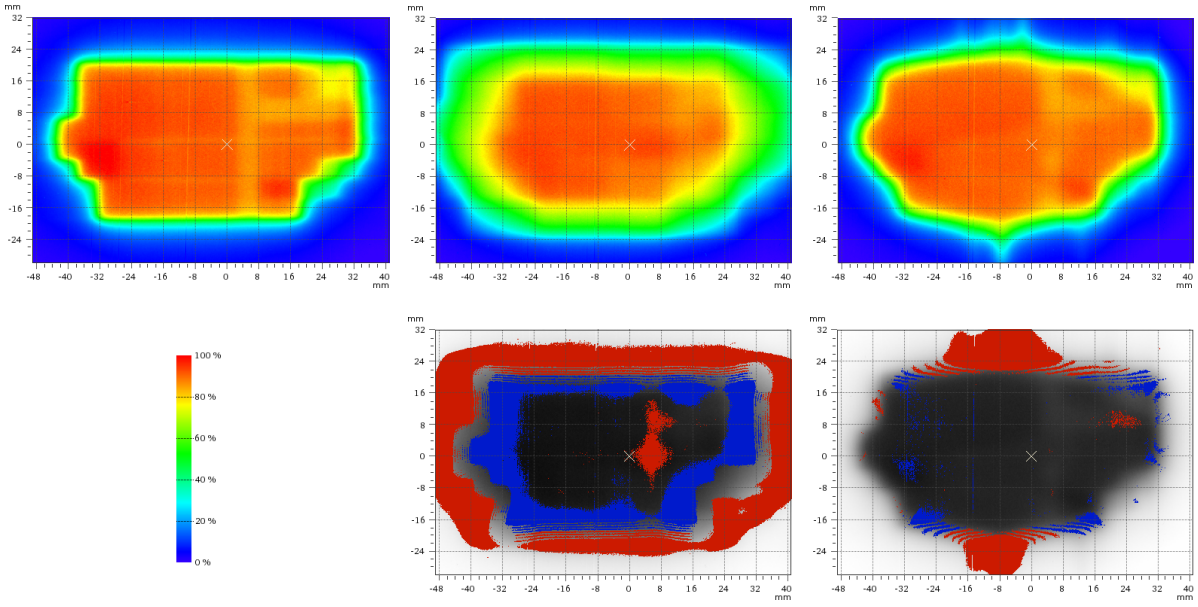

Figure 5.8: Dose distributions of a single IMRT beam applied to the target moving in two directions (Upper row). Gamma-test results displayed as grayscale dose distribution with gamma-indexes >1 marked in red for overdosage and blue for underdosage (Lower row).

Film 4 was placed 5 mm outside the target volume. Although for the two central sections (Films 2 and 3), the target motion induced only minor discrepancies between planned and delivered dose, the planned dose distribution to Films 1 and 4 was completely compromised. The 2%/2mm gamma-analysis results are listed in table 5.3.

Figure 5.9 shows the horizontal dose profiles of Films 1 and 4. Both the strong underdosage of Film 1 and the overdosage of Film 4 observed in the no-tracking case were substantially reduced using the tracking technique. Tracking resulted in a reduction of the mean overdosage of Film 4 (i.e., the mean dose difference between the measurement and the reference standard scan), from 20.9%to 5.2% of the maximal target dose.

5.2.3 Discussion

The presented experimental results have demonstrated the feasibility of intra-fractional motion compensation using a Siemens 160 MLC based on target motion monitoring with the Calypso System. We could demonstrate highly accurate target tracking and showed that even complex IMRT dose distributions could be recovered to a high degree using the integrated tracking system. The experiments represented the ideal case of perfectly regular target motion patterns. The linear regression predictor therefore induced almost no error to the overall system, despite the large system latency.

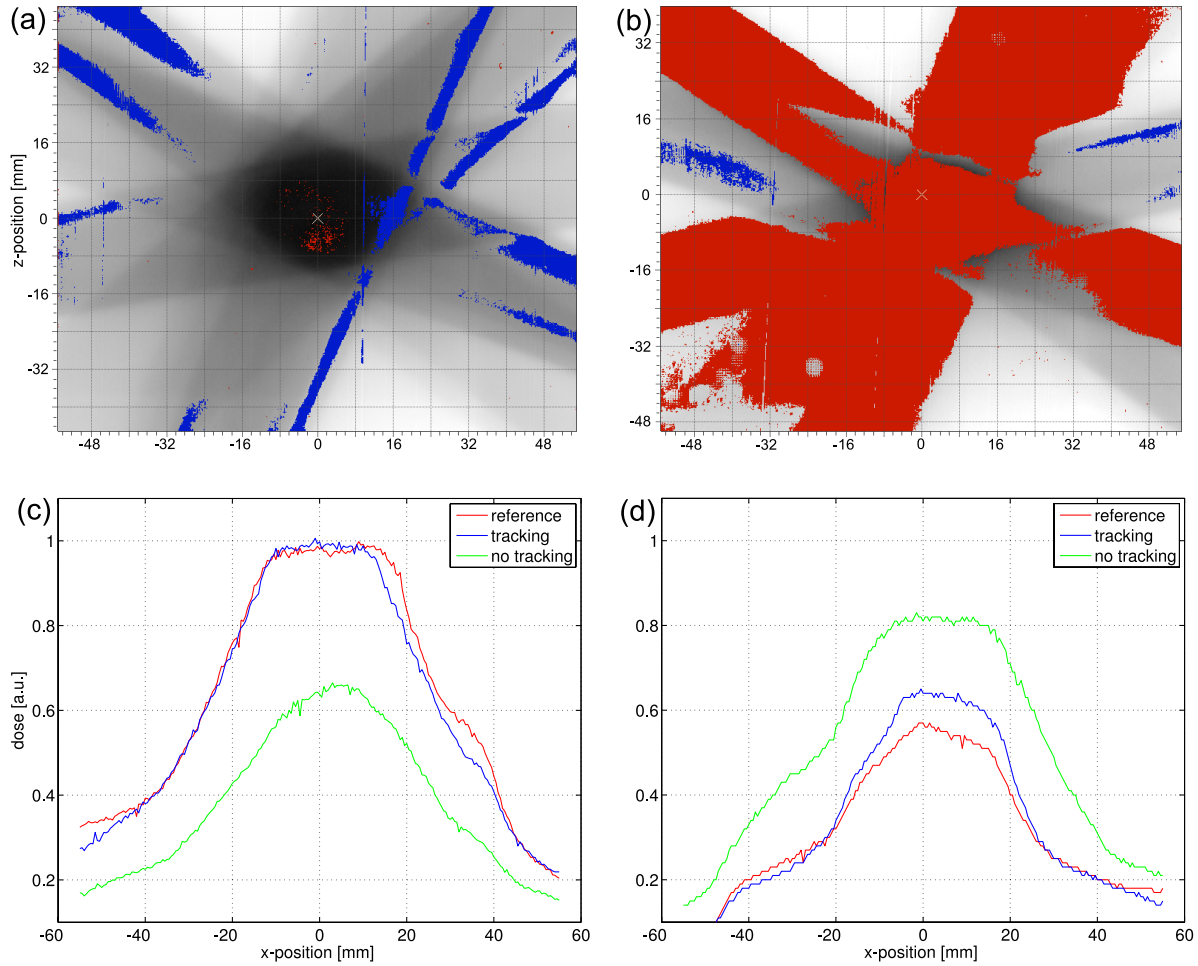

Figure 5.9: (a,b) Gamma-test results for Films 1 and 4 displayed as dose distributions recorded on tracking film, with points failing 2%/2mm gamma-criterion marked in red and blue for overdosage and underdosage, respectively. (c,d) Horizontal profiles of films 1 and 4 for reference, tracking, and no-tracking cases. Dose values normalized to maximal dose delivered to tumor.

Film dosimetry demonstrated considerable improvements for all the investigated scenarios. An almost complete recovery of the planned dose distribution was observed for open field tracking. A 2%/2mm gamma-failure rate of 0.6% and 3.6% for target motion parallel and perpendicular to the leaf travel direction, respectively, was observed. These findings emphasize that the prediction errors play no role for the regular motion traces used in our study. The tracking accuracy was primarily limited by the finite leaf width of 5 mm in the isocenter.

For a single IMRT beam applied to the phantom moving in two dimensions, the 2%/2mm gamma-failure rate was reduced from 54.6% to 15.6% by applying the tracking technique. Again, the remaining inaccuracy could be addressed to the finite leaf width. Because several segments of the IMRT field exhibited large leaf apertures directly adjacent to a

Table 5.3: Failure rates of the gamma-test for a five beam IMRT plan applied to the lung phantom moving on a 1D $\cos^4(t)$ trajectory with an amplitude of 24 mm and a period of 5 s.

	Without tracking		With tracking	
Film position	2%/2mm [%]	3%/3mm [%]	2%/2mm [%]	3%/3mm [%]
1	99.6	98.5	8.6	2.2
2	10.3	2.4	0.3	0.0
3	27.6	11.1	1.8	0.1
4	98.6	96.7	65.1	51.8

For the no tracking case, the treatment isocenter was placed in full exhale phase of the target trajectory. Calculation of the gamma-metric refers to the same normalization value for the four films (*i.e.,* the maximal dose recorded on the reference measurement).

closed leaf pair, the effect of the finite leaf width on the IMRT dose distribution was by far more pronounced than for the circular field.

To investigate the clinical benefits of the tracking system, the dosimetric accuracy was assessed for a five-beam IMRT plan. The strong underdosage of the tumor edge traveling out of the treatment field without tracking applied could be compensated effectively. The 2%/2mm gamma-failure rate decreased from 99.6% to 8.6%. The overdosage of the surrounding tissue traveling into the treatment beam without tracking recorded on Film 4 showed that the dose gradients intended to protect the healthy tissue from an excessive dose were severely compromised without tracking. This effect could not be completely eliminated.

Nevertheless, a reduction of the 3%/3mm gamma-failure rate from 96.7% to 51.8% and of the mean overdosage from 20.9% to 5.2% of the target dose observed for a film placed 5 mm outside the target volume showed at least considerable improvement when the tracking technique was applied. The dose profiles displayed in figure 5.8 show that the maximal dose recorded on that particular film for the reference measurement was approximately 55% of the maximal dose delivered to the tumor. This indicates that the film was placed in a region of steep dose gradients. The remaining inaccuracy for the dose delivery thus showed the sensitivity of the steep dose gradients achievable with IMRT to minor target displacements. Even for the idealized conditions of this tracking experiment, we were not able to completely restore the planned dose distribution.

5.3 Comparative performance of MLC tracking and robotic couch tracking

Compensation of intra-fractional organ motion based on MLC tracking adapts the treatment beam to the observed target motion. Another approach to intra-fractional motion compensation is robotic patient couch tracking (D'Souza and McAvoy, 2006; Wilbert et al., 2008). A robotic patient couch is used to move the entire patient to countersteer the target motion, *i.e.* the patient couch is moved such that the tumor position is fixed within the room coordinate system. Consequently, patient couch tracking does not influence the radiation delivery process.

In a multi-institutional collaboration, we have performed a comparison study of MLC tracking and robotic couch tracking. To achieve equal conditions for both tracking systems, an integrated couch tracking system developed at the University of Würzburg (Wilbert et al., 2008) was installed at our institution. The couch tracking system relies on motion compensation through the HexaPOD robotic table top (Medical Intelligence, Schwabmünchen, Germany). The HexaPOD control system was modified to receive target position information from the Calypso System.

The study included lung tumor and prostate motion tracking. Tracking performance was assessed geometrically through portal imagery and dosimetrically through film dosimetry.[2]

5.3.1 Materials and methods

Experimental setup

Figure 5.10 displays the experimental setup for the tracking experiments. The HexaPOD was mounted on top of the standard Siemens treatment couch. The 4D motion stage was fixed on the HexaPOD. For the couch tracking deliveries, the HexaPOD countersteered the motion of the 4D stage so that the phantom's position in the room coordinate system was minimized. During MLC tracking deliveries we locked the HexaPOD position. The displayed cylindrical phantom was used for the prostate motion tracking experiments. It was fixed to the motion stage and contained the Calypso transponders. The Calypso System detected transponder motion and reported it to either the MTCS or to the HexaPOD control system. For the lung tumor tracking experiments, the cylindrical phantom was replaced by the previously described simple phantom, which consists of stacked solid water slices. The lung tumor tracking experiments additionally utilized the on-board flat panel imager to assess geometric tracking accuracy as outlined in section 5.1.2.

[2]Measurements and initial data evaluation performed by M. Menten

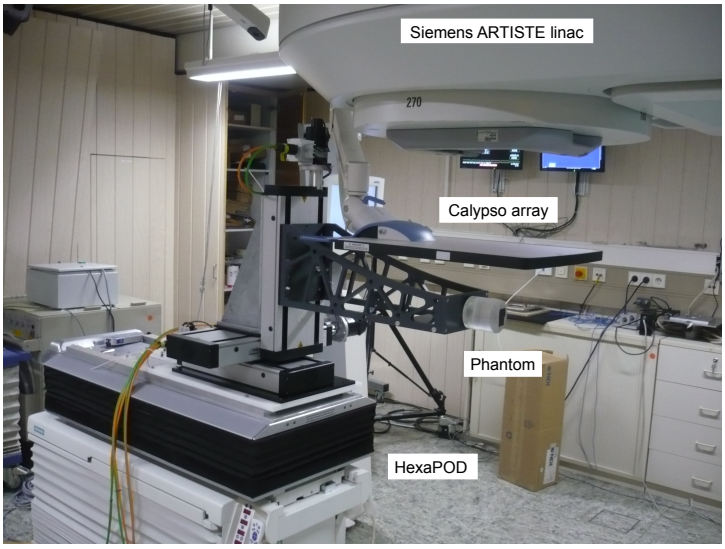

Figure 5.10: Experimental setup for MLC and HexaPOD tracking. The HexaPOD is mounted on top of the Siemens treatment couch. Phantom motion is detected with the Calypso array.

The HexaPOD control system

The HexaPOD tracking control system used the target position updates of the Calypso System to minimize the phantom motion in the room coordinate system. The motion of the HexaPOD was detected with a infrared camera system (Polaris, Waterloo, Ontario, Canada), which monitored a passive infrared marker tool fixed to the HexaPOD. A closed-loop control algorithm combined the feedback from the phantom and HexaPOD position updates to maintain the desired state – *i.e.,* a non-moving phantom position.

Lung tumor motion tracking

The study included a total of 8 patient lung tumor motion traces from the breathing data set introduced in section 2.2.1. The breathing data samples contained internal 3D tumor motion trajectories acquired with stereoscopic x-ray fluoroscopy at 30 Hz (Berbeco et al., 2005). The coordinates of the breathing traces were interchanged so that the largest (second largest) breathing amplitude was in y-direction (x-direction) for the coordinate system introduced in section 5.2.1. The gantry angle was 0° and the collimator angle was 90° so that the leaf travel direction was parallel to the y-axis.

The breathing traces had a minimum length of 80 s. The first 30 s of each breathing trace were reserved for predictor training. The HexaPOD control system used a prediction algorithm to compensate for Calypso System latencies. The MTCS used a support vector regression predictor (section 2.2.3) to compensate for the total system latency of

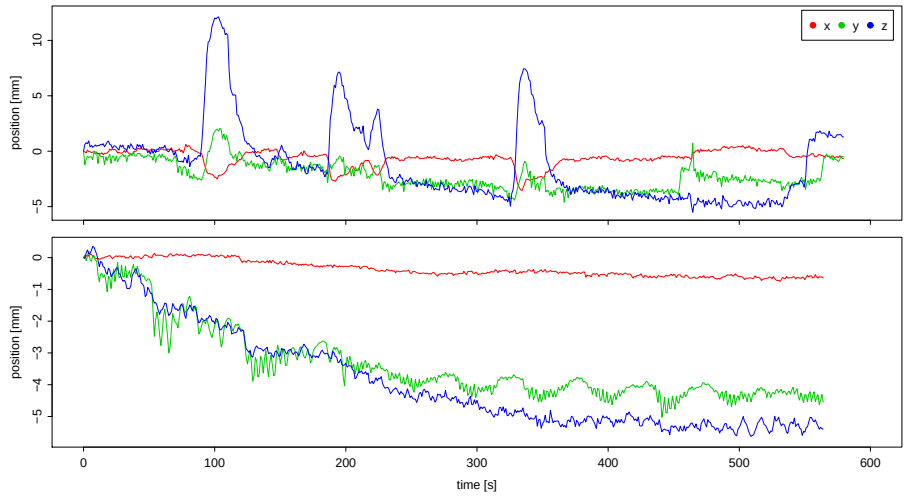

Figure 5.11: Example 3D prostate traces. Traces 2 (upper panel) and 4 (lower panel).

586 ms (section 5.1). Tracking performance was assessed during the subsequent delivery of 225 MU of MV radiation within 45 s.

Tracking performance assessment was based on tracking deliveries with a circular MV radiation field of 5 cm diameter. Geometric tracking accuracy was determined through portal image analysis as depicted in sections 5.1.2 and 5.2.1. For MLC tracking deliveries, geometric tracking errors were quantified as RMS deviations between target and MV field centroid trajectories. The goal of HexaPOD tracking is to maintain a non-moving target position within the room coordinate system. Geometric HexaPOD tracking errors were consequently quantified as RMS deviations of residual target motion from the treatment room isocenter.

Dosimetric tracking performance was assessed through film dosimetry using radiochromic EDR2 films (Eastman Kodak, Rochester, NY). Radiation delivery was restricted to the circular MV field shape. Dosimetric tracking accuracy was quantified through a gamma-analysis, which compared a static reference dose distribution to the dose distributions of the MLC and HexaPOD tracking deliveries.

Prostate motion tracking

Tracking performance was evaluated on five prostate motion traces. The prostate motion data was acquired during daily fractions of radiotherapy prostate treatments (Schmitt et al., 2010). The length of the motion traces was at least 9 minutes. The motion traces were shifted to zero displacement at the beginning of the treatment to simulate a perfect patient setup prior to the delivery. Figure 5.11 displays two example prostate traces. Trace 2 exhibits large displacement peaks; trace 4 shows a slow prostate position drift.

Prostate motion tracking accuracy was assessed dosimetrically for the delivery of a complete five beam step-and-shoot IMRT plan. The plan was generated on a CT scan of the cylindrical prostate phantom with CTV and organ-at-risk contours for prostate and rectum. The IMRT treatment was delivered within 9 minutes in automatic DMIP mode (section 4.3.1). A single EDR2 film was inserted into the phantom, oriented parallel to the y-z-plane. Dosimetric accuracy was quantified through a gamma analysis, which compared the dose distributions of the tracking deliveries with a static reference dose distributions.

5.3.2 Results

Respiratory motion

Figure 5.12 shows geometric tracking performances for breathing traces 6 and 8. The displayed data for MLC tracking was extracted from portal imagery. The data for HexaPOD tracking was extracted from dynamic log-files of the control system. It contains the couch motion for countersteering. The displayed target motion was calculated from the difference of the couch motion and the residual target motion as reported by the Calypso system. The portal imagery for HexaPOD tracking, which was used for quantitative tracking error analysis, contains only residual target motion (*i.e.,* the difference between the displayed curves). Both tracking systems could follow the rapid target motion of breathing trace 6 accurately. Breathing trace 8 exhibited a single extremely deep breathing cycle, after which the breathing pattern changed strongly. Both tracking methods failed to adapt quickly to these irregularities.

Figure 5.13 displays geometric RMS errors of MLC and HexaPOD tracking for the 8 lung tumor motion traces. The tracking errors were quantified through portal image analysis. Tracking method 'none' refers to static radiation delivery applied to the phantom, which moved on the same trajectories as for the MLC and HexaPOD tracking deliveries. Both tracking methods could substantially improve tracking accuracies. Similar to the prediction accuracy evaluation depicted in section 2.3, the tracking accuracy depended strongly on the respective breathing trace.

Prediction errors averaged over the 8 breathing traces are listed in table 5.4. Both methods roughly halved the average geometric errors of no-tracking deliveries. The averaged geometric accuracy of MLC tracking was slightly better than for HexaPOD tracking.

Figure 5.14 displays dose distributions for MLC and HexaPOD tracking applied to breathing trace 6. Both tracking methods could strongly reduce the blurring of the no-tracking delivery. For MLC tracking, however, overdosage regions on both sides of

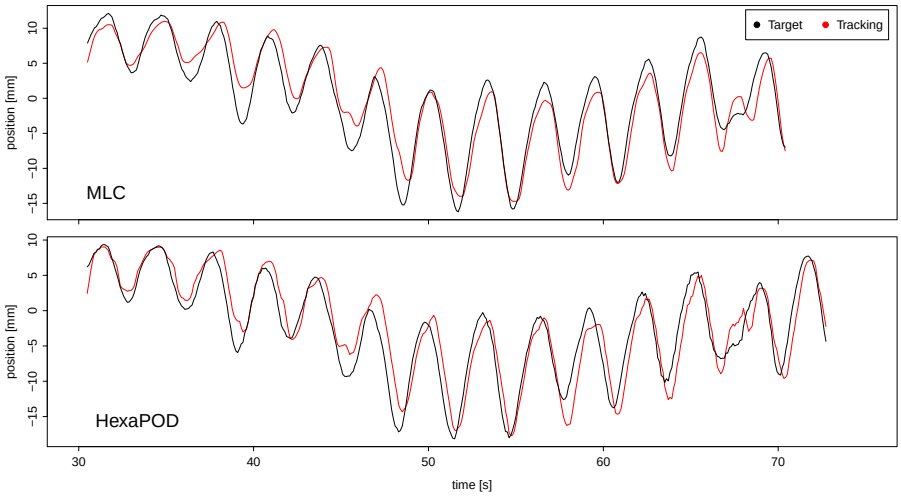

(a) Breathing trace 6

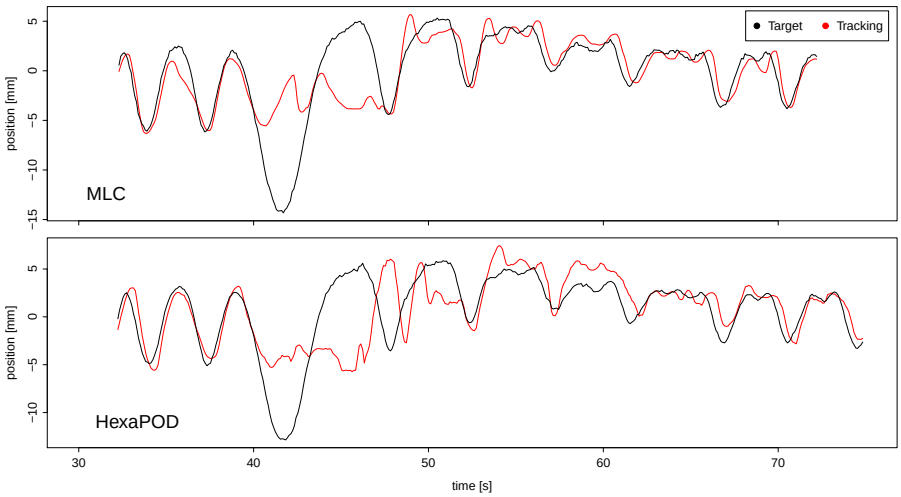

(b) Breathing trace 8

Figure 5.12: Geometric accuracy of MLC and HexaPOD tracking parallel to the leaf travel direction for breathing traces 6 and 8. MLC data from portal imagery. HexaPOD data from dynamic log-files.

Table 5.4: Geometric tracking errors averaged over 8 breathing traces. Absolute root mean squared tracking errors (RMSE) and errors normalized to no-tracking deliveries.

	Absolute RMSE [mm]		Normalized RMSE	
Tracking method	x-direction	y-direction	x-direction	y-direction
HexaPOD	0.98	2.15	0.49	0.53
MLC	0.90	2.04	0.49	0.50

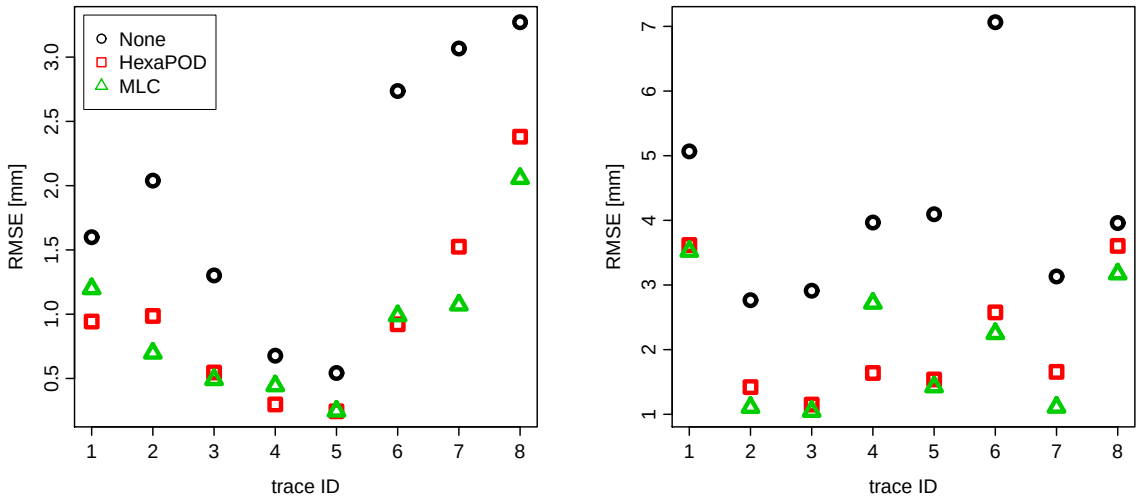

(a) x-direction (b) y-direction

Figure 5.13: Absolute root mean squared tracking errors (RMSE) for MLC and HexaPOD tracking applied to 8 breathing traces.

the field were observed. The overdosage was caused by leakage through adjacent closed leaf pairs. The dosimetric tracking accuracy analysis based on the circular field was slightly different from the analysis outlined in section 5.2.2. For the static reference delivery, all closed leaf pairs were retracted by 5 cm from the central axis. The remaining dosimetric tracking error caused by leakage through closed leaf pairs was consequently higher than the error displayed in figure 5.7.

Figure 5.15a displays the comparative dosimetric accuracy of the tracking methods for the 8 breathing traces. The HexaPOD outperformed the MLC for every breathing trace. The improvements of MLC tracking compared to no tracking were small for breathing traces 1 to 3. For traces 4 to 8, both tracking methods improved the dosimetric accuracy substantially. 2%/2mm gamma failure rates averaged over all breathing traces were 76%, 90% and 95% for no tracking, MLC tracking and HexaPOD tracking, respectively.

Figure 5.15b displays 2%/2mm gamma success rates as a function of the geometric 2D RMS tracking error. For deliveries without tracking, the dosimetric accuracy decreased strongly with the geometric tracking error. The dosimetric accuracy of the tracking deliveries was roughly constant for geometric errors below 3 mm. For higher geometric tracking errors, which only occurred for traces 1 and 8, the decrease of dosimetric accuracy followed the trend of the deliveries without tracking.

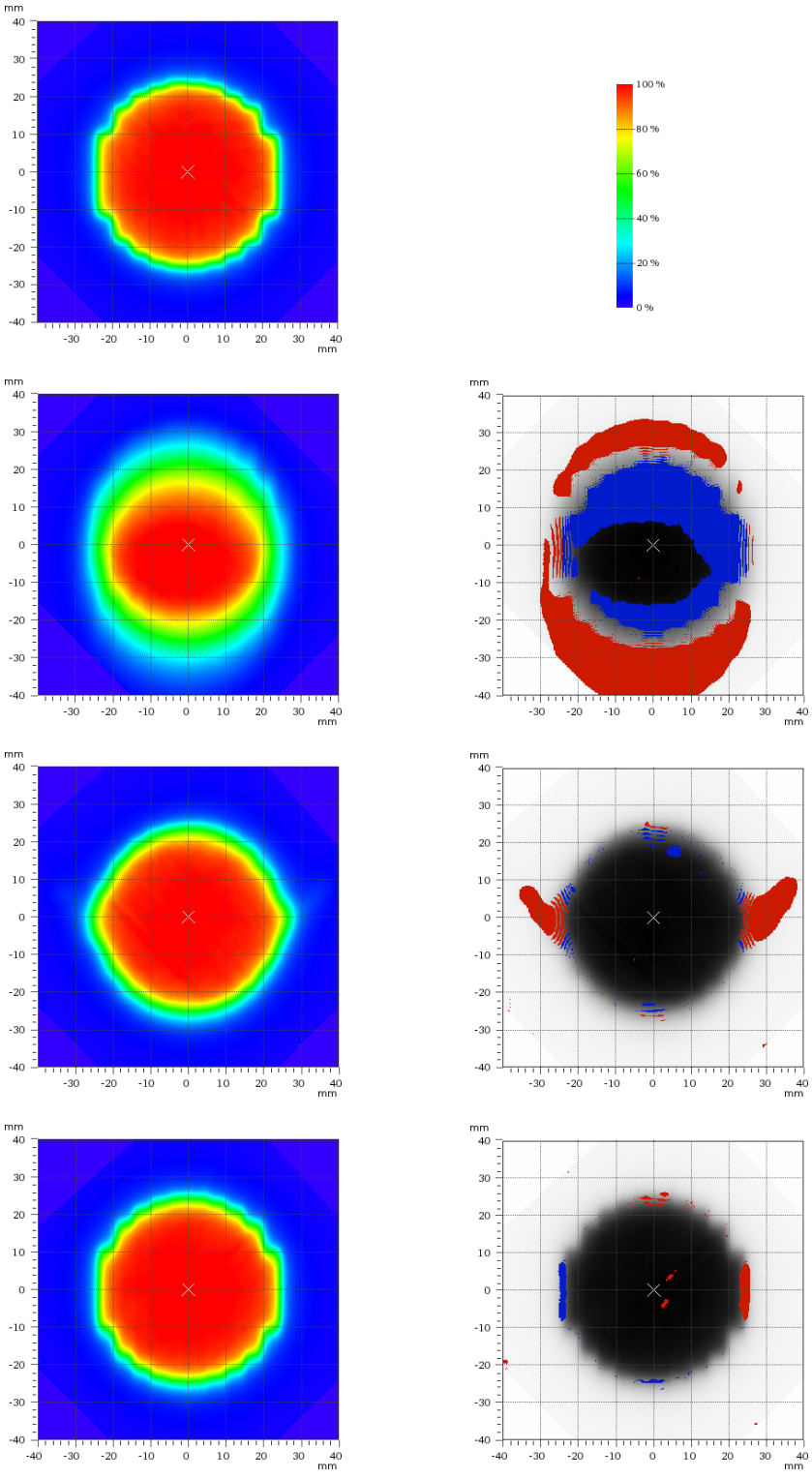

Figure 5.14: Dose distributions of the circular field applied to the target moving in two directions and gamma-test results displayed as grayscale dose distribution with gamma-indexes > 1 marked in red for overdosage and blue for underdosage. No tracking (2nd row), MLC tracking (3rd row), HexaPOD tracking (4th row).

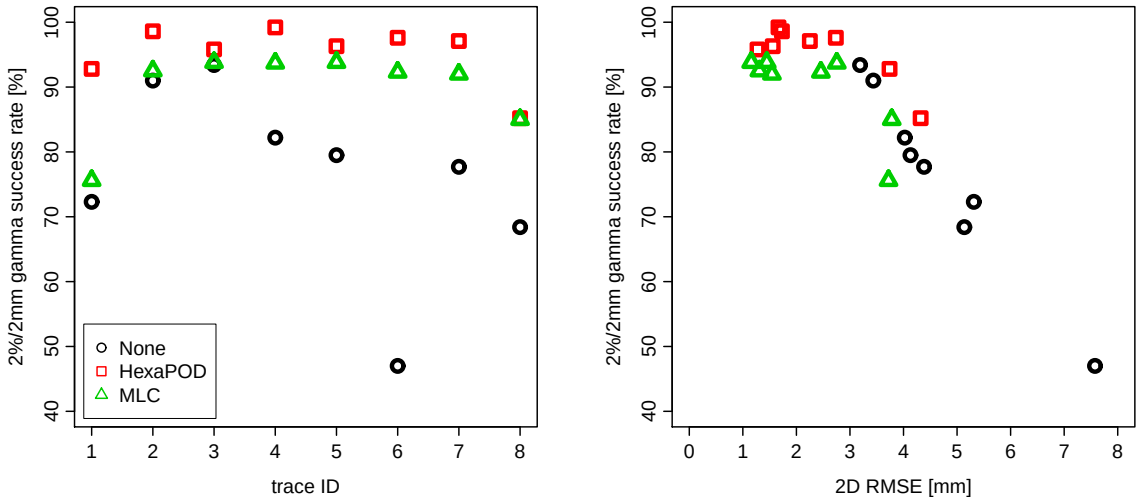

Figure 5.15: Dosimetric accuracies for lung tumor motion tracking. (a) Success rate of 2%/2mm gamma analysis for the individual breathing traces. (b) 2%/2mm gamma success rate as a function of the corresponding geometric 2D root mean squared tracking errors (RMSE).

Prostate motion

Figure 5.16 displays results of the 2%/2mm gamma analysis for prostate motion trace 2 (*i.e.*, the trace with the highest dosimetric errors for MLC tracking). The dose distribution without tracking was strongly blurred. HexaPOD tracking could almost completely recover the static dose distribution. Considerable dose errors remained with MLC tracking at the left and right borders of the high dose area. The horizontal coordinate in the displayed view is parallel to the y-axis of treatment room coordinate system. The leaf travel direction was perpendicular to the y-axis for every gantry angle. MLC tracking accuracy in this direction was limited due to hardware constraints.

Figure 5.17 displays the the dosimetric accuracy for prostate motion tracking with the MLC and the HexaPOD. Both tracking methods considerably improved dosimetric accuracies of all traces. The HexaPOD clearly outperformed the MLC for every prostate motion trace. The 2%/2mm gamma success rates for HexaPOD tracking were higher than 94% for all traces. MLC tracking improved gamma success rates of traces 1, 3 and 5 to more than 90%; traces 2 and 4 were more problematic. Gamma failure rates averaged over all prostate motion traces were 60%, 85% and 95% for no tracking, MLC tracking and HexaPOD tracking, respectively.

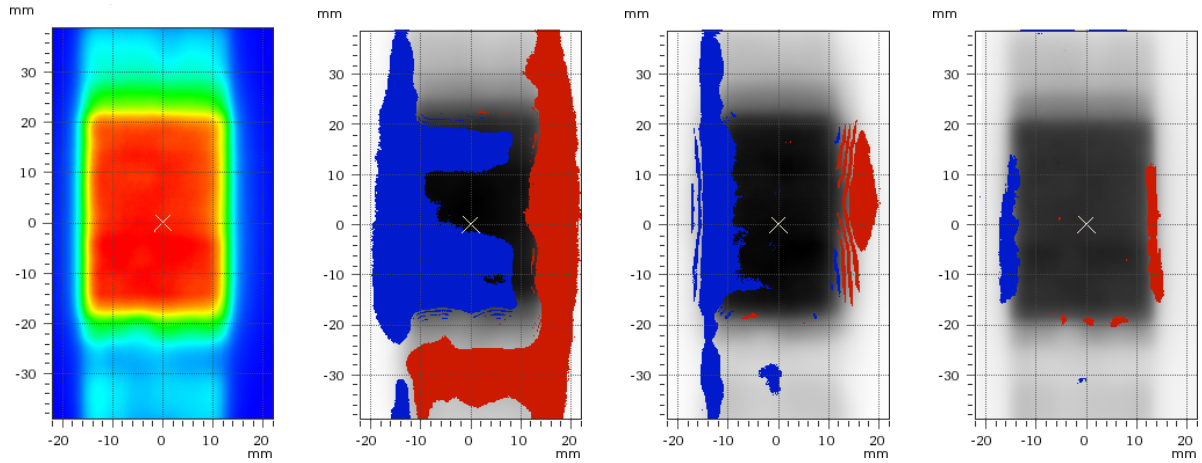

(a) static reference (b) no tracking (c) MLC tracking (d) HexaPOD tracking

Figure 5.16: (a) Static reference dose distributions of the prostate IMRT plan. (b-d) Gamma test results for prostate motion trace 2.

5.3.3 Discussion

We have compared the performances of tracking systems based on the adaption of the treatment beam with a dynamic MLC and on repositioning of the entire patient with a robotic treatment couch. Both tracking systems received continuous target position updates from the Calypso System and used the same motion data for the experiments. Tracking performance was assessed for 8 lung tumor and 5 prostate motion traces.

The evaluation of geometric tracking accuracies showed almost equal performances of the tracking systems. Both systems roughly halved the geometric errors of deliveries without tracking. The geometric accuracy of MLC tracking was slightly better than for HexaPOD tracking.

For MLC tracking, the remaining errors were predominantly caused by prediction errors. The dynamic MTCS log-files of the geometric tracking accuracy measurements contain target positions as reported by the Calypso System as well as forward predictions of the target positions. Prediction errors can therefore be calculated from the log-files. The RMS prediction errors averaged over the 8 breathing traces were 0.85 mm in x-direction and 1.97 mm in y-direction; this corresponds to 95% and 96% of the respective geometric tracking errors listed in table 5.4.

The remaining errors of HexaPOD tracking also seem to be caused by the tracking control system and not by couch travel speed or acceleration limitations: The highest tracking errors do not occur on breathing trace 6 with the fastest and largest target motion, but on breathing traces 1 and 8, which exhibit sudden changes in the breathing pattern.

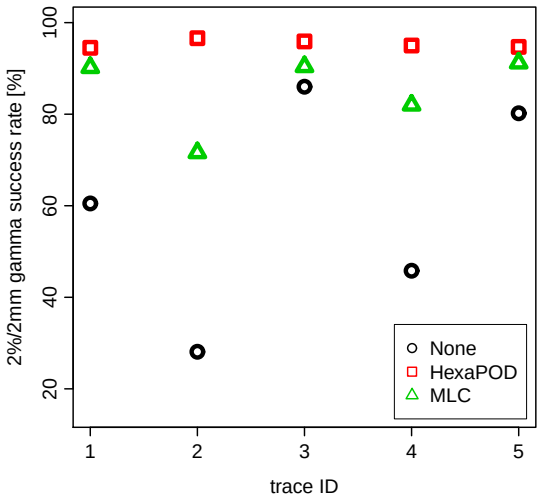

Figure 5.17: Dosimetric accuracy for prostate motion tracking. Success rate of 2%/2mm gamma analysis for the individual prostate motion traces.

In spite of the slightly better geometric accuracy of MLC tracking, the HexaPOD tracking yielded clearly better dosimetric accuracies. We observed that 2%/2mm gamma success rates of both tracking devices were roughly constant if 2D geometric tracking errors were below 3 mm (figure 5.15b). This constant level was at around 97% for HexaPOD tracking and at around 93% for MLC tracking. Dosimetric accuracy for MLC tracking consequently seems to be limited to this value due the issues raised in section 4.2.1: the leaf width of 5 mm as well as leakage through closed leaf pairs, which have to be positioned adjacent to open leaf pairs to be able to quickly open in case of target motion perpendicular to the leaf travel direction.

The HexaPOD outperformed the MLC even more clearly for the dosimetric tracking accuracy evaluation with prostate motion traces. Prostate motion typically exhibits slow drifts over the entire course of a radiotherapy fraction. Roughly constant target position offsets of several millimeters are often observed during the delivery of individual IMRT segments or even entire beams. Tracking errors due to the finite leaf width can not average out and are therefore more pronounced than for lung tumor tracking.

The presented tracking performance measurements did not account for the following concerns associated with robotic couch tracking applied to rapid respiratory motion: Firstly, patient comfort might be compromised. Secondly, couch motion might be different from organ motion due to patient anatomy deformation in response to the couch acceleration. Wilbert et al. (2010) reported that couch tracking of respiratory motion was tolerated well by a group of patients and volunteers. They also observed no significant changes within the breathing patterns during couch tracking. To our knowledge, the acceleration induced patient anatomy deformation has not yet been investigated.

5.3.4 Conclusion

The performance comparison of MLC and HexaPOD tracking showed a superior dosimetric tracking accuracy for HexaPOD tracking. The geometric tracking accuracy was almost equal for both systems with slight advantages of MLC tracking. Both systems yielded substantially improved dosimetric accuracies compared to the no-tracking deliveries. The dosimetric disadvantage of MLC tracking is caused by to the hardware limitations of MLC tracking – namely the leaf width of 5 mm and leakage through the tips of closed leaf pairs. There are concerns associated with rapid patient motion induced by couch tracking of respiratory motion; MLC tracking might therefore be the preferred method for respiratory motion tracking in spite of the slightly inferior dosimetric accuracy. For slow prostate motion compensation, HexaPOD tracking is clearly favorable.

5.4 MLC tracking applied to dynamic IMRT deliveries

The MTCS supports rotational and dynamic IMRT (D-IMRT) deliveries in addition to conformal RT and step-and-shoot IMRT (S-IMRT) – the radiotherapy delivery modes, which are clinically approved with the ARTISTE radiotherapy suite. In the following, we compare the dosimetric accuracies of MLC tracking applied to D-IMRT and S-IMRT deliveries.[3] The dosimetric accuracy measurements were based on a single, highly modulated beam out of a S-IMRT treatment plan. The D-IMRT deliveries were based on four different leaf sequence calculation methods.

5.4.1 Materials and methods

Leaf sequencing

Intensity modulation of D-IMRT deliveries is achieved by continuous leaf motion during radiation delivery. An arbitrary intensity profile along the leaf travel direction $I(x)$ can be generated by multiple (in fact, infinitely many) leaf sequences. Stein et al. (1994) proposed a method to calculate D-IMRT leaf sequences, which minimize the treatment time based on the following equations:

$$\begin{aligned} v_l(x) &= v_{max} & v_t(x) &= \frac{v_{max}}{1 + I'(x)\, v_{max}} & &, \text{for } I'(x) \geq 0 \\ v_l(x) &= \frac{v_{max}}{1 - I'(x)\, v_{max}} & v_t(x) &= v_{max} & &, \text{for } I'(x) < 0\,. \end{aligned} \tag{5.2}$$

The equations determine the leaf velocities $v_l(x)$ and $v_t(x)$ of leading and trailing leaves for each position x within the interval $[x_1, x_2]$. $I'(x)$ denotes the derivative of $I(x)$ along the x-coordinate and v_{max} denotes the maximum physically achievable leaf velocity. The corresponding leaf trajectories $s_l(x)$ and $s_t(x)$ are calculated through integration with $v_l(x_1) = v_t(x_1) = 0$.

The leaf sequences defined through (5.2) are valid only for an ideal MLC with zero penumbra. Our leaf sequence calculations were therefore based on an algorithm proposed also by Stein et al. (1994), which takes penumbra into account. The algorithm iterative modifies the leaf sequences obtained through (5.2) to generate the desired intensity profile $I(x)$ given a measured penumbra function.

A 2D intensity map can be generated by applying the outlined method to each leaf pair independently. This will, however, lead to underdosage effects due to the tongue-and-groove design of the MLC (Tacke et al., 2008). We have therefore implemented an

[3] Measurements and initial data evaluation performed by K. Hofmann

algorithm proposed by Rangaraj and Papiez (2005), which eliminates the tongue-and-groove effect through synchronization of trajectories of adjacent leaf pairs. Depending on the level of modulation of the 2D intensity map, the synchronization algorithm can increase the delivery time considerably.

For MLC tracking applied to D-IMRT deliveries, the leaf motion for intensity modulation is superimposed with the leaf motion for target tracking. The maximal leaf velocity v_{max} for initial leaf sequence calculation according to (5.2) should consequently be set to smaller values than the maximal physically achievable leaf velocity (43 mm/s for the 160 MLC).

To investigate the influence of leaf trajectory synchronization as well as the influence of v_{max} on the tracking accuracy, our study included the following four leaf sequence calculation methods:[4]

1. non-synchronized with $v_{max} = 36$ mm/s,
2. non-synchronized with $v_{max} = 25$ mm/s,
3. synchronized with $v_{max} = 36$ mm/s,
4. synchronized with $v_{max} = 25$ mm/s.

Experimental methodology

The experimental setup was the same as introduced in section 5.1. We used two target motion patterns: a regular 2D $\sin^4$ trajectory with amplitudes of 10 mm and 20 mm in x and y-directions and a period of 4 s, and a 3D respiratory motion trace from the data set described in section 2.2.1. Geometric tracking accuracy was determined with a circular MV radiation field as outlined in section 5.1.2. Dosimetric tracking accuracy measurement was based on Gafchromic EBT and EBT2 films (International Specialty Products, Wayne, NJ). EBT films were used for the experiments with irregular breathing motion and EBT2 films for the regular $\sin^4$ motion. Dose distributions for all tracking deliveries were compared to the dose distribution of a static S-IMRT delivery using the 2%/2mm gamma criterion.

5.4.2 Results

Figure 5.18 displays the result of the geometric tracking accuracy evaluation with a circular MV radiation field for the breathing motion trace. The RMS tracking error was

[4]Leaf sequence calculations performed by K. Hofmann

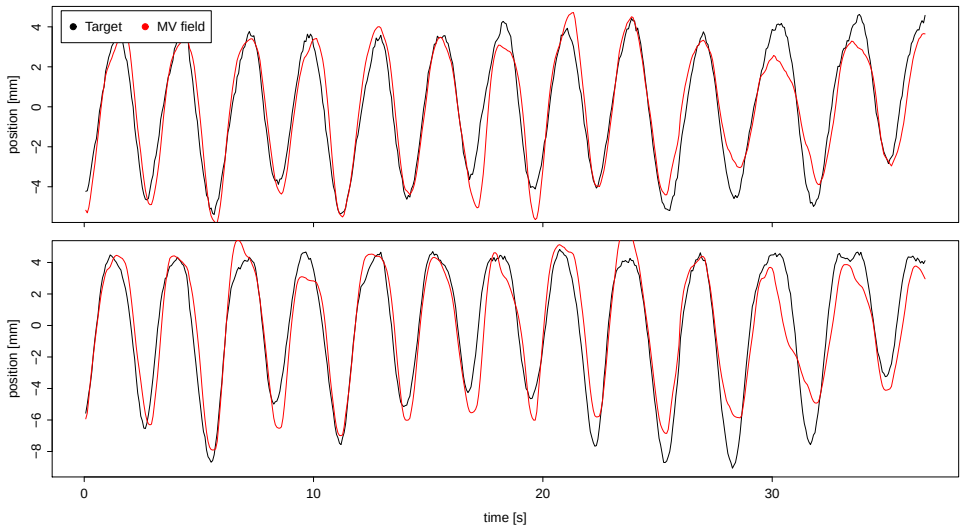

Figure 5.18: Geometric tracking accuracy in direction perpendicular (upper panel) and parallel (lower panel) to the leaf travel direction for the patient breathing trace.

0.99 mm in x-direction and 1.51 mm in y-direction. For the $\sin^4$ motion trace, geometric tracking errors were 0.40 mm in x-direction and 0.67 mm in y-direction.

Figure 5.19 displays results of the 2%/2mm gamma analysis for respiratory motion tracking. The IMRT field exhibited large dose gradients at the borders of, but also within the field (figure 5.19a). In the displayed view, the leaves travel in horizontal direction to modulate the D-IMRT dose distributions. For both S-IMRT and D-IMRT, the tracking deliveries yielded substantially reduced gamma failure rates. In contrast to previously displayed gamma analysis results – for example in figures 5.7 and 5.8 – we observed pixels failing the 2%/2mm gamma criterion not only at the border of, but also within the high dose area of the field.

Table 5.5 summarizes the results of the dosimetric accuracy analysis for the regular $\sin^4$ motion and the irregular respiratory motion traces. In both cases, tracking increased the dosimetric accuracy substantially. 2%/2mm gamma failure rates for tracking applied to S-IMRT were smaller than those for D-IMRT.

5.4.3 Discussion

As pointed out in sections 5.2.3 and 5.3.3, the main contributions to the remaining dosimetric errors of MLC tracking are: Firstly, geometric uncertainties due to respiratory motion forward prediction errors. Secondly, hardware limitations, such as the leaf width of 5 mm, the limited maximal leaf velocity and leakage through closed leaf pairs.

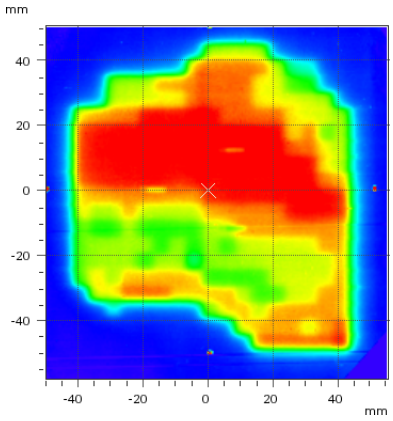

(a) static reference

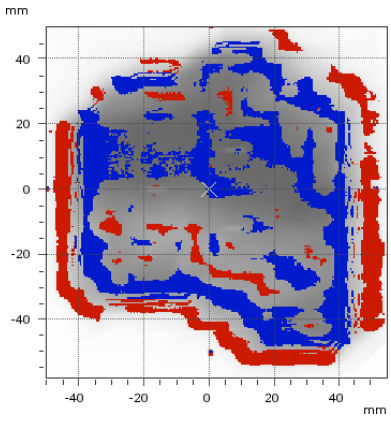

(b) S-IMRT, without tracking

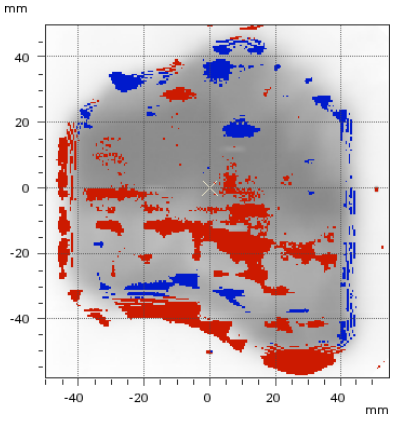

(c) S-IMRT, with tracking

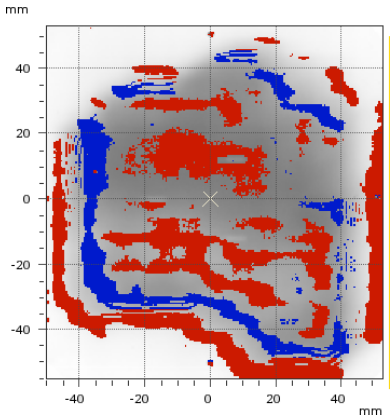

(d) D-IMRT, without tracking

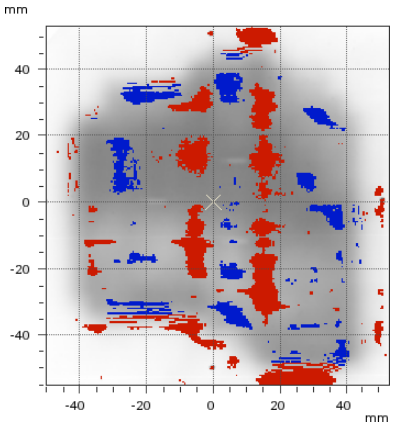

(e) D-IMRT, with tracking

Figure 5.19: Dosimetric accuracy for breathing motion tracking. (a) Static reference dose distribution. (b-e) 2%/2mm gamma-test results displayed as grayscale dose distribution with gamma-indexes >1 marked in red for overdosage and blue for underdosage. (b, c) S-IMRT delivery. (d, e) Synchronized D-IMRT delivery with $v_{max} = 36$ mm/s.

Table 5.5: Dosimetric tracking accuracy for $\sin^4$ and breathing motion traces. Displayed are percentage 2%/2mm gamma failure rates.

	$\sin^4$ motion		Breathing motion	
Delivery mode	w/o	w/	w/o	w/
D-IMRT / non-sync / 36	44.6	22.6	41.8	22.0
D-IMRT / non-sync / 25	44.6	23.5	35.3	22.1
D-IMRT / sync / 36	51.8	20.0	37.6	23.9
D-IMRT / sync / 25	37.6	20.8	39.4	22.8
S-IMRT	42.9	13.7	35.5	16.7

'w/' and 'w/o' refer to deliveries with and without tracking applied.
'D-IMRT / non-sync / 36' refers to non-synchronized D-IMRT delivery with $v_{max} = 36$ mm/s.

The results displayed in table 5.5 demonstrate that the relative importance of geometric uncertainties and hardware limitations depends on the D-IMRT delivery mode. The non-synchronized deliveries exhibit complex field shapes with large distances between adjacent leaf tips. The field shapes of synchronized deliveries are generally smaller, more compact and adjacent leaf tips are closely aligned. The influence of hardware limitations is consequently more pronounced for non-synchronized deliveries. Geometric uncertainties induce dosimetric errors at the borders of the radiation field. Their influence is accordingly more pronounced for synchronized deliveries.

For $\sin^4$ motion tracking, geometric uncertainties played no role. The tracking accuracies of the synchronized deliveries were better than for non-synchronized deliveries. For respiratory motion tracking, in contrast, the geometric uncertainties dominated the tracking performance. The non-synchronized deliveries were more accurate than the synchronized deliveries.

The $\sin^4$ motion had larger amplitudes than the respiratory motion; the influence of hardware limitations was consequently more pronounced than for respiratory motion tracking. For non-synchronized deliveries, the hardware limitations were obviously more important than the geometric uncertainties. Tracking of the more rapid regular motion yielded worse dosimetric tracking accuracies in spite of the better geometric accuracy.

The differences between the deliveries with maximum leaf velocity $v_{max} = 36$ mm/s and $v_{max} = 25$ mm/s were small. The dosimetric accuracy measurement were based on EBT and EBT2 films, which are optimized for complete radiotherapy fraction doses. The noise level of the measured single-beam doses is consequently relatively large. We therefore consider the observed differences between 36 mm/s and 25 mm/s as not significant.

6 MLC tracking based on kilovoltage x-ray imagery

The research ARTISTE radiotherapy suite installed at our institution features the KVision on-board kilovoltage (kV) x-ray imaging system introduced in section 4.1.1. We have recently developed a novel intra-fractional target motion monitoring system based on the KVision system (Fast et al., 2011a) as outlined in section 3.1.2. The imaging system can be operated either continuously with a maximum update rate of 7.1 Hz or on demand. In the following we present the results of MLC tracking based solely on continuous x-ray imaging (section 6.1). In section 6.2, we report on MLC tracking based on a combined external surrogate motion and internal x-ray based target motion monitoring system. The results of sections 6.1 and 6.2 are jointly discussed in section 6.3.

6.1 MLC tracking based solely on x-ray imagery

6.1.1 Materials and methods

Experimental setup

Figure 6.1 shows the experimental setup for MLC tracking based on x-ray imaging in the in-line geometry. In addition to the on-board megavoltage (MV) flat panel detector (FPD), we have equipped the linac with a second FPD directly underneath the linac head. The kV x-ray source of the KVision system is mounted such that the kV beam points towards the linac head. We tilted the kV beam intentionally by 5.4° from the MV beam axis so that the two beams were spatially separated on both FPDs. A simple phantom consisting of stacked solid water slices was mounted on the 4D motion stage introduced in section 5.1.1. The phantom had a radioopaque marker embedded, whose position was detected with the x-ray imaging system at a frame-rate of 7.1 Hz. Target positions were reported to the MTCS through Ethernet connection.

The lower FPD displayed in figure 6.1 was used to monitor the MV beam and the marker of the phantom continuously during the tracking experiments. The images recorded

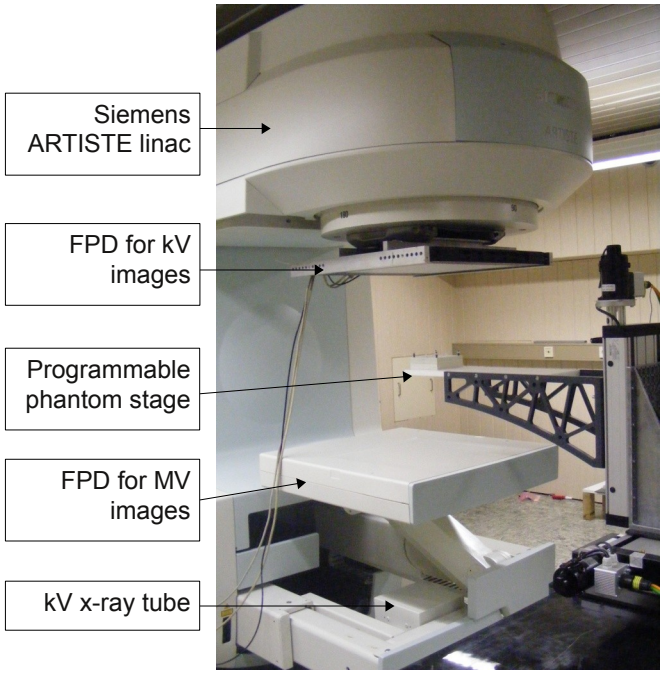

Figure 6.1: Experimental setup. The kV an MV beams pass through both flat panel detectors (FPD). The 4D motion stage moves on patient breathing traces. Target motion is detected with the upper FPD. The lower FPD is used for geometric accuracy assessment.

with the MV FPD were used for geometric tracking accuracy assessment and latency measurements. Obviously, both the kV imaging and the MV treatment beams passed through both FPDs.

Analysis of MV portal images

Latency and geometric tracking accuracy were assessed through an analysis of portal images based on the image analysis algorithm outlined in section 5.1.2. MV portal images were therefore acquired at a frame-rate of 10 Hz during the experiments. As a result of the in-line imaging geometry, both the MV treatment beam and the kV imaging beam were visible on both FPDs. Separation of MV and kV signals detected with the upper kV FPD for intra-fractional motion monitoring was outlined in section 3.1.2. Example images acquired with the lower MV FPD are displayed in figure 6.2. Because MV FPD readout and kV imaging pulses were not synchronized, the shape of the kV field alters from frame to frame.

To extract MV field and radioopaque marker centroids from the images with the previously described algorithm (section 5.1.2), the kV imaging field was subtracted from the mixed kV/MV images. The individual steps of the subtraction algorithm are displayed in figure 6.3. An image containing kV-only information (c) was constructed from the frame

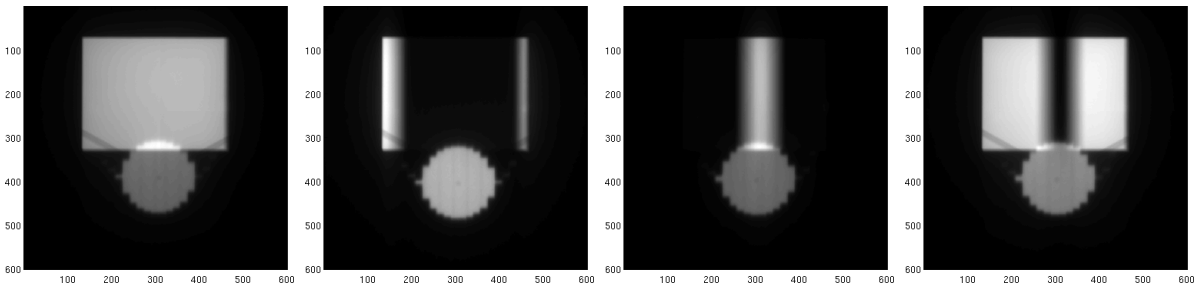

Figure 6.2: Example images acquired with the MV FPD during tracking experiments. The circular MV treatment field is overlaid with the rectangular kV imaging field.

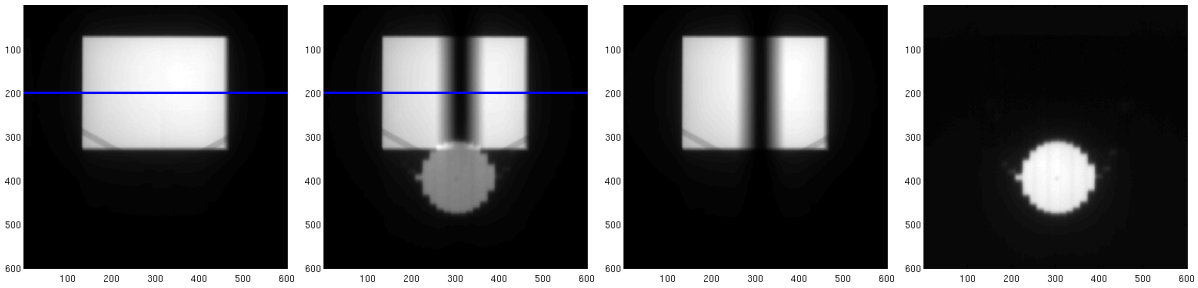

(a) (b) (c) (d)

Figure 6.3: Illustration of steps for subtraction of kV signals from MV imagery. (a) kV-only template frame, (b) frame to be analyzed, (c) calculated kV-only frame, (d) calculated MV-only frame

to be analyzed (b) using a kV-only template frame (a). Therefore, horizontal profiles of frames (a) and (b) at pixel position 200 were calculated (indicated by the blue lines). The horizontal profile of (b) is divided by the profile of (a). Finally, each vertical profile of the template frame (a) is multiplied with the corresponding entry of the division of profiles to generate the kV-only frame (c). MV-only images (d) are then calculated by subtracting the kV-only image (c) from the frame to be analyzed (b).

Geometric tracking accuracy

Geometric tracking accuracy was quantified by calculating RMS deviations between phantom motion and circular MV field motion extracted from the portal imagery. Three breathing traces from the previously described data set (section 2.2.1) were used. Target motion forward prediction was performed with a support vector regression predictor (section 2.2.3). Predictor training was based on the adaptive-expansive training scheme (section 2.2.4) with a training window expanding from 30 s to 67 s. The influence of forward prediction on the geometric tracking accuracy was assessed through an analysis of dynamic log-files of the MTCS.

Table 6.1: Geometric tracking accuracy for three breathing traces.

	Absolute RMSE [mm]		Normalized RMSE	
Breathing trace	x	y	x	y
1	0.52	1.22	0.40	0.43
2	0.23	1.62	0.40	0.40
3	0.91	2.49	0.36	0.38

6.1.2 Results

Latency

The total system latency was measured as described in section 5.1.2. Sinusoidal target motion was tracked without target motion prediction. The resulting lag time was quantified as the phase difference between sine-function fits to the target and the MV field motion as extracted from the portal imagery. Four measurements yielded a total tracking system latency of (618 ± 6) ms.

The kV imaging system reported target position packages together with a time-stamp of position detection to the MTCS. The average latency value of the kV imaging system was (82 ± 1) ms. Given the position update rate of imaging system of 7.1 Hz, the effective motion monitoring latency according to equation (5.1) amounts to (152 ± 1) ms. In section 5.1.3, values for the MLC latency and MTCS computation times of (473 ± 10) ms and (1.4 ± 0.7) ms were obtained. The accordingly expected total system latency of (626 ± 10) ms is in accordance with the measurement.

Geometric tracking accuracy

Table 6.1 lists the results of the geometric tracking accuracy analysis based on MV portal imagery for the three breathing motion traces. Tracking errors in x-direction (perpendicular to leaf travel direction) were below 1 mm. In y-direction (parallel to leaf travel direction), higher absolute tracking errors up to 2.5 mm were observed. The increased errors in y-direction were due to the larger breathing motion amplitudes. The normalized tracking errors for both the x- and y-direction approximately amounted to 0.4, which corresponded to a 60% improvement compared to the no tracking deliveries.

Figure 6.4 displays the results of the log-file based prediction errors analysis. Predicted positions in y-direction are shown together with the target motion and the circular MV field centroid motion. The MV field closely followed the predicted positions. Minor deviations were observed at the turning points of the predicted trajectory. The noise level

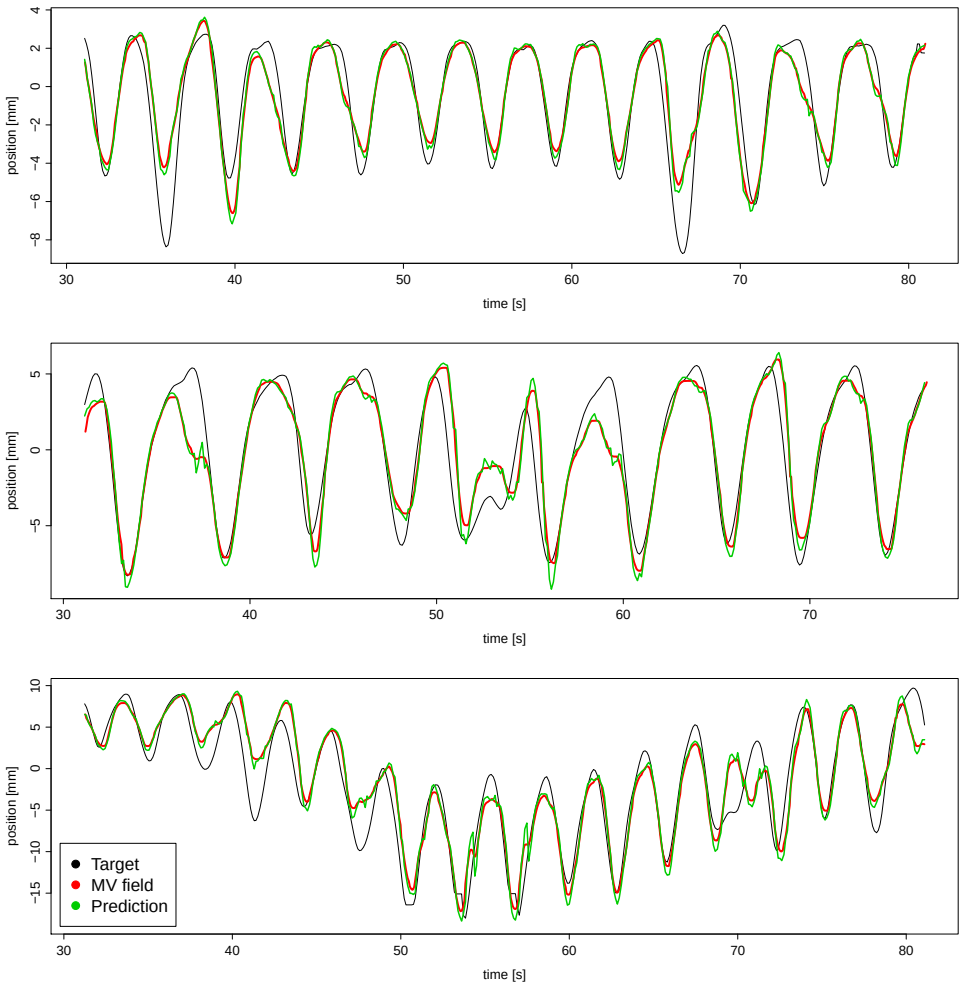

Figure 6.4: Influence of target motion forward prediction on geometric tracking accuracy for breathing traces 1 (upper panel) to 3 (lower panel). Trajectories parallel to leaf travel direction of target motion (black), MV field motion (red) and predicted positions (green) are extracted from the dynamic MTCS log-files.

of the predicted trajectories was smoothed by the MV field. Consequently, the remaining geometric tracking errors observed at irregularities of target motion were predominantly caused by prediction errors.

6.2 MLC tracking based on combined external surrogate and x-ray motion monitoring

In the previous section, we have demonstrated highly accurate MLC tracking based on a single kV x-ray imager in in-line geometry. The obvious disadvantage of the system is the additional dose of ionizing radiation due to x-ray imaging. With the maximum image acquisition frequency of 7.1 Hz, the average imaging dose would reach 1 Gy after approximately 22 minutes (Fast et al., 2011a).

The rationale for combined external surrogate and internal x-ray motion monitoring is to substantially reduce imaging dose. A correlation model between external and internal motion is established based on sparse internal motion data as outlined in section 3.2. The real-time part of the MLC tracking procedure (*i.e.,* the tracking loop depicted in section 4.3.2) then relies solely on the continuously monitored external motion signal. Consequently, the number of x-ray acquisitions during a tracking delivery can be drastically reduced.

Besides the dose saving through less x-ray acquisitions, combined external and internal x-ray motion monitoring offers two further advantages: Firstly, the total system latency can be reduced. External motion monitoring – for example with the infrared marker detection or the pressure belt systems depicted in section 3.2.1 – can be performed with considerably shorter latencies and higher update rates as x-ray imaging. Secondly, intra-fractional x-ray imaging can be performed while the treatment beam is turned off, for example in between the delivery of individual beams or segments of a radiotherapy treatment. This generally yields either increased image quality given the same imaging dose per x-ray pulse, or the same image quality with a lower imaging dose per x-ray pulse. The decreased image quality of synchronous x-ray imaging and MV radiation delivery in the in-line geometry is obviously due to the detection of both beams with the FPD for imaging. For orthogonal imaging geometries, image quality is compromised by scattered MV radiation.

The disadvantage of combined external and internal motion monitoring is the additional complexity; two monitoring devices have to be operated and two motion data streams have to be managed by the tracking system. Additionally, the estimation of internal target positions with the correlation model introduces further geometric uncertainties.

6.2.1 Materials and methods

Experimental setup

The experimental setup was similar to the previously described setup for MLC tracking based solely on x-ray imagery (section 6.1.1). The tracking performance assessment was based on the same three respiratory motion traces. The breathing data consisted of simultaneously measured internal 3D lung tumor motion and external chestwall displacement (section 3.3.1). The internal motion component with the largest and second largest amplitude was put on the y- and x-axes of the 4D motion stage, respectively. The external surrogate motion was put on the z-axis. Due to the in-line imaging geometry, the kV imaging system can only detect motion components parallel to the xy-plane. It consequently detected the beam's eye view of the internal target motion and was blind for the external motion. The external surrogate motion was measured with a linear potentiometer, which was fixed to the z-axis of the motion stage. An analog-to-digital (AD) converter reported potentiometer voltages to the MTCS at a frame-rate of 30 Hz.

Latency

The real-time part of the MLC tracking procedure is based on the external motion signal. The total system latency accordingly equals the latency of the MLC tracking system with potentiometer based motion monitoring. Total system latency was measured by moving the phantom on a sinusoidal trajectory in y- and z-direction simultaneously. The z-motion detected with the potentiometer was reported to the MTCS as internal y-motion. The motion monitored with the potentiometer was tracked in y-direction with a circular MV field without target motion forward prediction. The time lag between target and MV field motion was quantified through portal image analysis as outlined in section 5.1.2.

In addition to the total system latency measurements, the latency of the AD readout system for the potentiometer (in the following referred to as 'AD latency') was analyzed. The phantom was moved again on the simultaneous sinusoidal trajectories in y- and z-direction. Target motion was monitored with both the x-ray system and the potentiometer. The latency of the x-ray imaging system is known (section 6.1.2). The AD latency can consequently be calculated from the time shift of the target trajectories measured with the two monitoring systems.

Prediction and correlation model setup

Both the tracking and the verification loop of the MTCS relied on internal target position estimations of the correlation model based on the external surrogate motion signal. The training data set of the correlation model for internal target motion coordinate k consisted of pairs $(\boldsymbol{x}_j, y_j^k)$ of input vectors and target scalars (section 3.3.1). We selected the support vector regression based correlation model, which performed favorably in the comparison study presented in section 3.3.2. According to the results of the model parameter optimization procedure, we selected an input vector dimensionality of $p = 3$ and a spacing between input vector entries of $\delta = 0.8$ s. For each internal x-ray target position observations $\boldsymbol{s}_{int} = (s_{int}^1, s_{int}^2, s_{int}^3)$ within the training data set, input vectors and target scalars were constructed as:

$$\begin{aligned} \boldsymbol{x}_j &= (\ s_{ext}(t_{j-2\delta})\ ,\ s_{ext}(t_{j-\delta})\ ,\ s_{ext}(t_j)\ ) \\ y_j^k &= s_{int}^k(t_j)\ , \end{aligned} \tag{6.1}$$

for point in time t_j and external position observations s_{ext}.

In order to compensate for the total system latency τ_{total}, the MLC shape calculations within the tracking loop at time t were based on the estimated internal target positions at future point in time $t+\tau_{mlc}$. The estimation of future internal target positions $\hat{\boldsymbol{s}}_{int}(t+\tau_{mlc})$ required a combination of external motion forward prediction and the external/internal correlation model. The corresponding correlation model input vector was then given by the predicted external position $\hat{s}_{ext}(t + \tau_{mlc})$ and two previously detected external positions according to (6.1).

The external motion forward prediction was based on support vector regression (section 2.2.3). The predictor was continuously retrained during the tracking experiments using the adaptive-expansive training mode (section 2.2.4). The training window was expanded from 30 s to 67 s.

Step-and-shoot IMRT delivery

Tracking accuracy assessment was based on a single, highly modulated beam out of a step-and-shoot IMRT treatment plan. The highly modulated field consisting of ten segments has already been used for the dynamic IMRT tracking accuracy assessment outlined in section 5.4. The tracking delivery was performed completely automatic using the DMIP delivery mode (section 4.3.1). The delivery time for the total of 180 MU was approximately 85 s.

The first 30 s of the tracking experiments were reserved for external/internal correlation model setup and predictor training. For the initial correlation model setup, internal target motion was detected with 40 x-ray images acquired at a frame-rate of 2 Hz within

seconds 10 to 30 of the tracking experiments. The correlation model was trained directly after receipt of the 40^{th} x-ray image. After successful initial predictor and correlation model training, the MTCS started the delivery of the first segment. During the adjustment of a new segment, the acquisition of five x-ray images at a frame-rate of 2 Hz was triggered. These five new internal motion measurements were used to update the correlation model based on the adaptive retraining scheme (section 3.3.1). After the correlation model was re-established, the next segment was delivered.

Analysis of prediction and correlation model errors

The accuracies of external motion forward prediction and the external/internal correlation model were determined through an analysis of dynamic log-files. For combined external and internal motion monitoring, the MTCS does not monitor internal target motion continuously. The internal motion information was therefore extracted from the log-files of the 4D motion stage.

The log-files of the MTCS and the 4D motion stage are created by different programs on different computers. Both programs continuously log the z-motion (*i.e.,* the external surrogate motion) of the phantom, which allowed the synchronization of the time-axes of the two programs.

External motion forward prediction errors were quantified as RMS deviations between actual z-motion extracted from 4D motion stage log-files and the prediction values extracted from MTCS log-files. The correlation model estimates internal target positions based on the forward prediction of external position and past external position observations. The correlation model error therefore depends on the forward prediction model error. The accordingly combined correlation and prediction error was quantified as RMS deviations between actual x- and y-motion extracted from 4D motion stage log-files and the correlation model predictions extracted from MTCS log-files. Absolute prediction and correlation model errors as well as errors normalized with the standard deviation of the corresponding breathing trajectories were calculated.

Dosimetric tracking accuracy

Dosimetric tracking accuracy assessment was based on EDR2 films (Eastman Kodak, Rochester, NY). A static radiation delivery to the non-moving phantom provided a reference dose distribution. Dose distributions of the tracking deliveries and of deliveries with a moving phantom but without tracking were compared to the static reference dose distribution in terms of the 2%/2mm gamma criterion.

6.2.2 Results

Latency

Three measurements based on portal image analysis of target motion and circular MV field motion yielded a total system latency of (507 ± 14) ms.

We have additionally performed a MTCS log-file analysis for a delivery with simultaneously measured external motion as detected with the potentiometer and internal motion as detected with the x-ray system. The time shift of the target trajectories measured with the two system yielded an AD latency of (23 ± 2) ms. Using the results of the latency contributor analysis of section 5.1.3, the expected total system latency amounts (513 ± 10) ms, which is in accordance to the measured value.

Accuracies of prediction and correlation models

Normalized external motion forward prediction errors – as extracted from the dynamic MTCS and 4D motion stage log-files of the step-and-shoot IMRT deliveries – amounted to 0.31, 0.29 and 0.23 for breathing traces 1, 2 and 3, respectively. As the magnitude of the external motion has no influence on the tracking accuracy, we did not evaluate absolute external motion prediction errors. The normalized prediction errors are smaller than the normalized geometric tracking errors of the same breathing traces of approximately 0.4 shown previously for MLC tracking based solely on x-ray imagery.

Figure 6.5 displays the results of the log-file analysis for combined prediction and correlation model errors of the step-and-shoot IMRT tracking deliveries. Target motion trajectories from the 4D motion stage log-files are available throughout the delivery. The predictions of the correlation model are available only during the deliveries of the ten segments. X-ray images were acquired only prior to the delivery or in between the delivery of the ten segments. For breathing traces 1 and 2, the predicted values of the correlation model followed the actual target motion accurately. For the x-direction of breathing trace 3, in contrast, the correlation model predictions showed substantial deviations from the target trajectory. The correlation model completely failed to predict the baseline shifts observed in segments 1 to 3.

Table 6.2 lists the combined RMS prediction and correlation model errors of the step-and-shoot IMRT deliveries. The combined prediction and correlation model errors were considerably larger than the aforementioned prediction error alone for trace 2 and the x-coordinate of trace 3. In these cases, the correlation model contributed substantially to the overall prediction error, which was consequently higher than the previously reported respective geometric tracking accuracies of the x-ray only system (table 6.1). For breathing trace 1 and the y-coordinates of trace 3, the correlation model error played

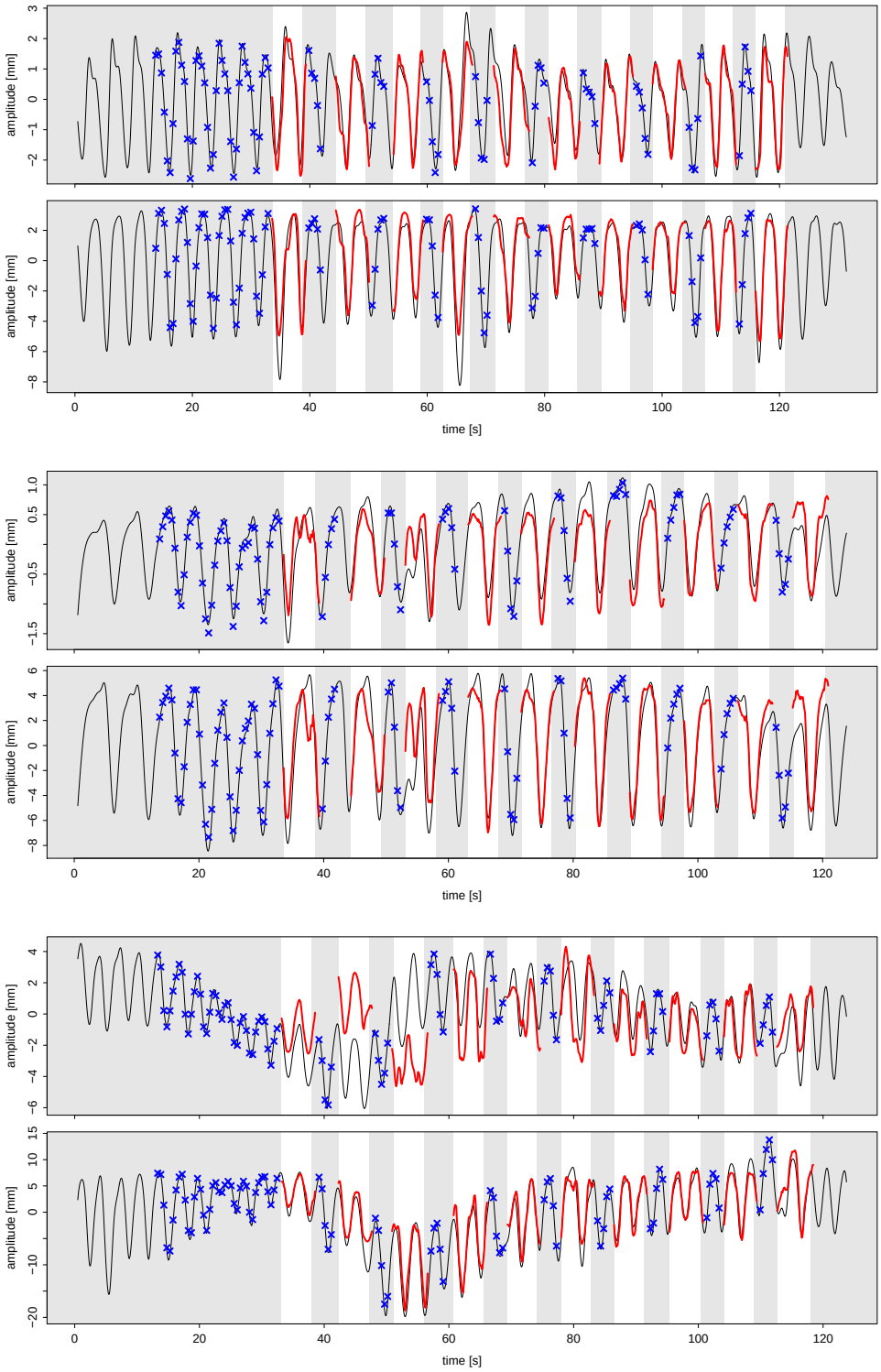

Figure 6.5: Trajectories of target motion (black) and predictions of the correlation model (red) in x-direction (upper panels) and y-direction (lower panels) for the three breathing traces. The shaded areas correspond to beam holds. Blue crosses represent internal motion observations of the x-ray imaging system.

Table 6.2: Combined prediction and correlation model errors for the three breathing traces in x- and y-directions as extracted from dynamic log-files. Absolute root mean squared errors (RMSE) and errors normalized with standard deviations of breathing trajectories.

	Absolute RMSE (mm)		Normalized RMSE	
Breathing trace	x	y	x	y
1	0.47	1.03	0.37	0.37
2	0.32	1.76	0.52	0.45
3	2.41	1.96	1.03	0.29

only a minor role for the overall prediction accuracy. As a consequence of the decreased latency, the corresponding total RMSE values were smaller than the previously observed geometric tracking errors.

Dosimetric tracking accuracy

Figure 6.6 illustrates the dosimetric accuracy analysis for breathing trace 3. For the no-tracking delivery, almost all pixels within the high dose area failed the 2%/2mm gamma criterion. In spite of the relatively large geometric uncertainties shown in table 6.2, the tracking delivery could substantially reduce the gamma failure rate.

Table 6.3 summarizes the results of the dosimetric tracking accuracy analysis for the three breathing traces. 2%/2mm failure rates were decreased substantially for breathing traces 2 and 3. For trace 1, the gamma failure rate of the no-tracking delivery was already small and tracking yielded only a slight improvement.

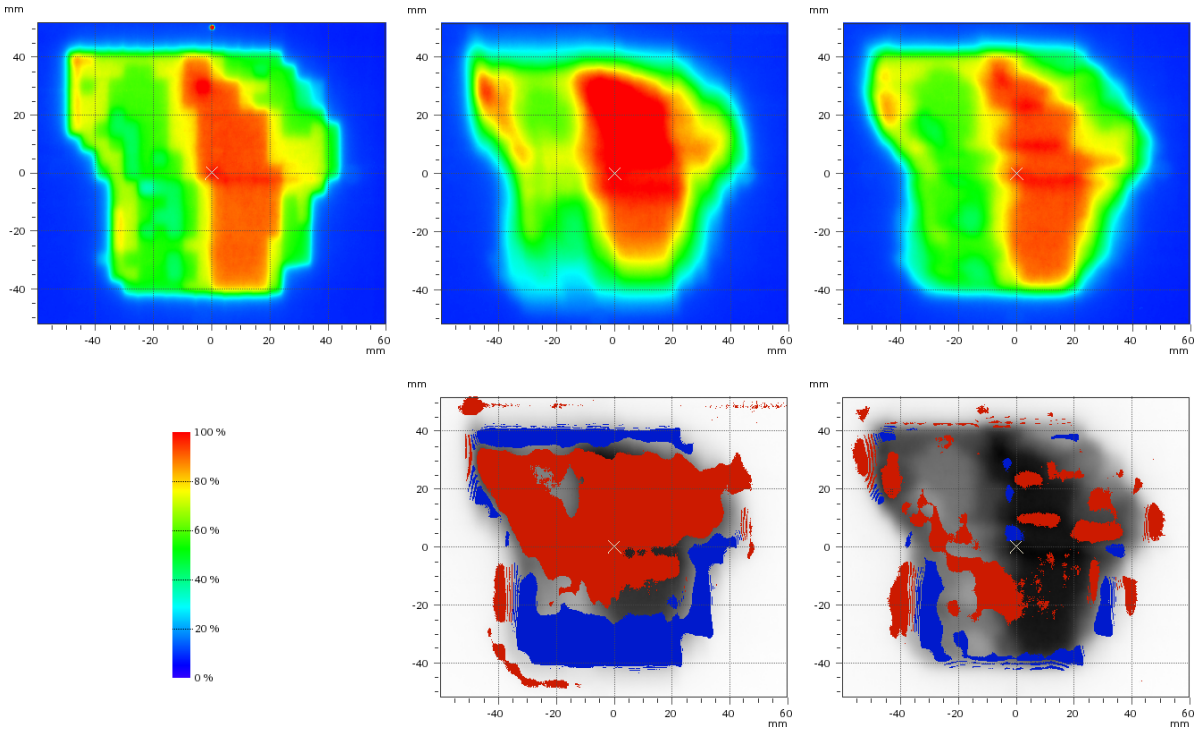

Figure 6.6: (Upper row) Dose distributions of the single IMRT beam. Static reference (left) and deliveries to the target moving on breathing trace 3 without (middle) and with (right) tracking applied. (Lower row) Gamma-test results displayed as grayscale dose distribution with gamma-indexes >1 marked in red for overdosage and blue for underdosage.

Table 6.3: 2%/2mm gamma failure rates of the single IMRT beam applied to the target moving on three breathing traces.

Breathing trace	Without tracking [%]	With tracking [%]
1	5.0	4.0
2	18.2	11.3
3	41.3	16.1

6.3 Discussion

We have successfully integrated a novel x-ray intra-fractional motion monitoring system with our MLC tracking control system, the MTCS. The x-ray imaging system uses the in-line geometry to monitor the most relevant part of intra-fractional target motion perpendicular to the treatment beam – the directions which usually feature steep dose gradients. The imaging system can monitor target motion continuously at a maximum frame-rate of 7.1 Hz while the treatment beam is turned on. We have evaluated the MLC tracking performance based on the x-ray imaging system for two setups: Firstly, based solely on the x-ray imagery and secondly, based on combined external surrogate motion monitoring and sparse x-ray internal motion monitoring.

The x-ray imaging system can detect marker positions with a latency of (82 ± 1) ms. The total system latency for MLC tracking based solely on x-ray imagery was (618 ± 6) ms. The performance of the tracking system based solely on x-ray imagery was assess geometrically through an analysis of portal images acquired during the tracking deliveries. Tracking errors normalized to the no-tracking deliveries were approximately 0.4 for both the x- and y-coordinate of three breathing traces. An analysis of dynamic MTCS log-files showed that the remaining geometric tracking errors were almost completely caused by prediction errors. Target motion forward prediction was based on support vector regression prediction (section 2.2.3) with continuous adaptive-expansive retraining (section 2.2.4). The predictor showed a good prediction performance when compared to three other state-of-the-art respiratory motion predictors (section 2.3). We can therefore conclude that, given the large latency of the integrated tracking system, the geometric tracking accuracy can not be further improved.

The MLC tracking performance based on the combined external surrogate and internal x-ray target motion monitoring system was assessed dosimetrically for a singly, highly modulated step-and-shoot IMRT beam. The system established an external/internal correlation model based on sparse internal motion observations. The x-ray images were acquired prior to or in between the delivery of the individual segments of the IMRT beam. The correlation model was also based on support vector regression. It showed superior prediction accuracies in the correlation model comparison study presented in section 3.3.1. The real-time part of the integrated tracking system is based solely on the external surrogate motion. The total system latency of (507 ± 14) ms was therefore smaller than for the tracking system based solely on x-ray imagery.

The accuracies of external motion forward prediction and of correlation model errors were assessed through an analysis of dynamic log-files of the MTCS and the 4D motion stage. The results of the prediction and correlation model accuracy analysis were compared with the geometric tracking errors of the tracking system based solely on x-ray imagery. This comparison is meaningful, because geometric tracking errors were primarily caused

by prediction errors. External motion forward prediction accuracy of the combined external/internal system was superior to the x-ray only system due to the smaller latency. For three out of six analyzed trajectories (x- and y-directions of three breathing traces), the correlation model introduced only minor errors and the combined prediction and correlation model error was superior to the geometric tracking error of the x-ray only system. Two cases were however slightly deteriorated and one case was even drastically deteriorated compared to the x-ray only system. In the latter case, the correlation model completely failed to adapt to a strong baseline drift in x-direction.

The results of the dosimetric tracking accuracy analysis showed substantially reduced 2%/2mm gamma failure rates for the tracking deliveries. Similar to the dosimetric tracking accuracy analysis of dynamic IMRT deliveries in section 5.4.2, pixels failing the gamma criterion with tracking applied were observed not only at the border of, but also within the high dose area of the IMRT field. The remaining dosimetric errors were strongly dependent on the geometric tracking accuracy. The previously reported dosimetric error of a the step-and-shoot IMRT tracking delivery in section 5.4.2 was approximately equal to the result for breathing trace 3, although the geometric errors were much smaller. We suspect that this inconsistency is due to the different films used for dosimetric accuracy quantification. The radiographic EDR2 films used for the x-ray system measurements show a strongly reduced noise level compared to the radiochromic EBT films used for the Calypso System measurements in section 5.4.2.

7 Summary and conclusions

Tracking system integration

In this thesis, we have substantially extended and improved a previously in-house developed MLC tracking system (Tacke, 2009; Tacke et al., 2010) based on a Siemens 160 MLC mounted on a research Siemens ARTISTE linac. The system is able to adapt the MLC aperture in real-time to continuously monitored irregular 3D target motion. The system supports MLC tracking deliveries of conformal radiotherapy, step-and-shoot IMRT, dynamic IMRT and rotational IMRT. We have integrated the system with three motion monitoring systems: the electromagnetic Calypso System, a recently in-house developed x-ray imaging system (Fast et al., 2011a,b), and a combined external surrogate motion and internal x-ray motion monitoring system. The external surrogate monitoring system was based on a linear potentiometer, which could however be easily replaced with a clinically applicable system.

The implementation of the combined external and internal motion monitoring system is based on a correlation model between external and internal motion. During MLC tracking deliveries, the MLC tracking control system (MTCS) automatically establishes the external/internal correlation model based on sparse x-ray image acquisitions. The real-time MLC tracking procedure is then based solely on the external motion monitoring system. The combined external/internal motion monitoring system drastically reduces additional ionizing radiation doses of the x-ray only system and is therefore suitable for clinical applications. The integrated MLC tracking system based on combined external/internal motion monitoring requires no additional hardware components for the ARTISTE radiotherapy suite except for the external surrogate monitoring system. An implementation of the system into a clinical setting could consequently be relatively cost-effective.

The MTCS does not directly control leaf positions and velocities, but sends MLC shape requests to a Siemens Collimator Control (SCC) unit, which performs the physical leaf actuation. The MLC aperture adaptation process involves consequently no feedback of the physically realized leaf motion. We have therefore implemented a verification loop into the MTCS, which continuously assesses the tracking performance and turns the treatment beam automatically off in case of tracking inaccuracies. As an additional tracking

performance verification tool, we have implemented a real-time visualization of the leaf positions, which allows the operator to manual intervene in abnormal situations.

The vastly extended functionality of the MTCS was realized through a complete redesign of the MLC tracking software package. As an additional benefit, the software redesign yielded a strongly improved application reliability. Upon the detection of exceptions – such as connection break-ups to the external devices or abnormally long computation times of individual subroutines – the MTCS turns the treatment beam off and enters a waiting state until the exception is resolved. From a technical point of view, we consider the MTCS to be well prepared for clinical applications, provided that thorough quality assurance routines for MLC tracking – for instance as proposed by Sawant et al. (2010) – are implemented.

Prediction of respiratory motion

As a consequence of the indirect MLC control through the SCC, the latency between MLC shape requests and the corresponding physical leaf motion is large. We have measured a MLC latency of (473 ± 10) ms, which is the major contribution to the total latency of the tracking systems integrated with the Calypso System (586 ± 3 ms), the x-ray motion monitoring system (618 ± 6 ms), and the combined external surrogate and internal x-ray motion monitoring system (507 ± 14 ms). Consequently, the compensation of the total system latency by means of a forward prediction of the target motion is essential for accurate tracking of rapid organ motion due to respiration.

To guide our choice of a suitable target motion forward prediction model, we have performed a comprehensive comparison study of four state-of-the-art respiratory motion predictors. The comparison study was not limited to the specific prediction scenario of our tracking system, but covered a wide range of latencies and motion monitoring sampling rates.

The considered prediction models learn the patient specific breathing pattern from a training data set. Besides the free parameters of the prediction model, which are automatically optimized in the predictor training phase, the considered predictors feature a set of model parameters, which have to be selected prior to predictor training. Our study revealed that the prediction performance depended strongly on the choice of the model parameters. We have therefore optimized the model parameters of the considered predictors through a grid search in the multidimensional model parameter space. The time-consuming model parameter optimization was performed on a patient-population level so that model parameter sets were obtained, which yielded good prediction performances for all considered breathing traces.

The comparative prediction model performance assessments were performed with the patient-population optimized model parameters. Our study showed that the performance differences of the considered prediction models were surprisingly small; all considered predictors roughly halved the errors of using no prediction. The neural network predictor slightly outperformed the support vector regression, linear regression and kernel density estimation predictors. The small difference between the predictors were contradictory to previously published studies, which did however not consider model parameter optimization to a – from our point of view – sufficient degree. We conclude from our results that the correct usage of the considered respiratory motion predictors (*i.e.,* the thorough model parameter tuning) is supposedly more important than the actual choice of the prediction model. Due to implementation advantages, we integrated the support vector regression and linear regression predictors into the MTCS.

Tracking performance assessments

The tracking performance assessments presented in chapters 5 and 6 evaluated geometric and dosimetric tracking accuracies. Geometric tracking errors were quantified by measuring deviations of target positions and MLC aperture centroid positions based on portal imagery acquired during the tracking experiments. Dosimetric tracking accuracy was assessed in terms of the gamma criterion based on radiographic and radiochromic film dosimetry. We found that the geometric tracking errors were predominantly caused by target motion forward prediction errors and correlation model prediction errors. The MLC aperture followed accurately the MLC shape requests sent to the SCC, thereby smoothing the noisy trajectory requests. For the given large MLC latency, we have consequently reached the optimum achievable geometric tracking performance through the implementation of state-of-the-art prediction models with thorough model parameter tuning.

The dosimetric tracking performance assessments identified geometric tracking errors as well as MLC hardware constraints as main contributors to dosimetric tracking errors. The main MLC hardware limitations were: the leaf width of 5 mm, the limited maximum leaf velocity of 43 mm/s and the radiation leakage through the tips of closed leaf pairs. The hardware constraints limited the dosimetric accuracy of target motion compensation perpendicular to the leaf travel direction. The relative importance of the geometric uncertainties and the hardware limitations depended on the radiotherapy delivery mode.

The dosimetric tracking accuracy assessments were based on the gamma criterion, which brings dose difference and distance-to-agreement maps together. For deliveries with a circular radiation field, we observed roughly constant 2%/2mm gamma failure rates, if 2D root mean squared geometric tracking errors were smaller than 3 mm. The gamma failure rates however increased rapidly for geometric tracking errors larger than 3 mm. The

remaining gamma failures for small geometric uncertainties were located at overdosage regions besides the high dose area. The overdosage was primarily caused by leakage through closed leaf pairs, which were positioned adjacent to the open field to be able to quickly open in case of target motion perpendicular to the leaf travel direction.

For step-and-shoot IMRT deliveries, dosimetric tracking errors were generally larger and occurred not only at the border of, but also within the high dose area of the IMRT field. The distribution of dosimetric errors over the modulated field is probably due to different positions of closed leaf pairs of the individual segments of the step-and-shoot IMRT fields. In contrast to the tracking deliveries with the circular radiation field, the dosimetric errors of step-and-shoot IMRT deliveries depended strongly on the corresponding geometric uncertainties.

We have evaluated the dosimetric tracking accuracies for multiple dynamic IMRT delivery modes. The dosimetric tracking errors were generally larger than for step-and-shoot IMRT deliveries. The relative importance of the geometric uncertainties and the hardware limitations depended on both the dynamic IMRT delivery mode and the specific characteristics of the target motion pattern.

An analysis of the dosimetric tracking accuracy in terms of the gamma failure rate has several weaknesses: It does neither give insight into the location nor the magnitude of the dose deviations. Furthermore, the insensitivity of the gamma metric to shifts of the entire dose distribution below its spatial tolerance limit is problematic in regions of sharp dose gradients intended to protect organs at risk. The presented dosimetric tracking accuracy evaluation can consequently not comprehensively quantify the clinical benefit of the tracking deliveries.

Comparison with other MLC tracking systems

Real-time MLC tracking has been pioneered at the University of Stanford (Keall et al., 2006a). The Stanford MLC tracking system is based on the Varian Millennium MLC (Varian Medical Systems, Palo Alto, CA). The latency of the Varian MLC tracking system is substantially smaller than for our Siemens MLC tracking system. Poulsen et al. (2010b) reported a MLC latency of only 52 ms. For the total latency of the integrated MLC tracking system, values of 220 ms with the Calypso System (Sawant et al., 2009) and 450 ms and 570 ms with MV and kV x-ray imaging (Cho et al., 2009; Poulsen et al., 2010a) were reported. The large latency values of the imaging systems were due to an indirect image transfer via image file storage and subsequent hard disk access. The latency could be substantially reduced through a direct image access to 382 ms and 264 ms with MV and kV x-ray imaging at a frame-rate of 5 Hz (Fledelius et al., 2011).

Various geometric tracking accuracy assessments have been reported for the Stanford MLC tracking system integrated with: optical external surrogate monitoring (Keall et al., 2006a; Sawant et al., 2008), the Calypso System (Sawant et al., 2009), combined kV and MV, kV-only and MV-only x-ray imaging (Cho et al., 2009; Poulsen et al., 2010a, 2011), as well as kV and MV imaging combined with external surrogate monitoring (Cho et al., 2011). Respiratory motion tracking accuracies were well below 2 mm with all investigated tracking system integrations. It is evident from our presented results that geometric tracking accuracies depend strongly on the specific breathing trace. A comparison of experimental results obtained with different breathing traces is therefore problematic. Our prediction accuracy analysis showed strongly increased prediction errors for increased system latencies. The shorter latency of the Stanford MLC tracking system represents consequently a clear advantage in terms of geometric tracking accuracy.

Sawant et al. (2008) reported on dosimetric tracking accuracies of the Stanford MLC tracking system for conformal radiotherapy, step-and-shoot IMRT, dynamic IMRT and rotational IMRT based on film dosimetry. The results were similar to our findings: The gamma failure rates were drastically reduced by the tracking deliveries, but could not be completely eliminated in spite of sub-millimeter geometric tracking accuracies for sinusoidal motion patterns. The results of the IMRT deliveries were considerably less accurate than for the conformal radiotherapy delivery.

McQuaid et al. (2009) has performed a feasibility study of MLC tracking based on the Elekta MLCi (Elekta Oncology Systems Ltd., Crawley, UK). The tracking experiments were performed with sinusoidal motion patterns. Considerable dosimetric accuracy improvements were observed, especially if the collimator angle was aligned with the major axis of the target motion trajectory. The presented tracking system was neither able to monitor target motion in real-time, nor did it support MLC adaptation during the radiotherapy delivery. It accounted for target motion during the treatment planning phase and relied on a perfectly long-term predictable target motion. The system is consequently not applicable to irregular patient breathing trajectories.

Comparison with other tumor tracking systems

Besides the MLC tracking approach, other techniques for tumor tracking have been proposed, such as repositioning of the entire linear accelerator with the CyberKnife System (Schweikard et al., 2004; Hoogeman et al., 2009), robotic patient couch tracking with the HexaPOD (D'Souza and McAvoy, 2006; Wilbert et al., 2008), or the VERO gimbals tracking system (Takayama et al., 2009; Depuydt et al., 2011). The CyberKnife Synchrony system (Accuray Inc., Sunnyvale, CA) is a real-time tracking system for tumors in the lung or the upper abdomen. Up to now, it is the only clinically applied tumor tracking system. Motion monitoring of the CyberKnife system is based on a combined

external surrogate and internal stereoscopic x-ray system. The total system latency amounts to 115 ms. Hoogeman et al. (2009) quantified average prediction and correlation model errors for 44 lung cancer patients through a straight line fit to absolute RMS errors as a function of the standard deviation of the raw breathing signals. The slopes were 0.1 for external motion forward prediction and 0.36 (SI), 0.40 (LR), and 0.33 (AP) for the correlation model estimations. Due to the small latency, the geometric tracking error of the CyberKnife system is dominated by the correlation model error.

The VERO system (BrainLAB AG, Feldkirchen, Germany and Mitsubishi Heavy Industries, Tokyo, Japan) features a 6 MV linac with a relatively small MLC mounted on a O-ring gantry. A gimbals system allows pan and tilt rotation of the entire linac-MLC assembly for tumor tracking. The latency of the tracking system integrated with optical external surrogate motion monitoring amounts to 47 ms. Depuydt et al. (2011) reported RMS geometric tracking accuracies for lung tumor motion below 0.22 mm.

The comparative performance of a HexaPOD tracking system developed by Wilbert et al. (2008) and MLC tracking was evaluated in this section 5.3. The HexaPOD tracking system clearly outperformed our MLC tracking in terms of dosimetric accuracy in spite of slightly worse geometric tracking accuracies.

The hardware limitations of MLC tracking due to the leaf width of 5 mm, the limited leaf velocity and the intra-leaf leakage represent a clear disadvantage of MLC tracking compared to VERO, CyberKnife and HexaPOD tracking. The dosimetric MLC tracking errors even for small geometric uncertainties complicate the estimation of the clinical benefits achievable with the tracking approach. For the VERO, CyberKnife and HexaPOD systems, in contrast, the achievable clinical benefits can easily estimated from the geometric tracking accuracies, for instance with aid of the population-based safety margin recipe proposed by Van Herk (2004).

A clear advantage of MLC tracking compared to HexaPOD tracking is the increased patient comfort as well as the avoidance of possible dose errors due to organ deformations induced by the rapid accelerations of the entire patient during respiratory motion couch tracking deliveries. Compared to the VERO and CyberKnife tracking systems, MLC tracking offers several advantages: The field size of the VERO system is relatively small, which limits its possible fields of application. The CyberKnife system is not equipped with a MLC and the delivery times are often substantially larger than for comparable radiotherapy deliveries with a medical x-ray producing linac. Additionally, MLC tracking could be advantageous from an economical point of view. Medical x-ray producing linacs equipped with MLCs are the 'working horses' of modern radiotherapy. MLC tracking essentially requires software modifications and has therefore the potential for a relatively cost-effective, widespread clinical implementation.

Outlook

The MLC tracking performance assessments presented in this thesis demonstrated that the geometric tracking accuracy can hardly be further improved with the given large latency of the Siemens 160 MLC. In order to possibly enhance the dosimetric tracking accuracy, we suggest the following further investigations: Firstly, the influence of positioning strategies of closed leaf pairs adjacent to the MLC aperture should be systematically studied. The number of closed leaf pairs could be adapted to the amplitude of the breathing motion. It could also be helpful to frequently shift the position of closed leaf pairs relative to the open field so that the local overdosage would be reduced through a smearing over a larger area. Secondly, the y-laws of the MLC could be used to dynamically collimate the treatment beam perpendicular to the leaf travel direction. This could not only eliminate the leakage through closed leaf pairs, but also increase the 5 mm resolution of MLC tracking determined by the leaf width at the borders of the MLC field. Thirdly, the alignment of the collimator angle with the major axis of the target motion trajectory as proposed by McQuaid et al. (2009) should be investigated. It should however be noted that the – generally beam angle dependent – collimator angle alignment has to be performed at the treatment planning phase. The approach consequently requires that the main axis of the target motion trajectory is stable over the entire course of the radiotherapy treatment.

Our MLC tracking implementation accounts for 3D rigid target translations. In section 4.2.2 we have introduced several previously proposed strategies to account for more complex forms of organ motion, such as 1D translations and deformations (Papiez and Rangaraj, 2005; Tacke et al., 2007), differential organ motion (Webb and Binnie, 2006; McClelland et al., 2007), or the compensation of in-plane rotations (Wu et al., 2011). We consider the 4D planning and 4D delivery strategy proposed by Suh et al. (2009) to be highly promising. As our tracking software implementation is already prepared for the delivery of 4D treatment plans, we suggest future experimental validation of 4D planning and 4D delivery strategies.

Our dosimetric tracking accuracy assessments based on the gamma metric could not comprehensively quantify the clinical benefits of MLC tracking. Future work should experimentally evaluate more clinically relevant measures for dosimetric accuracy of MLC tracking deliveries, such as dose-volume histograms of the target volume and nearby organs. Such studies should also investigate the extend to which the dosimetric tracking errors can be compensated by means of adequate safety margins. If such investigations were performed with several target motion traces as well as several patient geometries, they could finally yield a safety margin recipe for remaining geometric errors of MLC tracking deliveries. Although our presented dosimetric tracking accuracy assessments could not fully quantify the clinical benefits of the MLC tracking system, we demonstrated substantial improvements in terms of the gamma criterion, which shows that the

negative effects of intra-fractional organ motion on the delivered dose distributions could be eliminated to a large extend.

Bibliography

Ahn, S., Yi, B., Suh, Y., Kim, J., Lee, S., Shin, S., and Choi, E. (2004). A feasibility study on the prediction of tumour location in the lung from skin motion. *British journal of radiology*, 77(919):588.

Balter, J., Wright, J., Newell, L., Friemel, B., Dimmer, S., Cheng, Y., Wong, J., Vertatschitsch, E., and Mate, T. (2005). Accuracy of a wireless localization system for radiotherapy. *International Journal of Radiation Oncology* Biology* Physics*, 61(3):933–937.

Bellman, R. E. (1957). *Dynamic programming*. Princeton University Press, Princeton, NJ.

Berbeco, R., Hacker, F., Ionascu, D., and Mamon, H. (2007). Clinical feasibility of using an EPID in 'cine' mode for Image-Guided verification of stereotactic body radiotherapy. *International Journal of Radiation Oncology* Biology* Physics*, 69(1):258–266.

Berbeco, R., Nishioka, S., Shirato, H., Chen, G., and Jiang, S. (2005). Residual motion of lung tumours in gated radiotherapy with external respiratory surrogates. *Physics in medicine and biology*, 50:3655.

Bert, C., Metheany, K., Doppke, K., and Chen, G. (2005). A phantom evaluation of a stereo-vision surface imaging system for radiotherapy patient setup. *Medical physics*, 32:2753.

Bolliger, C., Koegelenberg, C., Von Groote-Bidlingmaier, F., Bernasconi, M., Steyn, D., Tamm, M., Zimmerman, F., Papachristofilou, A., Schratzenstaller, U., and Paris, G. (2011). First report of implantation of anchored electromagnetic fiducials in human lung cancers for real-time tumor localization and tracking during radiation therapy. *International journal of radiation oncology, biology, physics*, 81(2):S578–S579.

Bortfeld, T., Jiang, S. B., and Rietzel, E. (2004). Effects of motion on the total dose distribution. *Seminars in Radiation Oncology*, 14(1):41–51.

Cerviño, L., Du, J., and Jiang, S. (2011). MRI-guided tumor tracking in lung cancer radiotherapy. *Physics in Medicine and Biology*, 56:3773.

Chambers, J. M. M. (1983). *Graphical methods for data analysis*. Wadsworth International Group, Belmont, CA.

Chang, C. C. and Lin, C. J. (2001). LIBSVM: a library for support vector machines. Software available at http://www. csie. ntu. edu. tw/cjlin/libsvm.

Cho, B., Poulsen, P., Sawant, A., Ruan, D., and Keall, P. (2011). Real-time target position estimation using stereoscopic kilovoltage/megavoltage imaging and external respiratory monitoring for dynamic multileaf collimator tracking. *International Journal of Radiation Oncology* Biology* Physics*, 79(1):269–278.

Cho, B., Poulsen, P. R., Sloutsky, A., Sawant, A., and Keall, P. J. (2009). First demonstration of combined kV/MV image-guided real-time dynamic multileaf-collimator target tracking. *International Journal of Radiation Oncology* Biology* Physics*, 74(3):859–867.

Dawson, L. and Jaffray, D. (2007). Advances in image-guided radiation therapy. *Journal of clinical oncology*, 25(8):938.

Dempsey, J., Benoit, D., Fitzsimmons, J., Haghighat, A., Li, J., Low, D., Mutic, S., Palta, J., Romeijn, H., and Sjoden, G. (2005). A device for realtime 3D image-guided IMRT. *International Journal of Radiation Oncology* Biology* Physics*, 63:S202–S202.

Depuydt, T., Verellen, D., Haas, O., Gevaert, T., Linthout, N., Duchateau, M., Tournel, K., Reynders, T., Leysen, K., Hoogeman, M., et al. (2011). Geometric accuracy of a novel gimbals based radiation therapy tumor tracking system. *Radiotherapy and Oncology*, 98(3):365–372.

D'Souza, W. D. and McAvoy, T. J. (2006). An analysis of the treatment couch and control system dynamics for respiration-induced motion compensation. *Medical physics*, 33:4701.

Ernst, F., Bruder, R., Schlaefer, A., and Schweikard, A. (2011). Correlation between external and internal respiratory motion: a validation study. *International Journal of Computer Assisted Radiology and Surgery*, page 1–10.

Ernst, F. and Schweikard, A. (2009). Forecasting respiratory motion with accurate online support vector regression (SVRpred). *International journal of computer assisted radiology and surgery*, 4(5):439–447.

Faddegon, B., Wu, V., Pouliot, J., Gangadharan, B., and Bani-Hashemi, A. (2008). Low dose megavoltage cone beam computed tomography with an unflattened 4 MV beam from a carbon target. *Medical physics*, 35:5777.

Fallone, B., Carlone, M., Murray, B., Rathee, S., Stanescu, T., Steciw, S., Wachowicz, K., and Kirkby, C. (2007). Development of a Linac-MRI system for Real-Time ART. *Medical Physics*, 34:2547.

Fallone, B. G., Murray, B., Rathee, S., Stanescu, T., Steciw, S., Vidakovic, S., Blosser, E., and Tymofichuk, D. (2009). First MR images obtained during megavoltage photon irradiation from a prototype integrated linac-MR system. *Medical Physics*, 36:2084.

Fast, M., Krauss, A., Nill, S., and Oelfke, U. (2011a). Position detection accuracy of a novel Linac-Mounted Intra-Fractional X-Ray imaging system. *Medical Physics*, 38:3757.

Fast, M., Krauss, A., Oelfke, U., and Nill, S. (2011b). Position detection accuracy of a novel linac-mounted intra-fractional x-ray imaging system. *Medical Physics*, accepted for publication.

Fledelius, W., Keall, P., Cho, B., Yang, X., Morf, D., Scheib, S., and Poulsen, P. (2011). Tracking latency in image-based dynamic MLC tracking with direct image access. *Acta Oncologica*, 50(6):952–959.

Gierga, D., Brewer, J., Sharp, G., Betke, M., Willett, C., and Chen, G. (2005). The correlation between internal and external markers for abdominal tumors: implications for respiratory gating. *International Journal of Radiation Oncology* Biology* Physics*, 61(5):1551–1558.

Harris, E., Miller, N., Bamber, J., Evans, P., and Symonds-Tayler, J. (2007). Performance of ultrasound based measurement of 3D displacement using a curvilinear probe for organ motion tracking. *Physics in medicine and biology*, 52:5683.

Hastie, T., Tibshirani, R., and Friedman, J. H. (2001). *The elements of statistical learning: data mining, inference, and prediction*. Springer.

Hendee, W. and Ritenour, E. (2002). *Medical imaging physics*. LibreDigital.

Hofmann, K. (2011). *Implementation of a dose delivery modality using dynamic multileaf collimation and its application for real-time tumor tracking*. Diploma thesis, University of Heidelberg.

Hoisak, J., Sixel, K., Tirona, R., Cheung, P., and Pignol, J. (2004). Correlation of lung tumor motion with external surrogate indicators of respiration. *International Journal of Radiation Oncology* Biology* Physics*, 60(4):1298–1306.

Hoogeman, M., Prévost, J. B., Nuyttens, J., Pöll, J., Levendag, P., and Heijmen, B. (2009). Clinical accuracy of the respiratory tumor tracking system of the cyberknife: assessment by analysis of log files. *International Journal of Radiation Oncology* Biology* Physics*, 74(1):297–303.

Hsu, A., Miller, N., Evans, P., Bamber, J., and Webb, S. (2005). Feasibility of using ultrasound for real-time tracking during radiotherapy. *Medical physics*, 32:1500.

Ionascu, D., Jiang, S., Nishioka, S., Shirato, H., and Berbeco, R. (2007). Internal-external correlation investigations of respiratory induced motion of lung tumors. *Medical physics*, 34:3893.

Isaksson, M., Jalden, J., and Murphy, M. J. (2005). On using an adaptive neural network to predict lung tumor motion during respiration for radiotherapy applications. *Medical physics*, 32:3801.

Jaffray, D. (2007). Kilovoltage volumetric imaging in the treatment room. *Frontiers of radiation therapy and oncology*, 40:116.

Jaffray, D., Kupelian, P., Djemil, T., and Macklis, R. (2007). Review of image-guided radiation therapy. *Expert review of anticancer therapy*, 7(1):89–103.

Kalet, A., Sandison, G., Wu, H., and Schmitz, R. (2010). A state-based probabilistic model for tumor respiratory motion prediction. *Physics in Medicine and Biology*, 55:7615.

Keall, P. J., Cattell, H., Pokhrel, D., Dieterich, S., Wong, K. H., Murphy, M. J., Vedam, S. S., Wijesooriya, K., and Mohan, R. (2006a). Geometric accuracy of a real-time target tracking system with dynamic multileaf collimator tracking system. *International Journal of Radiation Oncology*Biology*Physics*, 65(5):1579–1584.

Keall, P. J., Mageras, G. S., Balter, J. M., Emery, R. S., Forster, K. M., Jiang, S. B., Kapatoes, J. M., Low, D. A., Murphy, M. J., Murray, B. R., et al. (2006b). The management of respiratory motion in radiation oncology report of AAPM task group 76. *Medical physics*, 33:3874.

Kirkby, C., Stanescu, T., Rathee, S., Carlone, M., Murray, B., and Fallone, B. (2008). Patient dosimetry for hybrid MRI-radiotherapy systems. *Medical physics*, 35:1019.

Korreman, S., Juhler-Nottrup, T., and Boyer, A. (2008). Respiratory gated beam delivery cannot facilitate margin reduction, unless combined with respiratory correlated image guidance. *Radiotherapy and Oncology*, 86(1):61–68.

Korreman, S., Mostafavi, H., Le, Q., and Boyer, A. (2006). Comparison of respiratory surrogates for gated lung radiotherapy without internal fiducials. *Acta Oncologica*, 45(7):935–942.

Korreman, S., Rasch, C., McNair, H., Verellen, D., Oelfke, U., Maingon, P., Mijnheer, B., and Khoo, V. (2010). The european society of therapeutic radiology and oncology – european institute of radiotherapy (ESTRO-EIR) report on 3D CT-based in-room

image guidance systems: A practical and technical review and guide. *Radiotherapy and Oncology*, 94(2):129–144.

Krauss, A., Fast, M., Nill, S., and Oelfke, U. (2011a). Multileaf collimator tracking of respiratory motion using a novel X-Ray monitoring system. *Medical Physics*, 38:3782.

Krauss, A., Nill, S., and Oelfke, U. (2010). Effective tracking of intrafractional organ motion due to breathing using a siemens 160 MLC. *Medical Physics*, 37:3146.

Krauss, A., Nill, S., and Oelfke, U. (2011b). The comparative performance of four respiratory motion predictors for real-time tumour tracking. *Physics in Medicine and Biology*, 56:5303.

Krauss, A., Nill, S., and Oelfke, U. (2011c). Comparative performance of respiratory motion predictors for real-time tumor tracking. *Radiotherapy and Oncology*, 99:S182–S183.

Krauss, A., Nill, S., and Oelfke, U. (2011d). Management of breathing motion through multileaf collimator tracking. *Radiotherapy and Oncology*, 99:S81.

Krauss, A., Nill, S., Tacke, M., and Oelfke, U. (2011e). Electromagnetic Real-Time tumor position monitoring and dynamic multileaf collimator tracking using a siemens 160 MLC: geometric and dosimetric accuracy of an integrated system. *International Journal of Radiation Oncology*Biology*Physics*, 79(2):579–587.

Krauss, A., Rau, A., Tacke, M., Nill, S., and Oelfke, U. (2009). Real-time tumor position monitoring and dynamic dose adaptation: Geometric and dosimetric accuracy of an integrated tracking system. *International journal of radiation oncology, biology, physics*, 75(3):S74.

Kubo, H. D., Len, P. M., Minohara, S., and Mostafavi, H. (2000). Breathing-synchronized radiotherapy program at the university of california davis cancer center. *Medical physics*, 27:346.

Kupelian, P., Willoughby, T., Mahadevan, A., Djemil, T., Weinstein, G., Jani, S., Enke, C., Solberg, T., Flores, N., Liu, D., et al. (2007). Multi-institutional clinical experience with the calypso system in localization and continuous, real-time monitoring of the prostate gland during external radiotherapy. *International Journal of Radiation Oncology* Biology* Physics*, 67(4):1088–1098.

Lagendijk, J., Raaymakers, B., Raaijmakers, A., Overweg, J., Brown, K., Kerkhof, E., van der Put, R., Haardemark, B., van Vulpen, M., and van der Heide, U. (2008). MRI/linac integration. *Radiotherapy and Oncology*, 86(1):25–29.

Langen, K., Pouliot, J., Anezinos, C., Aubin, M., Gottschalk, A., Hsu, I., Lowther, D., Liu, Y., Shinohara, K., Verhey, L., et al. (2003). Evaluation of ultrasound-based prostate localization for image-guided radiotherapy* 1. *International Journal of Radiation Oncology* Biology* Physics*, 57(3):635–644.

Li, X., Stepaniak, C., and Gore, E. (2006). Technical and dosimetric aspects of respiratory gating using a pressure-sensor motion monitoring system. *Medical physics*, 33:145.

Low, D. and Dempsey, J. (2003). Evaluation of the gamma dose distribution comparison method. *Medical Physics*, 30:2455.

Ma, Y., Lee, L., Keshet, O., Keall, P., and Xing, L. (2009). Four-dimensional inverse treatment planning with inclusion of implanted fiducials in IMRT segmented fields. *Medical physics*, 36:2215.

Mao, W., Riaz, N., Lee, L., Wiersma, R., and Xing, L. (2008). A fiducial detection algorithm for real-time image guided IMRT based on simultaneous MV and kV imaging. *Medical physics*, 35:3554.

Mayse, M., Parikh, P., Lechleiter, K., Dimmer, S., Park, M., Chaudhari, A., Talcott, M., Low, D., and Bradley, J. (2008). Bronchoscopic implantation of a novel wireless electromagnetic transponder in the canine lung: a feasibility study. *International Journal of Radiation Oncology* Biology* Physics*, 72(1):93–98.

McClelland, J., Webb, S., McQuaid, D., Binnie, D., and Hawkes, D. (2007). Tracking 'differential organ motion' with a 'breathing' multileaf collimator: magnitude of problem assessed using 4D CT data and a motion-compensation strategy. *Physics in medicine and biology*, 52:4805.

McQuaid, D., Partridge, M., Symonds-Tayler, J., Evans, P., and Webb, S. (2009). Target-tracking deliveries on an elekta linac: a feasibility study. *Physics in medicine and biology*, 54:3563.

Menten, M. J. (2011). *Comparison of a Multileaf Collimator and a Robotic Treatment Couch for Organ Motion Compensation during Radiotherapy.* Bachelor thesis, University of Heidelberg.

Murphy, M., Jalden, J., and Isaksson, M. (2002). Adaptive filtering to predict lung tumor breathing motion during image-guided radiation therapy. *Computer-Assisted Radiology and Surgery–CARS 2002*, page 539–544.

Murphy, M. J. and Dieterich, S. (2006). Comparative performance of linear and nonlinear neural networks to predict irregular breathing. *Physics in Medicine and Biology*, 51:5903.

Murphy, M. J. and Pokhrel, D. (2009). Optimization of an adaptive neural network to predict breathing. *Medical Physics*, 36(1):40.

Nill, S., Unkelbach, J., Dietrich, L., and Oelfke, U. (2005). Online correction for respiratory motion: evaluation of two different imaging geometries. *Physics in medicine and biology*, 50:4087.

Oelfke, U., Tücking, T., Nill, S., Seeber, A., Hesse, B., Huber, P., and Thilmann, C. (2006). Linac-integrated kV-cone beam CT: technical features and first applications. *Medical Dosimetry*, 31(1):62–70.

Pan, T., Lee, T., Rietzel, E., and Chen, G. (2004). 4D-CT imaging of a volume influenced by respiratory motion on multi-slice CT. *Medical physics*, 31:333.

Papiez, L. and Rangaraj, D. (2005). DMLC leaf-pair optimal control for mobile, deforming target. *Medical physics*, 32:275.

Papiez, L., Rangaraj, D., and Keall, P. (2005). Real-time DMLC IMRT delivery for mobile and deforming targets. *Medical physics*, 32:3037.

Pfaffenberger, A. and Oelfke, U. (2011). A transformation approach for dose calculation in a magnetic field. *Radiotherapy and Oncology*, 99:S158–S159.

Poulsen, P., Carl, J., Nielsen, J., Nielsen, M., Thomsen, J., Jensen, H., Kjaergaard, B., Zepernick, P., Worm, E., Fledelius, W., et al. (2011). Megavoltage Image-Based dynamic multileaf collimator tracking of a NiTi stent in porcine lungs on a linear accelerator. *International journal of radiation oncology, biology, physics*.

Poulsen, P., Cho, B., Langen, K., Kupelian, P., and Keall, P. (2008). Three-dimensional prostate position estimation with a single x-ray imager utilizing the spatial probability density. *Physics in medicine and biology*, 53:4331.

Poulsen, P., Cho, B., Ruan, D., Sawant, A., and Keall, P. (2010a). Dynamic multileaf collimator tracking of respiratory target motion based on a single kilovoltage imager during arc radiotherapy. *International Journal of Radiation Oncology* Biology* Physics*, 77(2):600–607.

Poulsen, P., Cho, B., Sawant, A., Ruan, D., and Keall, P. (2010b). Detailed analysis of latencies in image-based dynamic MLC tracking. *Medical physics*, 37:4998.

Poulsen, P., Cho, B., Sawant, A., Ruan, D., and Keall, P. (2010c). Dynamic MLC tracking of moving targets with a single kV imager for 3D conformal and IMRT treatments. *Acta Oncologica*, 49(7):1092–1100.

Putra, D., Haas, O. C., Mills, J. A., and Burnham, K. J. (2008). A multiple model approach to respiratory motion prediction for real-time IGRT. *Physics in medicine and biology*, 53:1651.

Raaijmakers, A., Raaymakers, B., and Lagendijk, J. (2005). Integrating a MRI scanner with a 6 MV radiotherapy accelerator: dose increase at tissue–air interfaces in a lateral magnetic field due to returning electrons. *Physics in medicine and biology*, 50:1363.

Raaymakers, B., Raaijmakers, A., Kotte, A., Jette, D., and Lagendijk, J. (2004). Integrating a MRI scanner with a 6 MV radiotherapy accelerator: dose deposition in a transverse magnetic field. *Physics in medicine and biology*, 49:4109.

Rangaraj, D. and Papiez, L. (2005). Synchronized delivery of DMLC intensity modulated radiation therapy for stationary and moving targets. *Medical physics*, 32:1802.

Rau, A., Nill, S., Eidens, R., and Oelfke, U. (2008). Synchronized tumour tracking with electromagnetic transponders and kV x-ray imaging: evaluation based on a thorax phantom. *Physics in Medicine and Biology*, 53:3789.

Ren, Q., Nishioka, S., Shirato, H., and Berbeco, R. (2007). Adaptive prediction of respiratory motion for motion compensation radiotherapy. *Physics in medicine and biology*, 52:6651.

Riaz, N., Shanker, P., Wiersma, R., Gudmundsson, O., Mao, W., Widrow, B., and Xing, L. (2009). Predicting respiratory tumor motion with multi-dimensional adaptive filters and support vector regression. *Physics in Medicine and Biology*, 54:5735.

Richter, A., Wilbert, J., Baier, K., Flentje, M., and Guckenberger, M. (2010). Feasibility study for markerless tracking of lung tumors in stereotactic body radiotherapy. *International Journal of Radiation Oncology* Biology* Physics*, 78(2):618–627.

Rottmann, J., Aristophanous, M., Chen, A., et al. (2010). A multi-region algorithm for markerless beam's-eye view lung tumor tracking. *Physics in Medicine and Biology*, 55:5585.

Ruan, D. (2010). Kernel density estimation-based real-time prediction for respiratory motion. *Physics in Medicine and Biology*, 55:1311.

Ruan, D., Fessler, J., Balter, J., Berbeco, R., Nishioka, S., and Shirato, H. (2008). Inference of hysteretic respiratory tumor motion from external surrogates: a state augmentation approach. *Physics in medicine and biology*, 53:2923.

Ruan, D. and Keall, P. (2010). Online prediction of respiratory motion: multidimensional processing with low-dimensional feature learning. *Physics in Medicine and Biology*, 55:3011.

Salter, B., Sarkar, V., Wang, B., Shukla, H., Szegedi, M., and Rassiah-Szegedi, P. (2011). Rotational IMRT delivery using a digital linear accelerator in very high dose rate'burst mode'. *Physics in Medicine and Biology*, 56:1931.

Sawant, A., Dieterich, S., Svatos, M., and Keall, P. (2010). Failure mode and effect analysis-based quality assurance for dynamic MLC tracking systems. *Medical Physics*, 37:6466.

Sawant, A., Smith, R., Venkat, R., Santanam, L., Cho, B., Poulsen, P., Cattell, H., Newell, L., Parikh, P., and Keall, P. (2009). Toward submillimeter accuracy in the management of intrafraction motion: the integration of real-time internal position monitoring and multileaf collimator target tracking. *International Journal of Radiation Oncology* Biology* Physics*, 74(2):575–582.

Sawant, A., Venkat, R., Srivastava, V., Carlson, D., Povzner, S., Cattell, H., and Keall, P. (2008). Management of three-dimensional intrafraction motion through real-time DMLC tracking. *Medical physics*, 35:2050.

Schlosser, J., Salisbury, K., and Hristov, D. (2010). Telerobotic system concept for real-time soft-tissue imaging during radiotherapy beam delivery. *Medical Physics*, 37:6357.

Schmitt, D., Nill, S., Herfarth, K., Münter, M., Pfitzenmaier, J., Zabel-du Bois, A., Röder, F., Huber, P., and Oelfke, U. (2010). Intrafraction organ motion during prostate radiotherapy: Quantitative correlation of treatment time and margin size. *International journal of radiation oncology, biology, physics*, 78(3):S752.

Schweikard, A., Shiomi, H., and Adler, J. (2004). Respiration tracking in radiosurgery. *Medical physics*, 31:2738.

Schöffel, P., Harms, W., Sroka-Perez, G., Schlegel, W., and Karger, C. (2007). Accuracy of a commercial optical 3D surface imaging system for realignment of patients for radiotherapy of the thorax. *Physics in Medicine and Biology*, 52:3949.

Seppenwoolde, Y., Berbeco, R., Nishioka, S., Shirato, H., and Heijmen, B. (2007). Accuracy of tumor motion compensation algorithm from a robotic respiratory tracking system: a simulation study. *Medical physics*, 34:2774.

Sharp, G. C., Jiang, S. B., Shimizu, S., and Shirato, H. (2004). Prediction of respiratory tumour motion for real-time image-guided radiotherapy. *Physics in Medicine and Biology*, 49:425.

Shirato, H., Shimizu, S., Kitamura, K., Nishioka, T., Kagei, K., Hashimoto, S., Aoyama, H., Kunieda, T., Shinohara, N., Dosaka-Akita, H., and Miyasaka, K. (2000a). Four-dimensional treatment planning and fluoroscopic real-time tumor tracking radiother-

apy for moving tumor. *International Journal of Radiation Oncology*Biology*Physics*, 48(2):435–442.

Shirato, H., Shimizu, S., Kunieda, T., Kitamura, K., van Herk, M., Kagei, K., Nishioka, T., Hashimoto, S., Fujita, K., Aoyama, H., et al. (2000b). Physical aspects of a real-time tumor-tracking system for gated radiotherapy. *International Journal of Radiation Oncology Biology Physics*, 48(4):1187–1196.

Sonke, J., Lebesque, J., and van Herk, M. (2008). Variability of four-dimensional computed tomography patient models. *International Journal of Radiation Oncology* Biology* Physics*, 70(2):590–598.

Sonke, J., Zijp, L., Remeijer, P., and van Herk, M. (2005). Respiratory correlated cone beam CT. *Medical Physics*, 32:1176.

Stein, J., Bortfeld, T., Dorschel, B., and Schlegel, W. (1994). Dynamic x-ray compensation for conformal radiotherapy by means of multi-leaf collimation. *Radiotherapy and Oncology*, 32(2):163–173.

Steinke, M. (2010). *Performance characteristics of a novel megavoltage cone beam computed tomography device*. Diploma thesis, University of Heidelberg.

Stützel, J., Oelfke, U., and Nill, S. (2008). A quantitative image quality comparison of four different image guided radiotherapy devices. *Radiotherapy and Oncology*, 86(1):20–24.

Suh, Y., Sawant, A., Venkat, R., and Keall, P. (2009). Four-dimensional IMRT treatment planning using a DMLC motion-tracking algorithm. *Physics in medicine and biology*, 54:3821.

Tacke, M. (2009). *Adaptation of high-precision radiotherapy to moving target volumes in real-time using dynamic multileaf collimators*. PhD thesis, University of Heidelberg.

Tacke, M., Nill, S., Häring, P., and Oelfke, U. (2008). 6 MV dosimetric characterization of the 160 MLC$^{\mathrm{TM}}$, the new siemens multileaf collimator. *Medical physics*, 35:1634.

Tacke, M., Nill, S., and Oelfke, U. (2007). Real-time tracking of tumor motions and deformations along the leaf travel direction with the aid of a synchronized dynamic MLC leaf sequencer. *Physics in Medicine and Biology*, 52:N505.

Tacke, M. B., Nill, S., Krauss, A., and Oelfke, U. (2010). Real-time tumor tracking: Automatic compensation of target motion using the siemens 160 MLC. *Medical physics*, 37:753.

Takayama, K., Mizowaki, T., Kokubo, M., Kawada, N., Nakayama, H., Narita, Y., Nagano, K., Kamino, Y., and Hiraoka, M. (2009). Initial validations for pursuing irradiation using a gimbals tracking system. *Radiotherapy and Oncology*, 93(1):45–49.

Tsunashima, Y., Sakae, T., Shioyama, Y., Kagei, K., Terunuma, T., Nohtomi, A., and Akine, Y. (2004). Correlation between the respiratory waveform measured using a respiratory sensor and 3D tumor motion in gated radiotherapy. *International journal of radiation oncology, biology, physics*, 60(3):951–958.

Ulrich, S. (2009). *Optimization, realization and quality assessment of arc-modulated cone beam therapy*. PhD thesis, University of Heidelberg.

Van Herk, M. (2004). Errors and margins in radiotherapy. In *Seminars in radiation oncology*, volume 14, page 52–64.

Vapnik, V. N. (1998). *Statistical learning theory*, volume 2. Wiley, New York.

Vedam, S., Keall, P., Docef, A., Todor, D., Kini, V., and Mohan, R. (2004). Predicting respiratory motion for four-dimensional radiotherapy. *Medical physics*, 31:2274.

Vedam, S., Kini, V., Keall, P., Ramakrishnan, V., Mostafavi, H., and Mohan, R. (2003). Quantifying the predictability of diaphragm motion during respiration with a noninvasive external marker. *Medical Physics*, 30:505.

Venables, W. N. and Ripley, B. D. (2002). *Modern applied statistics with S*. Springer, Berlin.

Verellen, D., De Ridder, M., Linthout, N., Tournel, K., Soete, G., and Storme, G. (2007). Innovations in image-guided radiotherapy. *Nature Reviews Cancer*, 7(12):949–960.

Verellen, D., De Ridder, M., Tournel, K., Duchateau, M., Reynders, T., Gevaert, T., Linthout, N., and Storme, G. (2008). An overview of volumetric imaging technologies and their quality assurance for IGRT. *Acta Oncologica*, 47(7):1271–1278.

Webb, S. and Binnie, D. (2006). A strategy to minimize errors from differential intrafraction organ motion using a single configuration for a'breathing'multileaf collimator. *Physics in medicine and biology*, 51:4517.

Wilbert, J., Baier, K., Richter, A., Herrmann, C., Ma, L., Flentje, M., and Guckenberger, M. (2010). Influence of continuous table motion on patient breathing patterns. *International Journal of Radiation Oncology* Biology* Physics*, 77(2):622–629.

Wilbert, J., Meyer, J., Baier, K., Guckenberger, M., Herrmann, C., Hess, R., Janka, C., Ma, L., Mersebach, T., Richter, A., et al. (2008). Tumor tracking and motion compensation with an adaptive tumor tracking system (ATTS): system description and prototype testing. *Medical physics*, 35:3911.

Wu, J., Ruan, D., Cho, B., Sawant, A., Petersen, J., Newell, L. J., Cattell, H., and Keall, P. J. (2011). Electromagnetic detection and real-time DMLC adaptation to target rotation during radiotherapy. *International journal of radiation oncology, biology, physics*.

Xing, L., Thorndyke, B., Schreibmann, E., Yang, Y., Li, T., Kim, G., Luxton, G., and Koong, A. (2006). Overview of image-guided radiation therapy. *Medical Dosimetry*, 31(2):91–112.

Xu, Q. and Hamilton, R. (2006). A novel respiratory detection method based on automated analysis of ultrasound diaphragm video. *Medical physics*, 33:916.

Zhang, T., Keller, H., O'Brien, M., Mackie, T., and Paliwal, B. (2003). Application of the spirometer in respiratory gated radiotherapy. *Medical Physics*, 30:3165.

Zhu, X., Bourland, J. D., Yuan, Y., Zhuang, T., O'Daniel, J., Thongphiew, D., Wu, Q. J., Das, S. K., Yoo, S., and Yin, F. F. (2009). Tradeoffs of integrating real-time tracking into IGRT for prostate cancer treatment. *Physics in Medicine and Biology*, 54:N393–N401.

Acknowledgments

This work has been carried out over the past three years in the group Physical Models within the Department of Medical Physics at the German Cancer Research Center (DKFZ). I want to express my gratitude to:

- Prof. Dr. Uwe Oelfke for his great supervision of my work on this excellent project and for his constant encouragement and confidence.
- Prof. Dr. Wolfgang Schlegel for providing pleasant working conditions in our department and for acting as the second referee of my thesis.
- Dr. Simeon Nill for constant support with experimental problems, for his help with the software development and for proofreading my abstracts, papers and this thesis.
- Kerstin Hofmann and Martin Menten for the great work on their student projects, the results of which have contributed to this thesis.
- Martin Fast for the good cooperation as well as his great job with the x-ray imaging system.
- Armin Runz and Gernot Echner for always providing creative and uncomplicated solutions to all mechanical problems.
- Dr. Jürgen Wilbert, Christian Hermann and Prof. Dr. Matthias Guckenberger from the University of Würzburg for the excellent cooperation in the HexaPOD project.
- Our industrial partners Siemens Healthcare and Calypso Medical Technoligies.
- The entire group E0401 for a friendly atmosphere, for numerous fruitful discussions and for loads of cake.
- My parents for constant support throughout my entire scientific education.
- Finally, Ulrike Krieg for her endless love and encouragement.

Erklärung:

Ich versichere, dass ich diese Arbeit selbstständig verfasst habe und keine anderen als die angegebenen Quellen und Hilfsmittel benutzt habe.

Heidelberg, den 6. Dezember 2011 .....